



141
819
THS

L
1001



This is to certify that the
thesis entitled

**A TWO-STAGE METHOD FOR ESTIMATING RELATIVE
PRESSURE FIELDS FROM NOISY VELOCITY DATA**

presented by

Christopher David Bolin

has been accepted towards fulfillment
of the requirements for the

 M.S. degree in Mechanical Engineering

Major Professor's Signature

 05/13/09

Date

PLACE IN RETURN BOX to remove this checkout from your record.
TO AVOID FINES return on or before date due.
MAY BE RECALLED with earlier due date if requested.

DATE DUE	DATE DUE	DATE DUE

A TWO-STAGE METHOD FOR ESTIMATING RELATIVE PRESSURE FIELDS
FROM NOISY VELOCITY DATA

By

Christopher David Bolin

A THESIS

Submitted to
Michigan State University
in partial fulfillment of the requirements
for the degree of

MASTER OF SCIENCE

Mechanical Engineering

2009

ABSTRACT

A TWO-STAGE METHOD FOR ESTIMATING RELATIVE PRESSURE FIELDS FROM NOISY VELOCITY DATA

By

Christopher David Bolin

The determination of intravascular pressure fields is important to the characterization of cardiovascular pathology. A two-stage method that solves the problem of estimating the relative pressure field from noisy velocity fields on an irregular domain with limited spatial resolution and includes a filter for the experimental noise is presented here. For the pressure calculation, the pressure Poisson equation is solved by embedding the irregular flow domain into a regular domain. To lessen the propagation of the noise inherent to the velocity measurements, three filters – a median filter and two physics-based filters – are evaluated and compared to three filters from the literature using a pair of two-dimensional mathematical phantoms. The most accurate pressure field results from a filter that applies in a least-squares sense three constraints simultaneously: consistency between measured and filtered velocity fields, divergence-free and removes noise in the Laplacian of the velocity field. This filter leads to a 5-fold gain in accuracy for the estimated relative pressure field compared to without noise filtering, using spatial resolutions that are consistent with phase-contrast magnetic resonance imaging (MRI) of the carotid artery on a clinical MRI scanner in the more complex of the two phantoms.

To my friends and family.

ACKNOWLEDGMENTS

I wish to acknowledge those with out whom this work would not have been possible. First, I would like to thank my committee members Professor Seungik Baek and Professor David Zhu for aiding me in the preparation of this thesis. I also wish to thank all of the course instructors I have had through my undergraduate and graduate studies for providing me with necessary the background knowledge to complete this work. Last, but certainly not least, I would especially like to thank my research advisor, Professor L. Guy Raguin for introducing me to this topic area and guiding me throughout this process.

I would also like to express my appreciation to those who provided non-academic support. I am grateful to my fellow graduate students who proved to be excellent distractions whenever they were necessary, and sometimes when they were wholly unnecessary. Thank you to my friends from my undergraduate years for entertaining me with your constant stream of emails about life in the 'real world' and the occasional visit. Finally, I would like to thank my parents and family for giving me ample opportunities to perform manual labor, feeding me good food whenever I came home and the constant encouragement.

“If we knew what it was we were doing, it would not be called research, would it?” - Albert Einstein

TABLE OF CONTENTS

LIST OF TABLES	viii
LIST OF FIGURES	x
LIST OF SYMBOLS	xiii
LIST OF ABBREVIATIONS	xvii
1 Introduction	1
1.1 Motivation	1
1.2 Methods of Pressure Estimation	3
1.3 Minimally Invasive Blood Flow Assessment	7
1.4 Thesis Layout	15
2 Methodology	16
2.1 Pressure Estimation	16
2.1.1 Theory	17
2.1.2 Numerical Implementation	19
2.2 Proposed Noise Filters	22
2.2.1 Filter Description	23
2.2.2 Filter Implementation	28
2.3 Mathematical Phantoms & Validation	29
2.3.1 Mathematical Phantoms	30
2.3.2 Resolution and Embedding Experiments	34
2.3.3 Filter Parameter Estimation and Noise Experiments	39
3 Results & Discussion	43
3.1 Influence of Spatial Resolution and Embedding Strategy	43
3.2 Calibration and Performance of Proposed Noise Filters	46
3.3 Discussion	57
4 Conclusions	63
4.1 Insight	64
4.2 Future Work	66
APPENDICES	69
A Finite Difference Schemes	69

B	Fourier Poisson Equation Solver	74
B.1	2D Neumann Problem	74
B.2	2D Dirichlet Problem	80
C	Mathematical Phantom	84
C.1	Couette Flow Between Rotating Cylinders	84
C.2	Poiseuille Channel Flow	86
D	Experimental Parameters	88
E	Tabulated Experimental Results	91
	BIBLIOGRAPHY	95

LIST OF TABLES

B.1	The weights for the perturbation required to solve the 2D Neumann Poisson equation.	79
D.1	Parameters used in the Couette flow mathematical phantom in the resolution, embedding and initial noise experiments.	89
D.2	Parameters used in the Couette flow mathematical phantom noise experiments with more realistic viscous terms.	89
D.3	Parameters used in the Poiseuille flow mathematical phantom noise experiments.	90
E.1	The normalized relative RMS error, $\bar{\epsilon}$, results of the isotropic and anisotropic resolution tests (see Figures 3.1 and 3.2).	91
E.2	The normalized relative RMS error, $\bar{\epsilon}$ (%), results of the embedding tests (see Figure 3.3).	92
E.3	The filter parameters that yield optimal performance at SNR = 5. These are the parameters used in all future experiments with noisy velocity fields (see Figures 3.4 and 3.5).	92
E.4	The average normalized relative RMS error and standard deviation, $\bar{\epsilon} \pm \sigma$ (%), in the estimated relative pressure field, for the initial Couette flow parameters, a resolution of $\eta = 0.05$ on a 20×20 flow domain Ω_F and an embedding level $\Gamma = 25\%$, after applying the three filters proposed here (Median Filter, Filter 1, Filter 2) to the relative pressure field estimated with no filtering and three filters from the literature (PSDF [1], $(d/dx)^2$ [2], Visc. Diss. [3]) over the range of SNR tested (see Figure 3.6).	93
E.5	The average performance factor F and standard deviation, $F \pm \sigma$, for all filters tested using the initial Couette flow experimental parameters, a resolution of $\eta = 0.05$ on a 20×20 flow domain Ω_F and an embedding level $\Gamma = 25\%$ across the range of SNR tested (see Figure 3.8).	93

- E.6 The average normalized relative RMS error and standard deviation, $\bar{\varepsilon} \pm \sigma$ (%), in the estimated relative pressure field, for the second Couette flow parameters, a resolution of $\eta = 0.05$ on a 20×20 flow domain $\Omega_{\mathbb{F}}$ and an embedding level $\Gamma = 25\%$, after applying the three filters proposed here (Median Filter, Filter 1, Filter 2) to the relative pressure field estimated with no filtering (see Figure 3.10). 94
- E.7 The average normalized relative RMS error and standard deviation, $\bar{\varepsilon} \pm \sigma$ (%), in the estimated relative pressure field, for the Poiseuille flow parameters, a resolution of $\eta = 0.05$ on a 20×20 flow domain $\Omega_{\mathbb{F}}$ and an embedding level $\Gamma = 25\%$, after applying the three filters proposed here (Median Filter, Filter 1, Filter 2) to the relative pressure field estimated with no filtering and two filters from the literature ($((d/dx)^2$ [2], Visc. Diss. [3]) over the range of SNR tested (see Figure 3.11). 94

LIST OF FIGURES

2.1	The algorithm for solving the PPE on an irregular domain as described in [4]. The Poisson equation is solved in step 4 using the direct method outlined in Figure 2.2 and detailed in Appendix B.1.	20
2.2	The algorithm for the direct solver of Poisson equations based on Fourier transforms as described in [5] that completes step 4 in Figure 2.1. Greater detail can be found in Appendix B.1.	22
2.3	The algorithm for projecting the noisy velocity field into the space of divergence-free fields as proposed in [1].	29
2.4	A schematic of the Couette flow system used in the 2D validation experiments with the important geometric features identified.	31
2.5	Example sections of the analytical solution for the Couette flow mathematical phantom: (a) the velocity field, \mathbf{V}_A ; (b) the magnitude of the pressure field relative to its spatial average, P_A , and normalized by its RMS, $P_{A,RMS}$, on Ω_F	33
2.6	A schematic of the Poiseuille flow system used in the 2D validation experiments with the important geometric features identified.	34
2.7	Example sections of the analytical solution for the Poiseuille flow mathematical phantom: (a) the velocity field at a arbitrary axial location, \mathbf{V}_A ; (b) the magnitude of the pressure field relative to its spatial average, P_A , and normalized by its RMS, $P_{A,RMS}$, on Ω_F	35
2.8	Illustrations useful in visualizing the embedding tests, (a) the definition of the level of embedding Γ and an schematic of the fluid domain Ω_F embedded in the center of the extended computational domain Ω , (b) Ω_F embedded centered in one direction and off-center in the other and (c) Ω_F embedded in a corner of Ω	38
3.1	Plot of the normalized relative RMS error, $\bar{\epsilon}$, of the estimated relative pressure field for Couette flow with no noise added as a function of the the relative pixel size, $\eta = \Delta x/2r_2$	44

3.2	Plot of the normalized relative RMS error, $\bar{\varepsilon}$, of the estimated relative pressure field for Couette flow with no noise added as a function of $\chi_\alpha = \alpha/\eta_{\text{conv}}$	45
3.3	Plot of the normalized relative RMS error, $\bar{\varepsilon}$, of the estimated relative pressure field for Couette flow with no noise added as a function of the embedding level Γ with a 20×20 , which corresponds to $\eta = 0.05$, flow domain $\Omega_{\mathbb{F}}$	46
3.4	Plot of the average normalized relative RMS error, $\bar{\varepsilon}$, of the estimated relative pressure field for the initial Couette flow experimental parameters, a resolution of $\eta = 0.05$ on a 20×20 flow domain $\Omega_{\mathbb{F}}$, an embedding level $\Gamma = 25\%$ and $\text{SNR} = 5$, as a function of: (a) α'_1 for Filter 1; (b) α'_2 and γ'_2 for Filter 2, the minimum is circled.	47
3.5	Contour plots of the average normalized relative RMS error, $\bar{\varepsilon}$, of the estimated relative pressure field for the initial Couette flow experimental parameters, a resolution of $\eta = 0.05$ on a 20×20 flow domain $\Omega_{\mathbb{F}}$ and an embedding level $\Gamma = 25\%$ and $\text{SNR} = 5$, as a function of: (a) α'_3 and γ'_3 for the filter with filtering term proposed in [2]; (b) α'_4 and γ'_4 for filter with the filtering term proposed in [3]. The minimum is circled in both figures.	48
3.6	Plot comparing the average normalized relative RMS error, $\bar{\varepsilon}$, in the estimated relative pressure field, for the initial Couette flow parameters, a resolution of $\eta = 0.05$ on a 20×20 flow domain $\Omega_{\mathbb{F}}$ and an embedding level $\Gamma = 25\%$, after applying the three filters proposed here (Median Filter, Filter 1, Filter 2) to the relative pressure field estimation with the field estimated with no filtering and three filters from the literature (PSDF [1], $(d/dx)^2$ [2], Visc. Diss. [3]) over the range of SNR tested.	49
3.7	Sample images of the magnitude of the normalized relative error distribution, $ \varepsilon(x, y) $, for the estimated relative pressure fields obtained using the initial Couette flow experimental parameters, a resolution of $\eta = 0.05$ on a 20×20 flow domain $\Omega_{\mathbb{F}}$, an embedding level $\Gamma = 25\%$ and $\text{SNR} = 5$ (a) no filter; (b) a median filter with radius 1 pixel; (c) Filter 1; (d) Filter 2; (e) a filter using the term of [2]; and (f) a filter using the term of [3] on the noisy velocity field. The normalized RMS error, $\bar{\varepsilon}$, is specified for each case.	51

3.8	Plot comparing the average performance factor F to SNR for all filters tested using the initial Couette flow experimental parameters, a resolution of $\eta = 0.05$ on a 20×20 flow domain Ω_F and an embedding level $\Gamma = 25\%$. Note that the median filter, the PSDF method and the filter using the viscous dissipation term of [3] all become ineffective by SNR = 15.	52
3.9	Sample velocity vector fields of the initial Couette flow experimental parameters, a resolution of $\eta = 0.05$ on a 20×20 flow domain Ω_F , an embedding level $\Gamma = 25\%$ and SNR = 5 illustrating the effect of (a) no filter (\mathbf{V}_{exp}); (b) a median filter with radius 1 pixel; (c) Filter 1; (d) Filter 2; (e) the filter using the term of [2], see (2.11); and (f) the filter using the term of [3], see (2.12), on the noisy velocity field. The subscript f indicates the filtered field. The performance factor, F , is specified for each case.	53
3.10	Plot of the average normalized relative RMS error, $\bar{\epsilon}$, in the estimated relative pressure field versus SNR for the more realistic Couette flow parameters, resolution $\eta = 0.05$ on a 20×20 flow domain Ω_F and an embedding level of $\Gamma = 25\%$, comparing the results of the three filters proposed here to the result with no filter over the range of SNR tested.	54
3.11	Plot of the average normalized relative RMS error, $\bar{\epsilon}$, in the estimated relative pressure field versus SNR for the Poiseuille flow parameters, resolution $\eta = 0.05$ on a 20×20 flow domain Ω_F and an embedding level of $\Gamma = 25\%$, comparing the results of the three filters proposed here to the result with no filter and two filters from the literature $(d/dx)^2$ [2], Visc. Diss. [3]) over the range of SNR = 5 – 20.	55
B.1	A schematic illustrating the computational domain Ω and defining the names of the boundaries and indices used in the direct solver of the Poisson equation in two-dimensions.	75
C.1	A schematic illustrating the components of v_θ for the case where $v_r = 0$ in the Cartesian coordinate system	85

LIST OF SYMBOLS

Roman Letters

B_0	External magnetic field strength (T)
D_a	Arterial diameter (m)
F	Performance factor of velocity filters (-)
h	Height of the channel of the Poiseuille flow mathematical phantom (m)
i	Index in the x-direction in real space (-)
j	Index in the y-direction in real space (-)
K	Step-size change for line-search algorithm (-)
k	Index in Fourier space corresponding to i (-)
M	Maximum index in the x-direction (-)
N	Maximum index in the y-direction (-)
N_Ω	Number of points across the computational domain (-)
N_{Ω_F}	Number of points across fluid domain (-)
P	Pressure field (N m^{-2})
P_{num}	Estimated relative pressure field (N m^{-2})
P_A	True relative pressure field (N m^{-2})
Q_c	Flow rate per unit depth ($\text{m}^2 \text{s}^{-1}$)
r	Radial coordinate (m)
r_1	Radius of inner cylinder of Couette flow mathematical phantom (m)
r_2	Radius of outer cylinder of Couette flow mathematical phantom (m)
R_a	Radius of a blood vessel (m)
s	Step index for algorithms (-)

t	Time (s)
\bar{U}_a	Average arterial velocity (m s^{-1})
u	Velocity component in the x-direction (m s^{-1})
v	Velocity component in the y-direction (m s^{-1})
v_r	Radial velocity component (m s^{-1})
v_θ	Azimuthal velocity component (m s^{-1})
x	Spatial coordinate (m)
y	Spatial coordinate (m)
Re	Reynolds number (-)
Wo	Womersley number (-)
Re_C	Average Reynolds number of Couette mathematical phantom (-)
Re_a	Average Reynolds number of arterial flow (-)

Bold symbols and vectors

∇	Partial derivative vector (m^{-1})
\mathbf{b}	Advection term subtracted from the viscous term of the Navier-Stokes equations ($\text{kg m}^{-2} \text{s}^{-2}$)
\mathbf{b}_F	Advection term subtracted from the viscous term of the Navier-Stokes equations in the fluid domain ($\text{kg m}^{-2} \text{s}^{-2}$)
\mathbf{D}	Discrete divergence operator (m^{-1})
\mathbf{F}	Body force vector per unit mass (m s^{-2})
\mathbf{G}	Discrete gradient operator (m^{-1})
\mathbf{J}	Angular momentum or spin (J s)
\mathbf{L}	Discrete laplacian operator (m^{-2})
\mathbf{M}	Bulk magnetization (J T^{-1})
\mathbf{P}	Discrete projector in the the space of divergence-free fields operator (-)
\mathbf{V}	Velocity field (m s^{-1})

\mathbf{V}_{exp}	Noisy velocity field (m s^{-1})
\mathbf{V}_{f}	Filtered velocity field (m s^{-1})
\mathbf{V}_{med}	Median filtered velocity field (m s^{-1})
\mathbf{V}_{A}	True velocity field (m s^{-1})
\mathbf{x}	Spatial vector (m)
$\boldsymbol{\mu}$	Magnetic moment (J T^{-1})
$\underline{\underline{\boldsymbol{\sigma}}}$	Stress tensor (m s^{-2})
\hat{n}	Boundary unit normal vector (-)

Greek letters

$\alpha_{1,2,3,4}$	Filter parameter, see equations (2.9, 2.10, 2.11, 2.12) (m^{-1})
Γ	Level of embedding (-)
γ	Gyromagnetic ratio ($\text{rad s}^{-1} \text{T}^{-1}$)
γ_2	Filter parameter, see equation (2.10) (m)
γ_3	Filter parameter, see equation (2.11) (s)
γ_4	Filter parameter, see equation (2.12) ($\text{m}^2 \text{s}^2 \text{kg}^{-1}$)
Δ	Step in finite difference equations (-)
$\varepsilon(x, y)$	Normalized error distribution (-)
η	Voxel size relative to a characteristic dimension (-)
η_{FFT}	Voxel size relative to a characteristic dimension in the direction of the fast Fourier transform (-)
η_{sol}	Voxel size relative to a characteristic dimension in the solution direction (-)
θ	Azimuthal coordinate (rad)
μ	Fluid dynamic viscosity (N s m^{-2})
ρ	Fluid density (kg m^{-3})
σ	Standard deviation (-)

χ	Ratio of pixel dimensions (-)
Ω	Computational domain (-)
Ω_{F}	Fluid domain (-)
ω	Angular frequency (rad s ⁻¹)
ω_0	Larmor frequency (rad s ⁻¹)
ω_1	Angular velocity of the inner cylinder in the Couette mathematical phantom (rad s ⁻¹)
ω_2	Angular velocity of the outer cylinder in the Couette mathematical phantom (rad s ⁻¹)
$\partial\Omega$	Boundary of the computational domain (-)
$\partial\Omega_{\text{F}}$	Boundary of the fluid domain (-)
$\alpha'_{1,2,3,4}$	Scaled filter parameter see equation (2.13) (s ⁻¹)
γ'_2	Scaled filter parameter, see equation (2.14) (s ⁻¹)
γ'_3	Scaled filter parameter, see equation (2.15) (s ⁻¹)
γ'_4	Scaled filter parameter, see equation (2.16) (s ⁻¹)
$\bar{\varepsilon}$	Normalized relative root-mean-square error over the fluid domain (-)

LIST OF ABBREVIATIONS

1D	One dimension or One-Dimensional
2D	Two dimension or Two-Dimensional
3D	Three dimension or Two-Dimensional
4D	Time-varying, three dimension or Four-Dimensional
CFD	Computational fluid dynamics
CT	Computed tomography
DSA	Digital subtraction angiography
FFT	Fast Fourier transform
LHS	Left hand side
MRI	Magnetic resonance imaging
NMR	Nuclear magnetic resonance
NSE	Navier–Stokes equations
PC	Phase contrast
PPE	Pressure Poisson equation
PSDF	Projection onto the space of divergence-free fields
RF	Radio frequency
RHS	Right hand side
RMS	Root-mean-square of points in the fluid domain
SNR	Signal-to-noise ratio
w.r.t.	With respect to

CHAPTER 1

Introduction

1.1 Motivation

This work focuses on the problem of determining relative pressure fields from velocity measurements, and it is motivated by the desire to characterize cardiovascular pathology in a minimally invasive manner. Of particular interest is the stability of pathology associated with arteriosclerotic stenoses in the internal carotid artery. Stenoses of this nature are involved in between 34 [6] and 44 percent [7] of strokes. It has been shown that methods of assessment beyond angiography, which is the standard, are required to better predict the physiologic effects of this type of stenoses [8]. Determining intravascular blood pressure or pressure gradient *in vivo* is considered to be crucial to the design of these assessment methods [8, 9]. To date, the primary technique of determining intravascular blood pressure is catheterization, an invasive procedure. Minimally invasive procedures are defined as those that involve intravascular injections or are entirely noninvasive. Medical diagnostic methods such as computed tomography (CT), Doppler ultrasonography, digital subtraction angiography (DSA) and magnetic resonance imaging (MRI) are capable of quantifying *in vivo* blood flow in a minimally invasive manner, but they are unable to provide di-

rect pressure measurements. Thus, a method of estimating the pressure field based on these quantizations is required if a minimally invasive diagnostic tool is to be implemented.

A two-stage method for estimating the relative pressure field from discrete noisy measurements of the velocity field is proposed here. The first stage consists of an effort to reduce the propagation of noise from the velocity field into the pressure estimation. The effects of six different schemes are compared. One of these filters is a common filter used in image processing, namely a median filter, two others are physics-based methods developed in this work and the final three are techniques proposed in the literature. The physics-based label applied to the methods developed here is used to imply that they are designed to take into account the physics of the flow rather than using arbitrary smoothing functions like the median filter. The second stage of the method estimates the relative pressure field from the filtered velocity field. This is rendered more complex by the low spatial resolution and irregular nature of the discretized domains containing blood flow as assessed by minimally invasive techniques. Accordingly, a technique described previously is chosen as a way to handle these computational complexities [4]. It is shown in this work that the physics-based filtering schemes proposed here increase the accuracy of the estimated relative pressure field at realistic signal-to-noise-ratios (SNR) as compared to the second-stage acting on the noisy velocity field and the solver with a median filter. When compared to the techniques proposed in the literature, the application of the two proposed physics-based methods produces a relative pressure field as with less accuracy but more quickly (Filter 1, see Section 2.2.1) or greater accuracy and the same computational time (Filter 2, see Section 2.2.1).

The remainder of this chapter is divided into three parts. First, a review of proposed methods for the estimation of the intravascular pressure field is presented. Second, methods of minimally invasive blood flow assessment are discussed with an

emphasis placed on phase contrast (PC) MRI. Many of the assumptions pertaining to resolution and likely SNR for the numerical studies in this work are based on capabilities of PC-MRI; therefore, a brief introduction to the principles of PC-MRI is presented to help the reader understand these assumptions. The final section is a brief description of the layout and organization of this thesis.

1.2 Methods of Pressure Estimation

Several methods of estimating intravascular pressure fields based on the minimally invasive assessment of blood flow have been proposed in the literature. In general, all methods require geometry measurements that are also acquired during the imaging procedures. The methods can be divided into two major categories based on the amount of subject data used in the pressure estimation. Methods that require discrete velocity or acceleration fields in addition to geometry measurements as inputs for the pressure estimation make up the first category. This category can be further subdivided into two groups, those that solve the divergence of the Navier-Stokes equations (NSE), called the pressure Poisson equation (PPE, see Section 2.1.1), for pressure and those that use other methods. The second category of estimator uses volumetric flow rates or a single plane of a velocity field as inputs and boundary conditions for computational fluid dynamics (CFD) software. The CFD software is used to estimate the rest of the velocity field, the pressure field and other fluid dynamic parameters of interest. Methods from the first category can be construed as forms of CFD; however, in this work the term CFD is used to refer to any software that estimates both the velocity field and pressure field within the vessel. The estimation methods of the first group are based entirely on subject-specific characterizations of the velocity field.

The PPE has been used in several ways to estimate the relative pressure field and

the relative pressure gradient. One of the early methods to employ of the PPE uses an iterative technique based on Fourier transforms to solve for the relative pressure field. The method was initially tested for robustness to noise in two dimensions (2D) using a mathematical phantom and its behavior was deemed acceptable. It was then used to estimate the time-varying, three-dimensional (4D) intraventricular pressure distribution *in vivo* [4]. An explicit iterative approach to the solution of the PPE has also been proposed and applied to the calculation of relative pressure fields within the human heart using arguments similar to those in [4]. The velocity data used in the *in vivo* experiments was not filtered which might have lengthened the convergence time and no validation was performed [10]. Another method projects the pressure gradient onto the curl-free subspace of square integrable vector fields. The method's robustness to noise and turbulent flow in stenotic geometries has been tested *in vitro* by comparing its results to those generated by the commercial CFD software FLUENT. It was determined that the estimation was accurate to within 10% for the SNR tested. However, the pressure was only estimated along the centerline and the method is limited to axisymmetric flows [11]. Another iterative approach to solving the PPE using a special property of the discretized version of the Laplacian operator has proven popular. The method was first qualitatively validated using a rotating cylinder containing a liquid at hydraulic-equilibrium. Pressure estimations were also made in a single plane in both further *in vitro* experiments to determine the effect of oscillatory flow on the estimation and *in vivo* experiments in the aortic arch [12]. The method was then modified and expanded to 4D pressure estimations. A median filter was added in an effort to reduce noise in both *in vitro* and *in vivo* experiments. Validation was performed in an *in vitro* experiment by comparing the calculated pressure difference across a flow phantom to that measured by pressure transducers at either end. *In vivo* estimations were also made in the aortic arch [13]. Further work using the modified version of this estimator from [13] compared the calculated

transstenotic pressure gradient to that measured by a pair of endovascular pressure-sensing guidewires in *in vivo* experiments. The transstenotic gradient was calculated by estimating three-dimensional (3D) relative pressure fields using the method of [13], time-averaging the fields over the cardiac cycle and finally calculating the gradient between two points that most closely mirrored the locations of the catheters. The calculated gradients were found to show high correlation and good agreement in vessels with little motion [14].

Other methods that require discrete velocity or acceleration fields as an input to their algorithms use a variety of techniques for estimating pressure. Early methods of estimating pressure focused on calculation of the pressure drop across regions of interest. The Bernoulli equation was used to estimate the pressure drop using the maximum blood velocity at the exit of the mitral valve in the human heart. Estimations were compared to the pressure drop measured by catheter and it was determined that the estimation agreed to within 20 – 25% and tended to underestimate the pressure drop [15]. A second method used flow rates, calculated based on measured discrete velocity fields and vessel cross-sectional areas, to calculate the one-dimensional (1D) relative pressure distribution along a vessel [16] and pressure-pulse waveforms [17]. These methods were found to agree within 15% to pressure catheter measurements in both *in vivo* and *in vitro* experiments. Direct integration of the pressure gradient as it appears in the NSE along a path has also been proposed. It was qualitatively tested using a technique similar to that used in [12] with the liquid replaced by a gel. The method was then applied to a series of *in vivo* cardiac imaging applications. Noise in the velocity field makes the integration of the pressure path-dependent [18]. Direct integration using a single plane of velocity data has been compared to the method of [13] for calculating pressure differences and little difference was noted between the two techniques [19]. In an effort to minimize the propagation of noise from the velocity field into the pressure field, integration of blood acceleration measurements have also

been proposed as a basis for pressure gradient [20] and pressure field estimations [21]. The estimate of the pressure gradient was tested in an *in vitro* experiment and compared to that measured by a pair of pressure catheters. High correlation between the estimated gradient and the measured gradient was found. An *in vivo* experiment was also performed to map the pressure gradient in the descending aorta [20]. Estimation of pressure fields using acceleration data was done by minimizing the curl of the pressure gradient along a series of arcs. The relative pressure field estimated in this manner was compared to that estimated by the method in [13] in *in vivo* experiments. The two methods were in good agreement [21]. Both methods relying on acceleration data ignored the contribution of viscosity in their calculations [20, 21].

Commercially available CFD software is considered to be a tool to extend the information obtained by minimally invasive flow assessments in instances where complete assessments are not possible [22]. To investigate the coupling of the information derived from the minimally invasive flow assessments and CFD, a study of the effect of various boundary conditions was undertaken using a U-bend model. This study indicated that a velocity field measured by MRI and normalized by an accurate measurement of flow rate at the inlet should be used for the inflow boundary condition. This held for both steady and unsteady cases [23]. Vessel geometry and a discrete velocity field derived from an *in vivo* flow assessment of the descending aorta were used to construct a model and for the inflow boundary condition, respectively, in an investigation into the potential of linking CFD and MRI. The commercial code STAR-CD was used to compare the computed velocity field at the exit of a region of interest to that measured by MRI. Good agreement between the two allowed justified investigation of other fluid dynamic parameters, including the static pressure distribution, using the CFD model [24]. Another study, also using flow rate boundary conditions derived from discrete velocity fields, used an in-house software to investigate fluid dynamics in the carotid artery. This method was validated using MRI

based flow measurements of several flow phantoms and good agreement was reported between the MRI measurements and the results of the CFD model. Peak pressure and pressure drop across a stenosis were amongst the fluid dynamic parameters investigated and the latter was used in some of the validation [25]. Other studies combine boundary conditions based on minimally invasive blood flow assessments and CFD, but they tend to focus on the quantification of wall shear stress and oscillatory shear index [23, 26, 27, 28, 29, 30]

1.3 Minimally Invasive Blood Flow Assessment

This review of some of the available techniques to assess blood flow in a minimally invasive manner illustrates some of the many ways that these assessments can be performed. Not all of these methods are capable of measuring the (4D) velocity field within a vessel, but all of them are able to provide the information necessary for some of the methods developed for estimating the relative pressure field or pressure gradient. For this reason they are referred to as 'assessment methods'. This review also justifies the initial assumption used in this work, that a characterization of the blood flow within a vessel is available. Methods beyond those presented here are able to assess blood flow, but these methods are more invasive than has been defined as desirable (i.e., requiring catheterization or surgical access to the vessel).

DSA methods are an extension of x-ray angiography to assess the rate of blood flow. They are based on the detection of the movement of radio-opaque contrast agents in the vessel of interest. The contrast agent is injected intravascularly or, in situations where a more controlled bolus is required, a catheter is used to inject it directly into the vessel of interest. An initial background digital image is recorded before the injection of the contrast agent. This image is then digitally subtracted from images recorded following the contrast injection. The resulting image is generally free

of structures that the contrast agent had not reached at the time of the recording of the second image. Various methods are then used to assess the blood flow based on these images. A review of these methods has been published [31], a few examples are reviewed here. One proposed method to estimate blood flow rates follows the leading edge of an injected bolus and uses the ratio of the temporal and spatial derivatives of its density to determine its average velocity. This method has been tested in a laminar flow phantom, and it was determined that the measured velocity was consistently higher than the average fluid velocity in the phantom [32]. A technique based on first pass distribution analysis has also been studied as a method of measuring blood volume flow rates [33]. This method was modified to address some of its limitations by using a dual energy-subtraction technique [34, 35]. Other methods of assessing blood flow using DSA include those based on contrast dilution [36] and contrast transit times [37]. All of these methods are limited to estimating bulk blood flow rates and tissue perfusion. Flow rates tend to be over estimated due to using leading edge of the bolus in the calculations [32, 37].

Doppler ultrasonography is a generic term applied to techniques of assessing blood flow using either continuous wave or pulsed wave systems. Continuous wave systems are older, but they are limited in their ability since they are incapable of separating signals from more than one flow and unable to quantify blood flow [38]. These limitations were overcome by the development of pulsed wave systems. In pulsed wave systems, a single piezoelectric crystal is used as the transmitter and receiver of the ultrasound signal. Transmitted waves are reflected off various tissues (i.e., red blood cells and bone) and those waves reflecting from the desired focal volume are interpreted. The focal volume is selected by gating the received signal based on the velocity of sound in tissue to control the focal depth and its size perpendicular to the transmitter/receiver is fixed by the system being used. To aid in identifying a volume of interest, the Doppler system is often combined with an ultrasound imaging

system. The attenuation of the signal due to its passage through tissue between the receiver and the volume of interest is compensated for by signal amplification. There is a limit to the focal depth, even with amplification, making studies of deep tissue vessels difficult. After further processing of the received signal, information pertaining to the velocity of the reflector is contained in the phase difference between the reflected wave and the transmitted wave subject to the Doppler equation. The ability of pulsed wave systems to choose focal depth and volume allows for the measurement of flow profiles within vessels. However, because pulsed wave systems sample the data, aliasing must be avoided. Thus, the maximum measurable velocity is constrained by the transmitted signal's pulse frequency. The most accurate velocity measurements are made when the angle between the axis of the transmitted wave and the direction of the moving reflector is close to zero. Aligning the transmitter/receiver along the axis of a vessel to accommodate this can be made difficult by anatomical structures such as bones or the lungs, which absorb signal [39]. Transcutaneous Doppler ultrasound is a noninvasive procedure, and it has been applied to study blood flow and changes in blood flow due to pathology. Volume flow rates in the coronary artery as calculated by the peak velocity in the vessel was an early area of application of these methods [40]. Peak and mean flow velocities have also been measured in the cerebral artery using transcranial Doppler ultrasound to study spontaneous hemorrhage [41]. A comparison between transthoracic Doppler ultrasonography and the use of an invasive Doppler guidewire demonstrated that the noninvasive transthoracic method was able to accurately measure coronary flow velocity [42]. A similar study demonstrated that the noninvasive transthoracic ultrasound method is useful in the assessment of stenosis in coronary arteries based on flow velocities [43].

CT imaging is a method of reconstructing an image of the interior of an object from measurements of the attenuation of a series of x-rays transmitted at different angles. Unlike standard x-ray imaging, CT allows for soft-tissues of different types

to be distinguished. Its measurement accuracy allows for the planning and monitoring of various medical treatments [44]. Most techniques for blood flow assessment using CT, like DSA, require the intravascular injection and subsequent tracking of a radio-opaque contrast agent. Quantification of blood flow is then most often done by using varying forms of indicator-dilution theory as proposed in [45] and [46]. Experiments using a steady-flow phantom and three approaches based on indicator-dilution theory indicated good agreement between the known flow rate in the phantom and that measured by CT [47]. A further set of phantom experiments examining pulsatile and steady flow determined that the use of indicator-dilution theory for measuring blood flow with CT was heavily dependent on the relation between the concentration of the contrast agent and the intensity of the image [48]. The volume flow rate of cardiac output has been measured using these methods and compared to thermodilution catheter measurements with good agreement [49, 50, 51]. Pulmonary blood flow has also been assessed with CT and indicator-dilution theory [52]. However, there is some question as to the reliability of indicator-dilution theory as a method of assessing blood flow [53, 54]. Consequently, other methods using CT are being investigated. Assessments of coronary output have also been performed using precise measurements of the cardiac stroke volume and rate [53]. A low flow rate phantom was used to validate a method that measures changes in contrast along the axis of the phantom [55]. Another method is based on continuum theory and estimates discretized velocity fields within a volume based on the motion of the surrounding tissue [56]. With the exception of the method in [56], CT is primarily used to quantify volume flow rates and not discretized velocity fields.

MRI is a tomographic imaging technique for making measurements within opaque objects (i.e., without optical access). MRI measurements do not require intravascular injections or the use of ionizing radiation, thereby reducing undesirable effects and risks when compared to methods like DSA and CT, and they do not have a limited fo-

cal depth unlike methods based on transcutaneous ultrasound. Instead, MRI is based on the phenomenon of nuclear magnetic resonance (NMR) that was first described in 1946 [57, 58]. NMR was originally used for spectroscopic measurements, and it was not until the 1970's that imaging methods using NMR were first implemented [59, 60]. A full description of the physics of NMR requires the use of quantum mechanics and is beyond the scope of this work. A brief description of the underlying principles is possible using a semi-classical approach and is presented here for completeness.

Subatomic particles are fully described by four quantum numbers. Of these quantum numbers, the one of greatest importance to MRI is the quantum spin number, half or whole integers (i.e., $0, 1/2, 1, 3/2, 2, \dots$) for protons, which characterizes the angular momentum of the particle. According to the Pauli exclusion principle, no two particles (e.g., protons) in a system (e.g., an atomic nucleus) can have the same set of quantum numbers. Those nuclei with an odd number of protons and neutrons have a non-zero net spin and possess an angular momentum \mathbf{J} . The positive electric charge carried by the proton together with the act of spinning about its own axis generate a magnetic moment, $\boldsymbol{\mu}$, proportional to \mathbf{J} . The proportionality constant relating \mathbf{J} to $\boldsymbol{\mu}$ is γ , the gyromagnetic ratio which is dependent on the makeup of the nucleus. A group of nuclei with the same γ is called a spin-system.

MRI measurements are made by manipulating the $\boldsymbol{\mu}$ of the members of the spin-system. At thermodynamic equilibrium the $\boldsymbol{\mu}$ of the individual nuclei of a spin-system are oriented randomly and their sum, called the bulk magnetization, \mathbf{M} , is zero. If this spin-system is placed in an external magnetic field of strength B_0 , the $\boldsymbol{\mu}$ of the nuclei with the field generating a non-zero \mathbf{M} oriented along the direction of field. The $\boldsymbol{\mu}$ of the nuclei then precess randomly around the direction of B_0 at the Larmor frequency, $\omega_0 = \gamma B_0$, of that combination of spin-system and external field strength. When the spin-system is excited with a radio frequency (RF) pulse oscillating at ω_0 and oriented perpendicular to the direction of B_0 , the spins tip into the plane

perpendicular to B_0 creating a transverse component of \mathbf{M} . The oscillating field generated by the relaxation of this transverse component back to its equilibrium state induces a voltage in a receiver coil placed around the sample, which is the signal used to generate images. By applying known linear magnetic field gradients in addition to B_0 , a signal can be spatially located by the unique ω_0 of each point in the combined magnetic fields. An inverse Fourier transform is used to synthesize the measured signal from Fourier space into physical space. Most commonly in medical imaging, the hydrogen nucleus is the source of signal. In addition to the applied magnetic fields, the strength of the external field for each member of the spin-system is affected by the type of molecule to which it is attached. This allows MRI to distinguish between different molecules, and their associated tissues, within the body containing hydrogen nuclei based on their ω_0 . In order to obtain a sufficient signal-to-noise ratio (SNR) in the acquired images, the signal from a slice of the material being imaged is integrated generating a discrete 2D representation of 3D volumes which are called voxels. Generally, the dimensions of a voxel vary from a few μm to a few cm. For 2D imaging, the achievable in-plane resolution depends on the imaging system being used, but in most clinical applications, whose magnetic field gradients are limited for safety reasons, resolutions of a few hundred μm are possible. With higher strength research systems it can be as low as tens of μm . More detailed descriptions of the physics of NMR, the generation of signal and the signal processing required are available in [61, 62].

Flow can be assessed using MRI in several different ways. Of these, only two are routinely used in medical imaging due to time constraints. Spin-tagging is a method that encodes volumes of material with a specific spin magnetization [63, 64]. Images acquired using this method have a grid of bright and dark lines. The fluid flow is allowed to evolve and velocities are inferred from the motion of the grid lines in subsequent images or using methods like optical flow theory [65, 66]. PC-MRI

techniques are able to measure time-resolved 3D velocity fields directly, unlike spin-tagging methods, within opaque flow systems using special sequences of magnetic field gradients [67, 68]. In this way velocity information is encoded directly into the phase of the signal. A phase difference map is generated by subtracting the phase map of a second image from a first reference image. The local phase difference is proportional to the velocity of the fluid within that voxel [62]. Two images are enough to encode velocity in a single direction. Four images are required for 3D velocity measurements which increases scan time [69].

PC-MRI techniques are not without their limitations. The time required to measure velocity fields (\sim minutes) makes it impractical for assessing flows other than those that are either steady or periodic. The latter is possible by gating, either prospectively or retrospectively, the imaging sequence and by acquiring a few lines in Fourier space at a time and building an image that represents a particular phase of the periodic flow. These techniques are called cine PC-MRI [62]. Noise arising due to the thermal Brownian motion of electrons in the electrical components in the imaging system and the object being scanned. A number of images are averaged together to enhance the SNR which further increases the imaging time [61]. Voxels that contain both moving and stationary spins, like those in the near-wall region of a blood vessel, are subject to partial volume effects. Depending on how the velocity is calculated from the phase difference map, the voxel will indicate either a higher velocity, biased by the moving spins of the blood, or a lower velocity, biased by the stationary spins of the wall or surrounding tissue [70]. Velocity measurements are also susceptible to artifacts created by the motion of the spins. Sudden accelerations, large velocity gradients within the voxel and the movement of spins from one voxel to another during imaging can degrade the quality of the data [71]. These effects can be minimized by using short duration imaging sequences and developments in technology [72].

PC-MRI is a popular method for noninvasively measuring discrete velocity fields

in opaque systems. Several of the methods of estimating pressure reviewed above rely on PC-MRI to provide their input velocity data [10, 11, 12, 13, 14, 17, 23, 24, 25, 27]. A published review of methods used in cardiovascular fluid mechanics contains a section on biomedical uses of PC-MRI [73]. Phantom and patient studies have been used to develop a technique of assessing blood flow that is independent of system and patient parameters. The phantom studies indicated that the method was accurate to within 10% over a wide range of flow velocities [74]. A study compared the time-varying behavior of the instantaneous and mean flow rates in phantom and *in vivo* experiments as measured by Doppler ultrasound and PC-MRI. The work determined that Doppler ultrasound techniques were quicker and of lower cost but PC-MRI delivered more quantitative information about the flow [75]. The measurement of velocity in pulsatile flow has been evaluated using a flow phantom and determined to be accurate and reliable [76]. The accuracy of PC-MRI in measuring pulsatile flow was also validated in a flow phantom using the Womersley solution to the NSE. Peak velocities were found to be within 13% of those predicted by theory [77]. PC-MRI was compared to digital particle imaging velocimetry, a widely used technique in fluid mechanic experiments, in *in vitro* studies of total cavopulmonary connection. The two techniques showed good agreement in the large scale flow patterns and PC-MRI was determined to have potential value in the assessment of this procedure [78]. A more complete review of uses of PC-MRI in the evaluation of heart disease is available [79]. A comparison between CFD simulation and PC-MRI measurements on *in vitro* models demonstrated that measurements of velocity in the carotid artery made by PC-MRI were accurate to within 10% of those predicted by simulation [80].

1.4 Thesis Layout

The remainder of this work is divided into three chapters. In Chapter 2 the theoretical considerations and the implementation of the proposed method will be detailed. Included in this chapter is a description of the mathematical phantom used to validate the method and the procedures for optimizing the proposed filters. Chapter 3 presents and discusses the results of the validation and parameter estimation. The emphasis of the discussion is on the effect of the proposed velocity filtering methods. Finally, in Chapter 4 a conclusion of the findings this work is presented and potential paths of future work are introduced.

CHAPTER 2

Methodology

In this chapter the theory and implementational considerations necessary for the proposed two-stage method are presented. The technique chosen to estimate the relative pressure field is that proposed in [4]. This approach is general enough to handle the various complications of the problem at hand and applies boundary conditions in a way that is anticipated to be useful in future applications of the methodology presented here. A description of the technique is included here for completeness. The filters proposed here to minimize the propagation of noise from the velocity data into the pressure estimation are characterized in the second section. Next, a description of the procedure used to validate the method using a mathematical phantom is presented.

2.1 Pressure Estimation

Though the method chosen to estimate the relative pressure field has been described previously, the detail of its implementation was not. Thus, this section is divided into two parts. First, the theory behind the method starting from the NSE is described. Elements of this theoretical discussion will also be useful to the understanding of the noise mitigation techniques proposed in Section 2.2. Then, the detailed description

of the implementation of the method includes the algorithm used in the solution of the PPE.

2.1.1 Theory

In a fluid flow, the relationship between the pressure field, P , and the fluid velocity field, \mathbf{V} , is described by the NSE. The general form of the NSE for an incompressible, homogeneous fluid, like blood flowing within the larger vessels of the vascular system, can be written as:

$$\rho \left[\frac{\partial \mathbf{V}}{\partial t} + (\mathbf{V} \cdot \nabla) \mathbf{V} \right] = \rho \mathbf{F} + \nabla \cdot \underline{\underline{\sigma}} \quad (2.1)$$

where ρ is the density of the fluid, \mathbf{F} is the body force term and $\underline{\underline{\sigma}}$ is the stress tensor [81]. In addition, the following continuity equation needs to be satisfied:

$$\nabla \cdot \mathbf{V} = 0. \quad (2.2)$$

This is a system with more unknowns, nine, than equations, four. A set of constitutive equations are necessary to form a tractable problem. These constitutive equations express the components $\underline{\underline{\sigma}}$ in terms of the components of the gradients of \mathbf{V} [82].

Fluids are generally characterized as either Newtonian or non-Newtonian depending on the constitutive equation that is used to close the problem. Newtonian fluids are those that have a linear relationship between the components of $\underline{\underline{\sigma}}$ and the velocity gradients. Blood belongs to a non-Newtonian class of fluids. These fluids do not have a linear relationship between the components of $\underline{\underline{\sigma}}$ and the velocity gradients which complicates their description. However, for blood these effects are confined to flow in vessels smaller than 0.5 mm in diameter where the shear-rate is low. In vessels larger than this, like the carotid artery (10 mm in diameter), blood can be assumed to behave like a Newtonian fluid; thus simplifying the analysis [83]. It can be shown that using (2.2) and the assumption of a Newtonian fluid, (2.1) simplifies to

$$\nabla P = -\rho \left[\frac{\partial \mathbf{V}}{\partial t} + (\mathbf{V} \cdot \nabla) \mathbf{V} \right] + \rho \mathbf{F} + \mu \nabla^2 \mathbf{V} \quad (2.3)$$

where μ is the dynamic viscosity of the fluid. Further, it is assumed that \mathbf{F} can be ignored.

It would be convenient at this point to also ignore the effect of viscosity because the numerical approximation of higher derivatives (e.g., those in the viscous term of (2.3)) using noisy data is problematic and can lead to amplification of the noise. This has been done in studies of larger vessels [12, 20, 21]. Before neglecting the higher derivatives in the viscous terms of (2.3) one should calculate the Womersley number (Wo) for the vessel of interest. The Womersley number is defined as

$$Wo = R_a \left(\frac{\omega \rho}{\mu} \right)^{\frac{1}{2}} \quad (2.4)$$

where R_a is the radius of the vessel, ω is the frequency of the oscillations in rad/s and ρ and μ are defined as before. Womersley numbers less than 1 indicate viscous terms are very important and those greater than 10 indicate that they can be ignored [84]. For flow in the carotid artery, $R_a \approx 5$ mm, with a pulse rate of 60 beats per minute and using $\mu = 0.004$ N s and $\rho = 1040$ kg/m³, $Wo \approx 6.4$ which is between the two cut-off points. Variability in the pulse rate and size of the carotid artery will affect the value of Wo , but it is not expected that this variability will push the flow into the realm where viscous effects can definitely be ignored. Thus, the viscous terms will be included in the following algorithms.

The solution of (2.3) for P can be accomplished in many ways. If the velocity field is known, the pressure field can be solved for by integrating (2.3) along a path as was done in [18]. However, because of the noise inherently present in experimental data, the resulting pressure field depends on the integration path. To avoid path dependence, the method used to determine the pressure field from a velocity field is to solve the PPE which is derived by taking the divergence of (2.3)

$$\nabla^2 P = \nabla \cdot \mathbf{b} \quad (2.5)$$

where \mathbf{b} is the right-hand-side, RHS, of (2.3). Neumann boundary conditions are

prescribed for the PPE

$$\nabla P \cdot \hat{n} = \mathbf{b} \cdot \hat{n} \quad (2.6)$$

where \hat{n} is the unit outward normal on the boundary [85]. The pressure field resulting from (2.5) is unique up to an integration constant and is referred to as the relative pressure field. A measurement of the pressure at a point on $\Omega_{\mathcal{F}}$ can be used to compute the absolute pressure field. A measurement of this nature can only be obtained invasively, so the estimated pressure field is left relative to a constant to be determined later in Section 2.1.2. The PPE has also been shown in [4] to be a least-squares solution to (2.3) for cases where the system is inconsistent or overdetermined.

2.1.2 Numerical Implementation

On a discrete rectangular domain Ω , the PPE with prescribed boundary conditions on $\partial\Omega$, can be solved directly in several ways [86, 87]. For most *in vivo* applications, the flow domain $\Omega_{\mathcal{F}}$ is irregular (e.g., nonconvex). Direct solutions for the Poisson equation on irregular domains exist by embedding $\Omega_{\mathcal{F}}$ in an extended rectangular domain, $\Omega \supset \Omega_{\mathcal{F}}$, on which the Poisson equation is solved [88]. Depending on the size of $\Omega_{\mathcal{F}}$ and $\partial\Omega_{\mathcal{F}}$, this technique may be inefficient and difficult to implement as it requires the careful accounting of points on $\partial\Omega_{\mathcal{F}}$ for the proper application of the boundary conditions. The alternative iterative approach proposed in [4] has been selected for use in this work. This technique also uses embedding in an extended rectangular domain, but implements the boundary conditions in simpler manner.

In this method, points within $\Omega_{\mathcal{F}}$ are treated in a different manner than those outside of $\Omega_{\mathcal{F}}$ in the steps leading up to the solving PPE. The value of \mathbf{b} inside the fluid domain, $\mathbf{b}_{\mathcal{F}}$ (i.e., on $\Omega_{\mathcal{F}}$), is calculated once and used throughout the iterative process whereas outside the flow domain (i.e., on $\Omega \setminus \Omega_{\mathcal{F}}$) \mathbf{b} is updated after each

<p>step 1 Approximate \mathbf{b}_F</p> <p>step 2 Approximate $\nabla P^{(s)}$</p> <p>step 3 Approximate $\nabla \cdot \mathbf{b}^{(s)}$ on Ω and $\mathbf{b} \cdot \hat{n}$ on $\partial\Omega$</p> <p>step 4 Solve the Poisson equation using a direct method</p> <p>step 5 Calculate $\ P^{(s)} - P^{(s-1)}\ /\ P^{(s)}\$</p>

Figure 2.1. The algorithm for solving the PPE on an irregular domain as described in [4]. The Poisson equation is solved in **step 4** using the direct method outlined in Figure 2.2 and detailed in Appendix B.1.

iteration (indexed by s) to the value of ∇P from the previous iteration:

$$\begin{aligned} \nabla^2 P^{(s)} &= \nabla \cdot \mathbf{b} & \text{on } \Omega \\ \nabla P^{(s)} \cdot \hat{n} &= \mathbf{b}^{(s)} \cdot \hat{n} & \text{on } \partial\Omega \end{aligned} \quad (2.7)$$

where

$$\mathbf{b}^{(s+1)} = \begin{cases} \mathbf{b}_F & \text{on } \Omega \\ \nabla P^{(s)} & \text{on } \Omega \setminus \Omega_F \end{cases} \quad (2.8)$$

A point is identified as being on Ω_F or on $\Omega \setminus \Omega_F$ by a mask and the initial guess for the pressure field, $P^{(0)}$, is zero everywhere. In this method, the Neumann boundary conditions are applied on $\partial\Omega$ rather than on $\partial\Omega_F$. By choosing Ω to be rectangular, the calculation of \hat{n} is trivial which simplifies the application of the boundary conditions.

The algorithm for solving the PPE, as described in [4], is outlined in Figure 2.1. Second-order accurate finite difference schemes are used to approximate all the derivatives necessary to compute \mathbf{b} and its divergence as well as the divergence of pressure. In the calculations of **step 1**, central difference schemes are used where possible and forward or backward schemes are used on $\partial\Omega_F$. At locations where second-order schemes are not possible, first-order schemes are used if the data to complete them

is available. Regions exist where neither second- nor first-order schemes are possible occur near $\partial\Omega_{\mathbb{F}}$. Special approximations are used at these points that assume the boundary is located one half of a voxel away and that the wall velocity is zero. These assumptions allow for a rudimentary estimation of the derivative. The schemes used are described in detail in Appendix A. Even with these special schemes it is still possible that there will be regions where second-order derivatives will not be possible to approximate. At these points the term for which no approximation can be made is estimated to be the median of its neighbors. The approximations in **step 2** and **step 3** are done with no consideration for the difference between $\Omega_{\mathbb{F}}$ and $\Omega \setminus \Omega_{\mathbb{F}}$. Therefore, second-order accurate schemes are always possible and no special schemes are necessary. The direct method used to solve the Poisson equation used in **step 4** is detailed below. The solution has converged when the absolute rate of change between iterations as calculated in **step 5** is less than some finite threshold, set to 10^{-3} here. Since pressure only appears as a gradient in (2.3), the converged solution is only accurate to an integration constant as discussed in Section 2.1.1. Thus, the spatial average of the pressure field on $\Omega_{\mathbb{F}}$ is subtracted from the pressure solution, yielding a relative pressure field, P_{num} [4].

By extending $\Omega_{\mathbb{F}}$ to Ω , one of the many direct methods of solving Poisson equations can be used to complete **step 4** from Figure 2.1. In this work the method based on fast Fourier transforms (FFT) described in [5] is applied. The basic algorithm is illustrated in Figure 2.2. The specific FFT and inverse FFT used depends on the boundary conditions and the dimensionality of the problem. For the PPE the boundary conditions are of the Neumann type as discussed in Section 2.1.1. This dictates the use of cosine transforms and inverse transforms. For 2D problems, a 1D transform is used and similarly for 3D problems a 2D transform is used. Certain numerical difficulties arise for the case of Neumann boundary conditions. Since the solution sought is a least-squares solution, these difficulties are bypassed by perturbing the problem.

- | | |
|----------------|----------------------------------------------------------------------------|
| step 4a | Incorporate the boundary conditions into $\mathbf{b}^{(s)}$ |
| step 4b | Perform a FFT to transform the equations into Fourier space |
| step 4c | Solve resulting series of tridiagonal systems for the Fourier coefficients |
| step 4d | Perform an inverse FFT to transform the solution back into physical space |

Figure 2.2. The algorithm for the direct solver of Poisson equations based on Fourier transforms as described in [5] that completes **step 4** in Figure 2.1. Greater detail can be found in Appendix B.1.

The perturbation uses a constraint to force the system to conform to Green’s theorem. Even with the perturbation, one of the tridiagonal systems solved in **step 4c** is singular. This system is identified and its output is set to zero. Details of the transforms and inverse transforms used, the incorporation of the boundary conditions and a description of the perturbation used are found in Appendix B.

The method described in this section has been implemented in MatLab (The MathWorks, Natick, MA). Special functions were written for nearly all aspects of the algorithm due to the complexity of the steps required to handle the irregular domain and consistency issues within the available built-in functions. The primary exception is the method used for the solution of the tridiagonal systems Poisson solver. This is accomplished using MatLab’s matrix division operator.

2.2 Proposed Noise Filters

The negative effect of noise in the velocity field on the accuracy of the pressure estimation has been mentioned in several of the methods reviewed in Section 1.2 [4, 10, 11, 12, 13, 18, 20, 21]. In an attempt to mitigate these effects, three

different filters are proposed and tested in this work. These proposed filters are compared to three filters described in the literature.

2.2.1 Filter Description

The methods proposed here for removing noise in the velocity field (i.e., to smooth the velocity field and its derivatives either in an arbitrary fashion or in a selective fashion by applying physical constraints) are identified by different names depending on their area of application. For example, the estimation of the pressure field in a fluid based on its measured velocity field is an inverse problem. Many problems of this type are ill-posed; thus, they require steps to introduce enough additional information for a unique solution to be found. These steps, called regularization, can involve the assumption of smoothness constraints similar to some of the velocity filtering methods used here. However, the six methods for filtering the velocity field investigated here are not coupled to the estimation of the pressure field and are not performed simultaneously. For this reason regularization is not the appropriate terminology. A filter is commonly defined as a device that has the effect of selectively modifying something to eliminate an undesirable attribute. In this case the measured velocity field is modified in ways that attempt to minimize measurement noise in the field. Thus, these methods of modifying the experimental velocity field are referred to as filters henceforth.

Experimental velocity measurements are inherently polluted by noise, which is amplified by the numerical differentiation required for most of the methods of pressure estimation discussed in Section 1.2. If smaller vessels are to be investigated the high-order terms in the NSE cannot be ignored as demonstrated in Section 2.1.1; therefore, some sort of filtering is required for the accurate estimation of the relative pressure field. The purpose of this work is to identify the appropriate method for mitigating the noise in the velocity field and its derivatives. The exact manner of

optimization is left for later discussion. Tura *et al.* [89] has proposed an Tikhonov-type velocity field filtering technique based on a modified form of the NSE for cases where measurements are noisy and incomplete. Using the NSE to filter the velocity field and estimate the relative pressure field would not be appropriate unless both the velocity filtering and pressure estimation are performed simultaneously, which would then be more computationally intensive than using either by themselves. A few other methods have been proposed for filtering velocity data by applying physics-based and smoothing functions in a least-squares sense. One such filter proposed for improving the accuracy of PC-MRI velocity measurements and streamlines minimizes the square of the first spatial derivatives of the velocity field, the terms of (2.2), and the difference between the filtered field and the noisy field. These three constraints, when applied simultaneously, guarantee that the filtered velocity field is unique. This filter was formulated and implemented in three ways: using a Cartesian variable system, an axisymmetric cylindrical coordinate system and a stream function approach. The results of the filter with the broadest application, using a Cartesian coordinate system and no assumption of axisymmetry, were discussed only qualitatively. The more restrictive stream function based filter was reported to reduce the normalized RMS difference between filtered PC-MRI velocity measurements and the CFD generated velocity field of a flow phantom to less than 10% [2]. A viscous energy norm can also be used for filtering as it was in [3] to reconstruct the experimentally measured velocity field of the stationary helical vortex mode of a Taylor–Couette–Poiseuille flow to within 10% of the field predicted by theory. This method, like that in [2] does not directly affect the second derivatives that appear in (2.3). Alternatively the experimental velocity field can be projected onto a space of divergence-free fields obtained either numerically [1, 3] or analytically [90], and both approaches have shown promising results. In this work three methods of reducing the propagation of noise into the estimated pressure field by filtering the velocity field are proposed. One is

a standard image/signal-processing filter and the other two are novel, physics-based filters that rely on a least-squares approach similar to those in [2, 3].

The first approach proposed here is a median filter, which has the benefits of being edge-preserving and easy to implement [91]. These filters are popular in image processing and have been used in some of the other pressure estimation methods [13, 14]. The velocity at each point is replaced by the median of its neighbors within a defined application radius, resulting in a new velocity field \mathbf{V}_{med} . This reduces the effect of spurious noise peaks in the velocity field at the cost of spatial resolution. Using a larger application radius further reduces the spatial resolution.

A physics-based approach is proposed for the development of two additional filters. At this stage, the continuity equation (2.2) has not been explicitly enforced. Physically, it is known that the measured velocity field must satisfy this constraint from Section 2.1.1. The first proposed filter imposes (2.2) in a least-squares sense on $\Omega_{\mathcal{F}}$. An additional penalty function that minimizes the L_2 norm of the difference between the experimental (\mathbf{V}_{exp}) and filtered (\mathbf{V}) velocity fields is added minimize the difference between these fields. Without this second term it is possible for the filter to modify \mathbf{V}_{exp} into a velocity field that satisfies (2.2) but is no longer physically relevant. The function to be minimized is

$$f_1 := |\nabla \cdot \mathbf{V}| + \alpha_1 \|\mathbf{V} - \mathbf{V}_{\text{exp}}\| \quad (2.9)$$

where α_1 is a Lagrange multiplier to be calibrated (see Section 3.2).

Filter 2 minimizes the value of the L_2 norm of the Laplacian of the velocity field in addition to the terms for Filter 1 in equation (2.9). The addition of this term is an attempt to decrease the effect of noise pollution on the computation of the second derivatives in the viscous terms of the NSE (2.3) by selectively removing the noise in these terms. This is a constraint that is used in the implementation of optical flow

algorithms [92]. Thus, the cost function for Filter 2 is

$$f_2 := |\nabla \cdot \mathbf{V}| + \alpha_2 \|\mathbf{V} - \mathbf{V}_{\text{exp}}\| + \gamma_2 \|\nabla^2 \mathbf{V}\| \quad (2.10)$$

where α_2 and γ_2 are Lagrange multipliers to be calibrated (see Section 3.2). Because the three terms of Filter 2 are pushing the cost function toward separate goals, it is unlikely that f_2 will ever reach zero (this is possible if the measurements are noise free and the flow is completely inviscid). Therefore, this term is not attempting to force the Laplacian of the velocity field to be zero, but it is attempting to remove noise in the second spatial derivatives of the velocity field which will need to be calculated in general to estimate the relative pressure field using the method from Section 2.1.2.

Filter 1 and Filter 2, unlike the median filter, do not filter the velocity field at the cost of resolution. The median filter removes noise without adding any additional information (i.e., physical constraints) to the problem; therefore, spatial resolution is traded to remove noise in the velocity field. The proposed physics-based filters bring new information into the problem by enforcing additional constraints on the system, so no resolution must be sacrificed to remove noise from the velocity field.

To determine the relative merit of the filters proposed here, a useful comparison is made to the filter proposed in [1] and the additional filtering terms of [2, 3]. The filtering terms of [2] and [3] can be implemented by modifying the last term on the RHS of (2.10). The filtering term proposed in [2] (2.10) becomes

$$f_3 := |\nabla \cdot \mathbf{V}| + \alpha_3 \|\mathbf{V} - \mathbf{V}_{\text{exp}}\| + \gamma_3 \left| \left(\frac{\partial u}{\partial x} \right)^2 + \left(\frac{\partial u}{\partial y} \right)^2 + \left(\frac{\partial v}{\partial x} \right)^2 + \left(\frac{\partial v}{\partial y} \right)^2 \right| \quad (2.11)$$

where u and v are the x - and y -components of \mathbf{V} , respectively. Using the viscous dissipation term of [3], (2.10) becomes

$$f_4 := |\nabla \cdot \mathbf{V}| + \alpha_4 \|\mathbf{V} - \mathbf{V}_{\text{exp}}\| + \gamma_4 \left| 2\mu \left[\left(\frac{\partial u}{\partial x} \right)^2 + \left(\frac{\partial v}{\partial y} \right)^2 + \frac{1}{2} \left(\frac{\partial u}{\partial y} + \frac{\partial v}{\partial x} \right)^2 \right] \right| \quad (2.12)$$

The filter of (2.11) is identified as $(d/dx)^2$ and the filter of (2.12) as Visc. Diss. in the various figures of Section 3.

It is common in fluid mechanics to apply scaling to parameters which are useful in multiple problems. Doing so eliminates the necessity of optimizing the parameters for each new use. In addition to the physics-based filters themselves, a method of scaling their Lagrange multipliers is proposed so that reoptimization for each new application is avoided. Parameters α_1 , α_2 , α_3 and α_4 are scaled by

$$\alpha_{1,2,3,4} := \alpha'_{1,2,3,4} \frac{\|\nabla \cdot \mathbf{V}_{\text{exp}}\|}{\|\mathbf{V}_{\text{med}} - \mathbf{V}_{\text{exp}}\|} \quad (2.13)$$

where \mathbf{V}_{med} is the median filtered velocity field. The speed of the median filter allows for this normalization to contribute negligibly to the computation time required for the minimization of the cost functions. A scaling factor for γ_2 is similarly defined

$$\gamma_2 := \gamma'_2 \frac{\|\nabla \cdot \mathbf{V}_{\text{exp}}\|}{\|\nabla^2 \mathbf{V}_{\text{exp}}\|} \quad (2.14)$$

The scaling of γ_3 and γ_4 akin to that of γ_2 and in 2D Cartesian coordinates they are

$$\gamma_3 := \gamma'_3 \{ \|\nabla \cdot \mathbf{V}_{\text{exp}}\| \} \left\{ \left| \left(\frac{\partial u}{\partial x} \right)^2 + \left(\frac{\partial u}{\partial y} \right)^2 + \left(\frac{\partial v}{\partial x} \right)^2 + \left(\frac{\partial v}{\partial y} \right)^2 \right| \right\}^{-1} \quad (2.15)$$

and

$$\gamma_4 := \gamma'_4 \{ \|\nabla \cdot \mathbf{V}_{\text{exp}}\| \} \left\{ \left| 2\mu \left[\left(\frac{\partial u}{\partial x} \right)^2 + \left(\frac{\partial v}{\partial y} \right)^2 + \frac{1}{2} \left(\frac{\partial u}{\partial y} + \frac{\partial v}{\partial x} \right)^2 \right] \right| \right\}^{-1} \quad (2.16)$$

respectively.

The filter of [1] was proposed as a method of filtering PC-MRI measurements based on the notion that the measured velocity field must be divergence free. The velocity field is projected onto the space of divergence-free fields using a discrete projector \mathbf{P} that has the form

$$\mathbf{P}\mathbf{V} = \mathbf{V} - \mathbf{G}\mathbf{L}^{-1}\mathbf{D}\mathbf{V} \quad (2.17)$$

where \mathbf{G} is the discrete gradient operator, \mathbf{L} is the discrete Laplacian operator and \mathbf{D} is the discrete divergence operator. $\mathbf{L}^{-1}\mathbf{D}\mathbf{V}$ is found by solving the Poisson equation

$$\begin{aligned} \nabla^2 \mathbf{L}^{-1} \mathbf{D}\mathbf{V} &= \nabla \cdot \mathbf{V} && \text{on } \Omega \\ \mathbf{L}^{-1} \mathbf{D}\mathbf{V} &= 0 && \text{on } \partial\Omega \end{aligned} \tag{2.18}$$

The projection generates a divergence free velocity field, but it does not eliminate all of the noise. It also does not guarantee that the filtered velocity field will still be physically relevant.

2.2.2 Filter Implementation

The filters tested in this work are implemented in manners of varying complexity. For example, the `medfilt2` function in MatLab is used to perform the median filtering whereas each cost function and the PSDF filter require their own special functions. The complexity of the special functions affects the time required to filter the velocity field. Whenever possible MatLab's built-in functions are used to reduce the complexity of the algorithms.

Filter 1, Filter 2, and the filters based on [2] and [3] considerably more computational resources than the median filter. The divergence operator in f_1 and f_2 and the Laplacian operator in f_2 are applied using matrix algebra in custom functions written for the 2D validation. This is done to make use of the speed of MatLab at performing these operations. Derivatives are numerically approximated in the same method as described in Section 2.1.2 for the approximation of \mathbf{b}_F and are detailed in Appendix A. Care is taken on $\partial\Omega_F$, as identified by a mask, not to include points from outside Ω_F . The matrices containing the operators are generated once and are inputs to the functions that evaluate f_1 and f_2 . These matrices are very large and sparse. In 2D, if Ω of size $M \times N$ points, then the coefficient matrices are of size $2(MN) \times 2(MN)$. This can lead to storage issues for large computational domains. The evaluation of f_3 and f_4 is done element by element due to the complexity of their

additional filtering terms. All four cost functions f_1 , f_2 , f_3 and f_4 are minimized using the unconstrained nonlinear minimization algorithm, `fminunc`, in MatLab. This algorithm uses a simple cubic approximation method to minimize the two functions.

The PSDF filter is conveniently implemented using the the same Poisson solver used in the relative pressure field estimation. The algorithm for filtering the velocity field is in Figure 2.3. This system has Dirichlet boundary conditions which require sine transforms and inverse transforms and do not require the extra steps necessary for the solution of a Neumann problem. This version of the Poisson solver is described in detail in Appendix B.2.

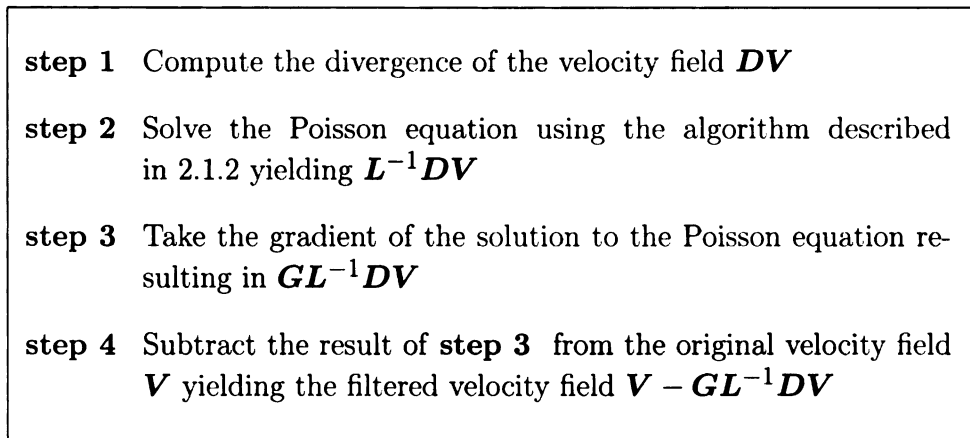


Figure 2.3. The algorithm for projecting the noisy velocity field into the space of divergence-free fields as proposed in [1].

2.3 Mathematical Phantoms & Validation

Several components of the the proposed method require validation and optimization as a sort of ‘proof of concept’ to assess which approach is best. This section is divided into three parts. First, a mathematical phantom of suitable complexity to test the algorithms is described. The second part of the section outlines a testing procedure for determining the effect of resolution and embedding on the estimation of the pressure

field. In [4] the proposed algorithm for estimating the relative pressure field was tested for robustness to noise at a higher resolution than that expected for PC-MRI data of the carotid artery. No results were reported on the effect of resolution or the size of Ω relative to Ω_F . In the final part the procedures for optimizing the filter parameters described in Section 2.2.1, the tests used to determine the method's robustness to noise at a realistic resolution for PC-MRI measurements of the carotid artery, determining the effect of the proposed filters and testing the scaling of the filter parameters proposed in Section 2.2.2.

2.3.1 Mathematical Phantoms

Examination of the usefulness of the relative pressure estimation method proposed in this work, like all numerical methods, requires comparing results to an example with known properties. This can be done by an experiment on a physical system performed with additional measurements provided by a trusted second method as in [13, 14, 17, 20], experiments on a physical phantom with well understood behavior like in [12], or numerical experiments using either commercial CFD software [11], or a mathematical phantom of sufficient complexity [4]. Experiments with physical phantoms and PC-MRI are expensive and noise free tests cannot be guaranteed. Comparing a numerical solution to CFD in a complex geometry allows for noise-free tests, but questions about the accuracy of the CFD model can still be raised. Instead, a mathematical phantom of a suitably complex system with a known analytical solution is chosen for use here because of the flexibility it allows in the testing and the simplicity of its implementation.

For the validation tests, a mathematical phantom of Couette flow between rotating cylinders is used. Certain compromises must be made when choosing a mathematical phantom. Couette flow between rotating cylinders provides a nontrivial system with an analytical solution for both the pressure and velocity fields. The cylindrical shape

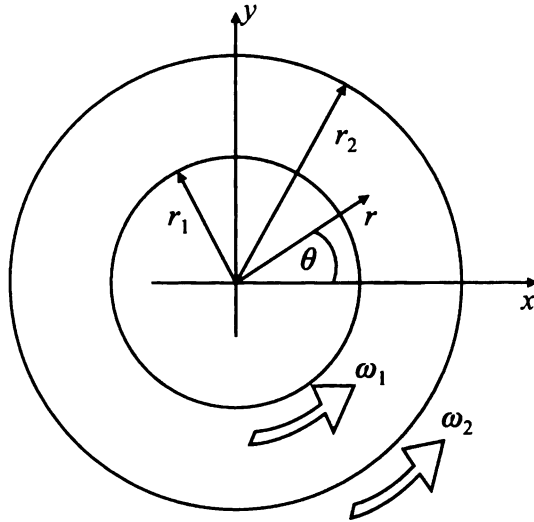


Figure 2.4. A schematic of the Couette flow system used in the 2D validation experiments with the important geometric features identified.

of this system also allows for identification of potential issues with the calculation of \mathbf{b}_F near boundaries that are similar to those anticipated in vessel geometry. The two boundaries in the system, on the inner and outer cylinder walls, also test the effect of multiple, moving embedded boundaries on the PPE solver. This is expected *in vivo* for data collected above the internal/external bifurcation in the carotid artery. However, one of the characteristics of this flow field is that the viscous terms of (2.3) are identically zero. This is a compromise that must be made to ensure that the majority of the components of the algorithms are tested sufficiently. The derivation of the flow field from (2.3) is detailed in Appendix C.1. The final results are presented in this section. The Cartesian velocity field (u, v) in polar coordinates (r, θ) is given by:

$$\begin{cases} u(r, \theta) = -\left(Ar + \frac{B}{r}\right) \sin \theta \\ v(r, \theta) = \left(Ar + \frac{B}{r}\right) \cos \theta \end{cases} \quad (2.19)$$

where $r := \sqrt{x^2 + y^2}$, $\theta := \arctan(y/x)$ and

$$A = \frac{\omega_2 r_2^2 - \omega_1 r_1^2}{r_2^2 - r_1^2}$$

$$B = \frac{r_1^2 r_2^2 (\omega_1 - \omega_2)}{r_2^2 - r_1^2}$$

r_1 and r_2 are the radii of the inner and outer cylinders, respectively, and ω_1 and ω_2 are their respective angular velocities, see Figure 2.4 for a schematic of the system. Though the flow is 1D in polar coordinates, the transformation to Cartesian coordinates generates a flow with non-zero gradients in both directions for at least one component of velocity at every point. Figure 2.5(a) is a vector plot of half of the analytical velocity field, \mathbf{V}_A , which illustrates its complexity. An analytical solution for the relative pressure field is similarly obtained:

$$P(r) = \rho \left(\frac{A^2 r^2}{2} + 2 A B \ln r - \frac{B^2}{2 r^2} + C \right) \quad (2.20)$$

where C is an arbitrary integration constant, such that P is the relative pressure field as defined earlier. An example of half of the analytical pressure field relative to its spatial average, P_A , and normalized by its root-mean-square, $P_{A,\text{RMS}}$, on Ω_F (RMS) is found in Figure 2.5(b).

A second simple phantom is necessary to determine if any bias has been introduced by the combination of filter and mathematical phantom. Poiseuille channel flow is a simple system with a 1D analytical velocity field and linear pressure gradient, see Figure 2.6 for a schematic. The Cartesian velocity field is

$$u(y) = \frac{-12Q_c\mu}{h^3} (y^2 - hy) \quad (2.21)$$

where u is the velocity component along the x -direction, Q_c is the volume flow rate per unit depth and h is the height of the channel. Figure 2.7(a) is a vector plot of the analytical velocity field at an arbitrary x -location, \mathbf{V}_A . The analytical pressure field is

$$P(x) = -\frac{12Q_c\mu}{h^3} (x - x_o) \quad (2.22)$$

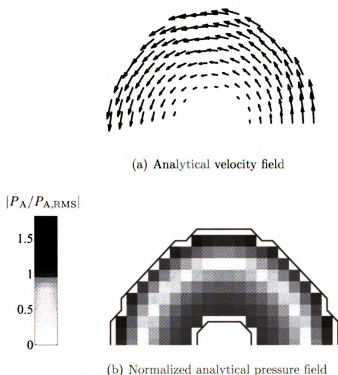


Figure 2.5. Example sections of the analytical solution for the Couette flow mathematical phantom: (a) the velocity field, \mathbf{V}_A ; (b) the magnitude of the pressure field relative to its spatial average, P_A , and normalized by its RMS, $P_{A,RMS}$, on Ω_F .

where x_o is an arbitrary datum. An example of the analytical pressure field relative to its spatial average, P_A , and normalized by its root-mean-square, $P_{A,RMS}$, on Ω_F (RMS) is found in Figure 2.7(b). In this mathematical phantom the viscous terms of (2.3) are not identically zero, see Appendix C.2 for a detailed derivation.

The mathematical phantoms described here are implemented using custom functions in MatLab. The physical domain in which they are contained is fixed, but the resolution in all directions is variable to facilitate the resolution experiments described in Section 2.3.2. These functions also generate the mask used in the algorithms of Section 2.1.2 and Section 2.2.2 for identifying points on Ω_F .

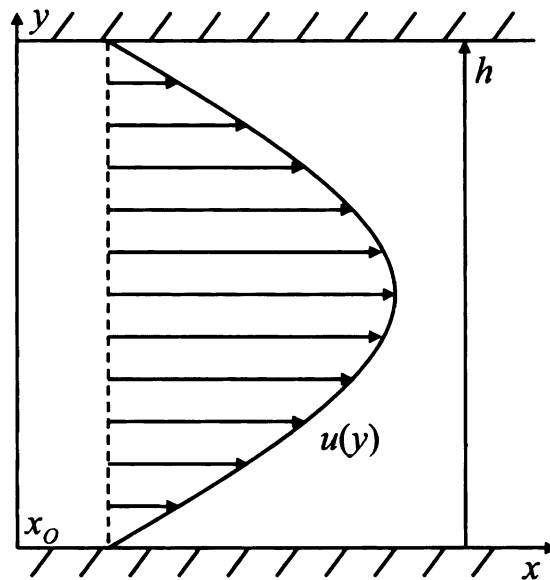


Figure 2.6. A schematic of the Poiseuille flow system used in the 2D validation experiments with the important geometric features identified.

2.3.2 Resolution and Embedding Experiments

As stated above, no testing of the algorithm in Section 2.1.2 for robustness to changes in resolution or the level of embedding have been, to the best of the author's knowledge, published. In [4] the algorithm was tested on a phantom similar to the 2D Couette flow between rotating cylinders used here with a grid size of 256×256 . The carotid artery has a diameter of ~ 10 mm and PC-MRI velocity data is expected to have an in-plane voxel size of ~ 0.5 mm \times 0.5 mm. Thus, approximately twenty voxels are expected across the vessel. This low resolution could be enhanced using interpolation to increase the number of data points on Ω_F , but upsampling like this with noisy data is problematic. The effect resolution has on the algorithm is investigated here to determine if upsampling can be avoided. The resolution of the velocity data cannot be guaranteed to be isotropic, so tests on the effect of anisotropic resolution in both directions are undertaken here to explore its influence on the estimated pressure field. The size of Ω can also be an issue from a computational point of view.

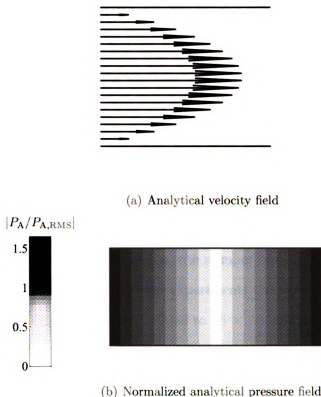


Figure 2.7. Example sections of the analytical solution for the Poiseuille flow mathematical phantom: (a) the velocity field at an arbitrary axial location, \mathbf{V}_A ; (b) the magnitude of the pressure field relative to its spatial average, P_A , and normalized by its RMS, $P_{A,RMS}$, on Ω_F .

For maximum efficiency Ω should be as small as possible. An investigation into the relative size of Ω compared to Ω_F is performed to determine a reasonable relative size for Ω or if an optimum size exists. In 3D, a single contiguous domain is desired to eliminate the difficulties of point registration. It is expected that the carotid artery will not remain centered in each plane of this domain. Therefore, the effect of the placement of Ω_F within Ω is also investigated.

The behavior of the pressure estimating algorithm with respect to resolution is required before any of the other experiments can be performed. If the estimation can

be performed accurately in noise-free conditions, the rest of the tests should be conducted at realistic PC-MRI resolutions. However, if the algorithm does not output results of sufficient accuracy at realistic resolutions without noise, then additional steps, like the upsampling mentioned above, will be required for the following experiments. Only the image matrix size and not the size of the voxels was reported in [4], so determining the resolution in that study is impossible. For these resolution experiments, the 2D mathematical phantom described in Section 2.3.1 is used. The parameters used to generate the mathematical velocity and pressure fields for these experiments are in Appendix D. The size of $\Omega_{\mathbb{F}}$ and the size of Ω relative to $\Omega_{\mathbb{F}}$ are both fixed. To vary the resolution, the number of points in the computational mesh is increased or decreased. In these experiments the resolution is isotropic. The size of the mesh is varied from 2048×2048 to 16×16 which corresponds to relative pixel size, $\eta = \Delta x / 2r_2$, of 7×10^{-4} and 0.09, respectively. PC-MRI data of the carotid artery, with $\eta = 0.05$, falls within this range. The metric ($\bar{\varepsilon}$) used to determine the accuracy of the algorithms is

$$\bar{\varepsilon} = \frac{\text{RMS}(P_{\text{num}} - P_{\text{A}})}{\text{RMS}(P_{\text{A}})} \quad (2.23)$$

where P_{num} is defined as before and P_{A} is the analytical pressure field minus its spatial average (i.e., P_{A} is an absolute pressure field). At $\eta = 0.05$, $\bar{\varepsilon}$ is less than 1% (see Section 3.1). This is deemed sufficient for the rest of the experiments to be conducted at this resolution without upsampling.

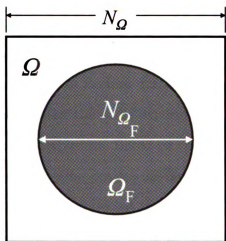
It is possible that the measured velocity field will have an anisotropic resolution and that this will affect the estimated pressure field. The Poisson equation solver used here relies on a FFT to decouple the two spatial directions and was derived to be robust to anisotropic resolution over a regular domain. However, the additional steps required for solutions on an irregular domain have the potential to favor isotropic resolution for more accurate solutions. Because the FFT is applied in one direction, the effect anisotropic resolution on the irregular solution can be dependent on which

direction has lower resolution. Two tests are carried out to determine these effects. In the first, the relative pixel size in the direction of the FFT, $\eta_{\text{FFT}} = \Delta x_{\text{FFT}}/(2r_2)$, is held constant at $\eta_{\text{conv}} = 0.0056$ while $\eta_{\text{sol}} = \Delta x_{\text{sol}}/2r_2$, the relative pixel size in the solution direction, is allowed to vary from 0.0004 to 0.09. The second test holds $\eta_{\text{sol}} = \eta_{\text{conv}}$ and allows η_{FFT} to vary from 0.0004 to 0.09. The fixed relative pixel size was chosen such that it fell in the converged region as determined by the initial isotropic resolution tests. The size of Ω relative to Ω_{F} in both directions is fixed.

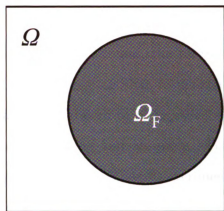
Determining the effect of embedding on the algorithm is important not only from the standpoint of the accuracy of the solution, but also from a computational standpoint. The size of Ω relative to Ω_{F} is referred to as level of embedding (Γ) and is defined as

$$\Gamma = \frac{N_{\Omega}}{N_{\Omega_{\text{F}}}} - 1 \quad (2.24)$$

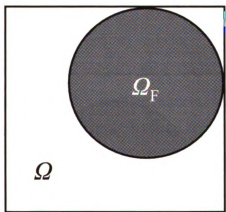
where N_{Ω} is the number of voxels across Ω and $N_{\Omega_{\text{F}}}$ is the number of voxels across the diameter of the outer cylinder in the 2D mathematical phantom, see Figure 2.8(a) for an illustration. This experiment is performed with $N_{\Omega_{\text{F}}} = 20$ and $\eta = 0.05$. Experiments are conducted with Ω_{F} located in three different regions of Ω to simulate the expected meandering of Ω_{F} in an *in vivo* data set. In the first experiment Ω_{F} is embedded centered in Ω as shown in Figure 2.8(a) while in the other two experiments Ω_{F} is embedded centered in one direction but off center in the other, see Figure 2.8(b), and in the corner of Ω , see Figure 2.8(c). For all three experiments the level of embedding is allowed to vary from 0% to 250%. Based on the results of this experiment (see Section 3.1) a level of embedding of 25% is deemed suitable for the rest of the 2D experiments.



(a)



(b)



(c)

Figure 2.8. Illustrations useful in visualizing the embedding tests, (a) the definition of the level of embedding Γ and an schematic of the fluid domain Ω_F embedded in the center of the extended computational domain Ω , (b) Ω_F embedded centered in one direction and off-center in the other and (c) Ω_F embedded in a corner of Ω .

2.3.3 Filter Parameter Estimation and Noise Experiments

Once the determination of how the method is affected by resolution has been made, the level of embedding and the location of Ω_F within Ω , tests to determine the usefulness of filtering the velocity field before estimating the relative pressure field can begin. This is done in two steps. In the first step the same set of experimental parameters as were used in the tests of Section 2.3.2 to optimize scaled versions filter parameters of Section 2.2.2. Once the scaled parameters are found, the filters are tested using the same experimental parameters over a range of SNR to determine their effectiveness. Based on this testing, three filters are chosen to be representative of the filtering options in terms of speed of implementation and accuracy. These representatives are put through another set of noise tests using different experimental parameters to test the scaling of the filter parameters.

The SNR for experiments with a noisy velocity field is defined as

$$\text{SNR} = \frac{\text{RMS}(\mathbf{V}_A)}{\text{RMS}(\mathbf{V}_{\text{exp}} - \mathbf{V}_A)} \quad (2.25)$$

where RMS is defined as before, \mathbf{V}_{exp} is the noisy experimental velocity and \mathbf{V}_A is the analytical velocity field. Noise is added to the \mathbf{V}_A with the `randn` function in MatLab which generates random numbers with a Gaussian distribution and the level is adjusted based on the desired SNR.

The two proposed physics-based filters and two of those described in the literature require the tuning of the parameters α_1' , α_2' and γ_2' , α_3' and γ_3' , and α_4' and γ_4' . This is done using the worst conditions considered here (SNR=5) and optimizing the parameters such that the pressure solution resulting from the filtered velocity fields has the smallest $\bar{\epsilon}$. These parameters are optimized empirically to determine the order of magnitude for the penalty terms in the cost functions. It is expected that these terms should be small compared to the term representing (2.2) so this level of optimization is deemed sufficient because it is unlikely that a set of parameters can

be found that will be optimal for all noisy velocity fields. The optimized values of the parameters, $\alpha_1' = 0.1$, $\alpha_2' = 0.01$ and $\gamma_2' = 0.53$, are used in the application of the two proposed physics-based filters Filter 1 and Filter 2, see Section 2.2.2. The optimized parameters for the filters from the literature, $\alpha_3' = 0.01$ and $\gamma_3' = 0.1$ and $\alpha_4' = 0.0001$ and $\gamma_4' = 0.1$, are used in the application of those filters.

The first set of tests with the noisy velocity fields are used to determine the effect of decreasing SNR on the algorithm and the effectiveness of the filters using the initial filter parameters. It was shown in [4] that the algorithm was robust to noise in 2D experiments using a mathematical phantom at a higher resolution than that of interest here. White Gaussian noise is added to the analytical velocity field at SNRs of 5, 10, 15, 20, 25 and 30 and the resulting noisy velocity field is input either directly into the algorithm of Section 2.1.2 or filtered before being input into the algorithm. A PC-MRI data set is expected to have a SNR between 5 and 10. However, with advances in sequence design or technology it is possible for this to increase, so the higher SNRs are tested to verify the filters do not enhance the proportion of noise in these conditions. Several noisy velocity fields are used to test each of the filters and the relative pressure estimation without a filter and the results are averaged.

A method of determining the quality of the filtered velocity field is of use as a way to directly compare the effect of the filters on the velocity field rather than on their effect on the resulting estimated relative pressure field. Such a method was described in [1] to evaluate the velocity filter proposed in that work. The performance factor F of a filter is defined as

$$F = \frac{\|\mathbf{V}_A - \mathbf{V}_f\|}{\|\mathbf{V}_A - \mathbf{V}_{\text{exp}}\|} \quad (2.26)$$

where \mathbf{V}_f is the filtered velocity field. F is the ratio of the error in the filtered velocity field to the error in the noisy velocity field. If $F < 1$, then the filter is effective in moving the the velocity field towards the true field, whereas $F > 1$ indicates that the filter is no longer effective and is moving the velocity field away from the true

field. This metric is used in the initial noise experiments as an additional method of differentiating between the proposed filters and evaluating their performance as compared to those filters from the literature.

A second set of experiments with noisy velocity data are performed using only the median filter and the two proposed physics-based filters proposed here. Based on the initial set of experiments, the three proposed filters illustrate the range of filtering options adequately. This second set of experiments are carried out using a different set of flow parameters to determine the appropriateness of the proposed scaling of the filter parameters. The second set of experimental parameters attempt to match the scale of the velocities that occur within the carotid artery. Setting experimental parameters that attempt to more closely match those in arterial flow is somewhat difficult with the Couette flow mathematical phantom used here. There are no direct connections in terms of length scales between this phantom and Carotid flow which makes matching the Reynold's number (Re) complex. Additionally, arterial flow is normally described, as stated in 2.1.1, with Wo not Re . As time dependence is not being considered at this stage, an attempt is made to mathematically approximate a flow with a more accurately scaled velocity field than that in the initial set of tests by matching an average Re rather than Womersley numbers for the two flows. To more closely match the behavior of blood, its average density and viscosity are used. The average Re in the Couette flow phantom defined as

$$Re_C = \frac{\rho}{\mu} (r_2 + r_1) \frac{\omega_1 r_1 + \omega_2 r_2}{2} \quad (2.27)$$

where the subscript C indicates the Couette flow phantom, is approximately matched to an average reynolds number in carotid artery flow defined as

$$Re_a = \frac{\rho D_a \bar{U}_a}{\mu} \quad (2.28)$$

where the subscript a indicates the approximate conditions in the carotid artery. This is not a direct scaling between the two flows. The mathematical phantom parameters

used to match these numbers are in Appendix D. The matching of these two numbers allows for only a very rough approximation of the velocity field which is adequate for testing the scaling of the filter parameters.

These two sets of experiments represent only one possible flow geometry. As discussed in Section 2.3.1, certain compromises are made in the selection of the Couette flow mathematical phantom. In particular the viscous terms are identically zero in the analytical description of the phantom. The constraint in Filter 2 that minimizes the Laplacian of the noisy velocity field is attempting accomplish this same requirement. This indicates a potential bias in the results of this work. To determine the importance of this bias, a set of simple experiments were undertaken using the Poiseuille flow phantom. The flow domain is embedded in the center of an extended domain as in the Couette noise experiments, noise is added to the analytical velocity field at $\text{SNR} = 5 - 20$ and the filter parameters optimized for the Couette flow mathematical phantom are used. The median filter, Filter 1, Filter 2, $(d/dx)^2$ Filter and the Visc. Diss. Filter are tested and compared to the relative pressure estimation with no filtering. The mathematical phantom parameters used are in Appendix D.

CHAPTER 3

Results & Discussion

The results of the 2D validation of both stages of the proposed methodology are presented in this chapter. The results of these experiments serve as a ‘proof of concept’ for the method. Without them it is unreasonable to assume the method would work in more realistic conditions or with velocity fields derived from real PC-MRI measurements. Starting with the resolution and embedding experiments described in Section 2.3.2, each additional experiment relies on the results of those before it. For this reason, this section is divided into three parts. The first two parts mirror the presentation of the experimental methodology in Section 2.3. Tabulated versions of the graphical results presented in these two sections are in Appendix E. The final section is dedicated to a discussion of the results.

3.1 Influence of Spatial Resolution and Embedding Strategy

The examination of the influence of isotropic spatial resolution, represented here by the relative voxel size η , on the normalized relative RMS error, $\bar{\epsilon}$, reveals that the relative pressure field estimation is second-order accurate, as shown in Figure 3.1.

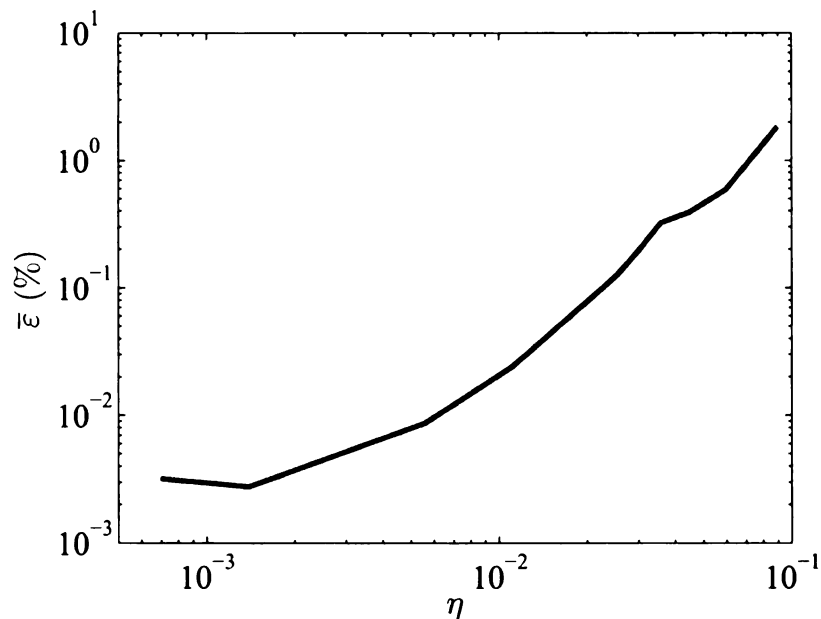


Figure 3.1. Plot of the normalized relative RMS error, $\bar{\epsilon}$, of the estimated relative pressure field for Couette flow with no noise added as a function of the the relative pixel size, $\eta = \Delta x/2r_2$.

More importantly, $\bar{\epsilon} \approx 1\%$ for the resolution expected for MRI studies of the carotid artery, $\eta = 0.05$. Thus, it is not necessary to artificially increase the resolution of the velocity field with interpolation in the remaining experiments.

Anisotropic resolution has a different effect depending on which direction is coarser in resolution. Above $\chi_{\text{sol}} = 10$ and $\chi_{\text{FFT}} = 10$, $\bar{\epsilon}$ differs between the two directions, see Figures 3.2(a) and (b), respectively. For $\chi_{\text{sol}} > 10$ $\bar{\epsilon}$ is larger compared to the opposite, $\chi_{\text{FFT}} > 10$, maximum $\bar{\epsilon} = 2.6\%$ and maximum $\bar{\epsilon} = 1.3\%$, respectively. Below $\chi_{\text{sol}} = 10$ and $\chi_{\text{FFT}} = 10$, the solver behaves identically to decreasing values of χ_{sol} and χ_{FFT} with a clear minimum $\bar{\epsilon}$ at $\chi_{\text{sol}} = \chi_{\text{FFT}} = 1$.

The effect of embedding Ω_{F} in increasingly larger Ω is shown in Figure 3.3. If Ω_{F} is embedded in the center of Ω , $\bar{\epsilon}$ decays monotonically towards an asymptotic value of 0.8% with increasing Γ . In addition, Figure 3.3 indicates that there is an error

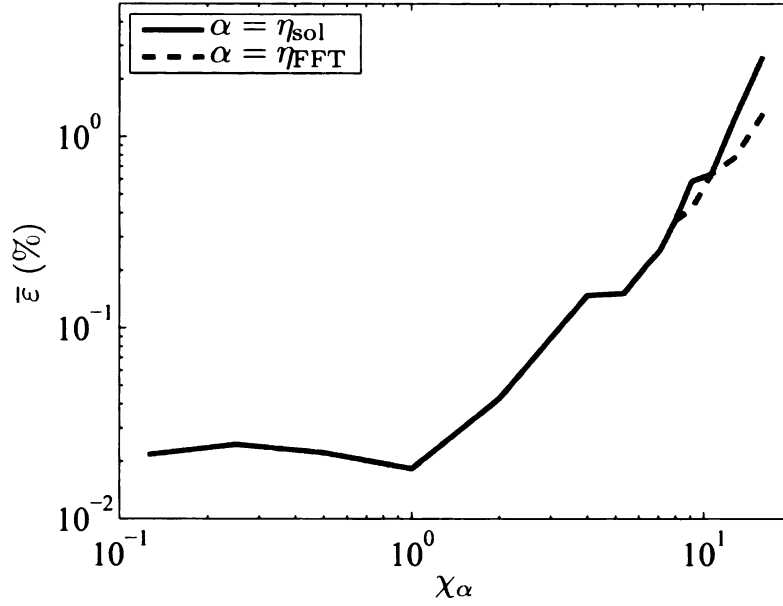


Figure 3.2. Plot of the normalized relative RMS error, $\bar{\varepsilon}$, of the estimated relative pressure field for Couette flow with no noise added as a function of $\chi_{\alpha} = \alpha/\eta_{conv}$.

minimum ($\bar{\varepsilon} \approx 0.9\%$) at Γ of approximately 45% when $\Omega_{\mathbf{F}}$ is located in the corner of Ω and at about 110% for the case when $\Omega_{\mathbf{F}}$ is located off to one side of Ω . All in all, the effects of the embedding are relatively negligible ($\bar{\varepsilon} < 1\%$) provided the embedding level is greater than 20%. A Γ of 25% is used for all other experiments presented here.

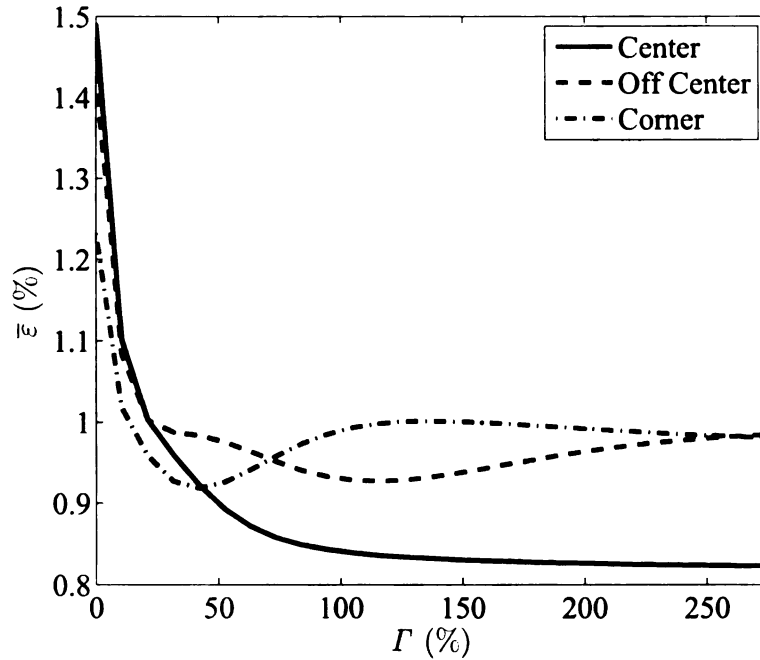
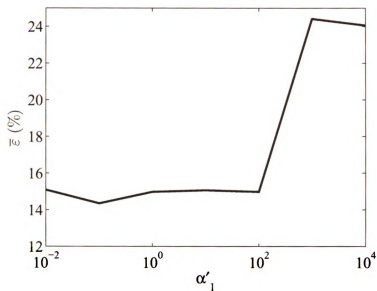


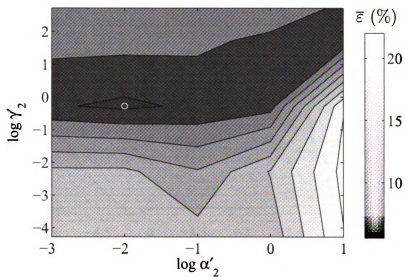
Figure 3.3. Plot of the normalized relative RMS error, $\bar{\epsilon}$, of the estimated relative pressure field for Couette flow with no noise added as a function of the embedding level Γ with a 20×20 , which corresponds to $\eta = 0.05$, flow domain Ω_F .

3.2 Calibration and Performance of Proposed Noise Filters

The Lagrange multipliers used for Filter 1 (α_1), Filter 2 (α_2 and γ_2) and the modified form of Filter 2 using the filtering terms of [2] (α_3 and γ_3) and [3] (α_4 and γ_4), are calibrated by optimizing the results for the worst noise conditions considered here (SNR = 5). The normalized relative RMS error for the estimated relative pressure field, $\bar{\epsilon}$, is plotted against $\alpha'_{1,2}$ and γ'_2 in Figure 3.4(a,b). The optimal performance is obtained for $\alpha'_1 = 0.1$ and $\alpha'_2 = 0.01, \gamma'_2 = 0.53$, which are the conditions used henceforth. Similar plots for the filters using the terms of [2], see (2.11), and [3], see (2.12), are shown in Figure 3.5(a,b). The optimal performances of these filters is

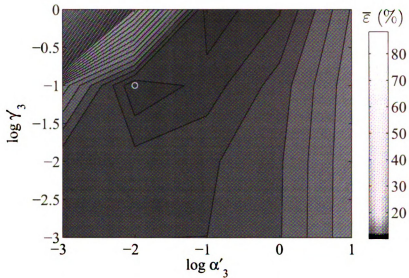


(a) Filter 1 calibration

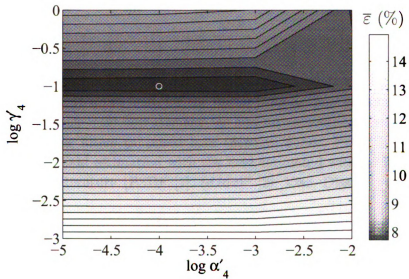


(b) Filter 2 calibration

Figure 3.4. Plot of the average normalized relative RMS error, $\bar{\varepsilon}$, of the estimated relative pressure field for the initial Couette flow experimental parameters, a resolution of $\eta = 0.05$ on a 20×20 flow domain Ω_F , an embedding level $\Gamma = 25\%$ and $\text{SNR} = 5$, as a function of: (a) α'_1 for Filter 1; (b) α'_2 and γ'_2 for Filter 2, the minimum is circled.



(a) $(d/dx)^2$ calibration



(b) Viscous dissipation calibration

Figure 3.5. Contour plots of the average normalized relative RMS error, $\bar{\epsilon}$, of the estimated relative pressure field for the initial Couette flow experimental parameters, a resolution of $\eta = 0.05$ on a 20×20 flow domain Ω_F and an embedding level $\Gamma = 25\%$ and SNR = 5, as a function of: (a) α'_3 and γ'_3 for the filter with filtering term proposed in [2]; (b) α'_4 and γ'_4 for filter with the filtering term proposed in [3]. The minimum is circled in both figures.

obtained using $\alpha'_3 = 0.01, \gamma'_3 = 0.1$ and $\alpha'_4 = 0.0001, \gamma'_4 = 0.1$ for (2.11) and (2.12), respectively.

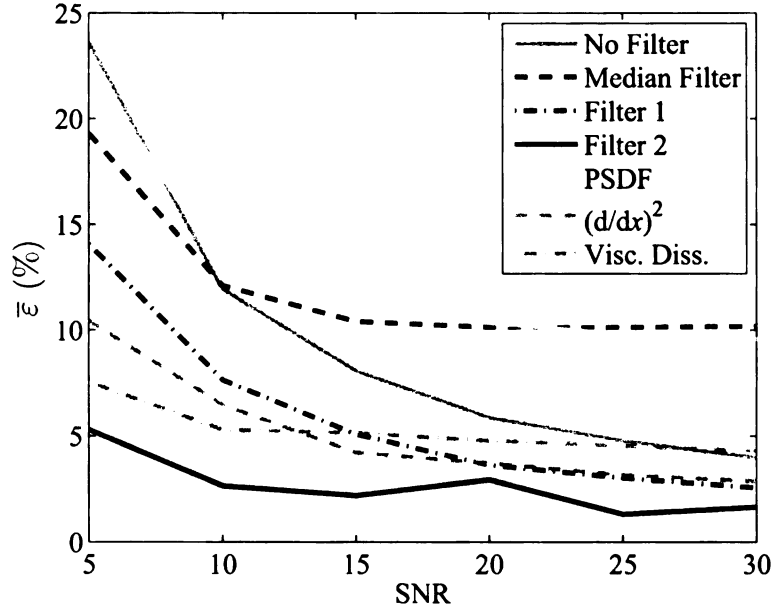


Figure 3.6. Plot comparing the average normalized relative RMS error, $\bar{\epsilon}$, in the estimated relative pressure field, for the initial Couette flow parameters, a resolution of $\eta = 0.05$ on a 20×20 flow domain Ω_F and an embedding level $\Gamma = 25\%$, after applying the three filters proposed here (Median Filter, Filter 1, Filter 2) to the relative pressure field estimation with the field estimated with no filtering and three filters from the literature (PSDF [1], $(d/dx)^2$ [2], Visc. Diss. [3]) over the range of SNR tested.

The normalized relative RMS error, $\bar{\epsilon}$, obtained before and after filtering is plotted against SNR in Figure 3.6. The tests were carried out using the initial set of experimental parameters with resolution of $\eta = 0.05$, on a 20×20 flow domain Ω_F embedded in a 25×25 computational domain Ω . The embedding level $\Gamma = 25\%$ is deemed sufficient in view of the results presented in Section 3.1. For all filters, $\bar{\epsilon}$ decreases with increasing SNR, as expected. Moreover, the two physics-based filters proposed here outperform the median filter and the PSDF filter of [1] over the full range of SNR values tested. Filter 2 outperforms all filters tested throughout the

range of SNR tested. Both the median filter and PSDF filter become ineffective at low SNR, SNR = 10 and SNR = 7.5, respectively. The other filters all remain effective through the SNR tested. For Filter 1, $\bar{\varepsilon}$ decreases from an average of 14.3% at SNR = 5 to an average of 2.5% at SNR = 30. For the filter of [2], $\bar{\varepsilon}$ goes from 10.4% to 2.8% for the same SNR range. For the filter of [3], $\bar{\varepsilon}$ goes from 7.5% to 4.3%. For Filter 2, $\bar{\varepsilon}$ goes from 5.3% to 2%.

The dependence of the estimated relative pressure field, $P_{\text{num}}(x, y)$, on the filtering of the noisy experimental velocity data with SNR = 5 is illustrated in Figure 3.7. Pixelated images of the magnitude of the normalized error distribution, $\varepsilon(x, y)$, are plotted when no filtering is applied in Figure 3.7(a) and then for the median filter in Figure 3.7(b), Filter 1 in Figure 3.7(c), Filter 2 in Figure 3.7(d) and filters using the terms of [2] in Figure 3.7(e) and [3] in Figure 3.7(f). The results of the PSDF filter are not included because the reduction in error is indistinguishable. The improved performance of Filter 2 is demonstrated by the clearly lower magnitude of $\varepsilon(x, y)$ and the significantly lower relative RMS error ($\bar{\varepsilon}$) as compared to the results for the other filters (by factor of 1.35 w.r.t. the filtering term of [3], 1.84 w.r.t. the filtering term of [2], 2.7 w.r.t. Filter 1 and factor of 3.64 w.r.t. the median filter).

The performance factor F is plotted against SNR in Figure 3.8 for all filters tested here with the initial set of Couette flow experimental parameters. Without filtering F is expected to be 1, $F < 1$ indicates that the filtered velocity field is closer to the true velocity field and $F > 1$ means the filtered velocity field is further from the true velocity field than the original noisy field. The two physics-based filters proposed here, Filter 1 and Filter 2, both have F values less than 1 for the entire range of SNR tested. The median filter and the PSDF filter both begin to push the filtered velocity field away from the true velocity field after an SNR of 5. The filter using the term of [2], $(d/dx)^2$, remains effective through the range of SNR tested, but F approaches one at SNR = 30. The filter using the term of [3] remains effective

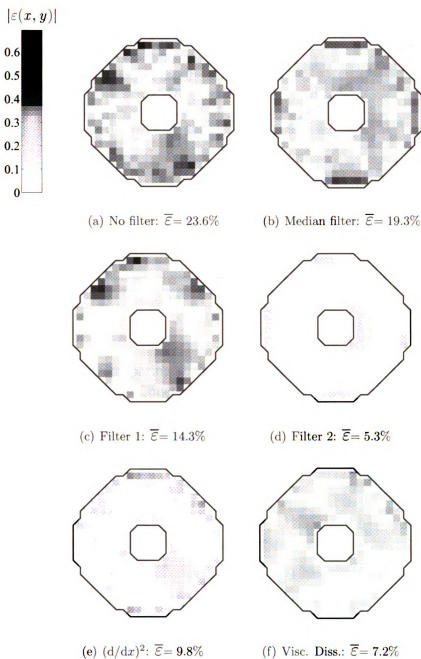


Figure 3.7. Sample images of the magnitude of the normalized relative error distribution, $|\varepsilon(x, y)|$, for the estimated relative pressure fields obtained using the initial Couette flow experimental parameters, a resolution of $\eta = 0.05$ on a 20×20 flow domain Ω_F , an embedding level $\Gamma = 25\%$ and $\text{SNR} = 5$ (a) no filter; (b) a median filter with radius 1 pixel; (c) Filter 1; (d) Filter 2; (e) a filter using the term of [2]; and (f) a filter using the term of [3] on the noisy velocity field. The normalized RMS error, $\bar{\varepsilon}$, is specified for each case.

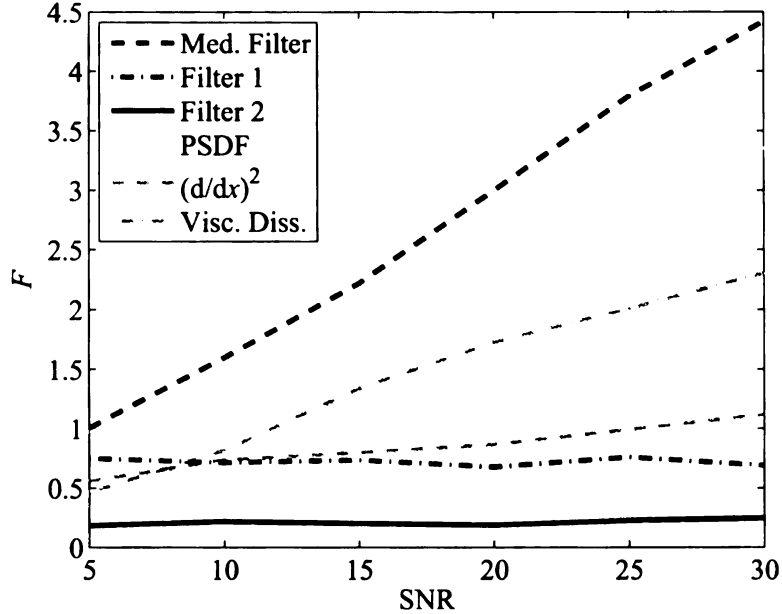


Figure 3.8. Plot comparing the average performance factor F to SNR for all filters tested using the initial Couette flow experimental parameters, a resolution of $\eta = 0.05$ on a 20×20 flow domain $\Omega_{\mathcal{F}}$ and an embedding level $\Gamma = 25\%$. Note that the median filter, the PSDF method and the filter using the viscous dissipation term of [3] all become ineffective by $\text{SNR} = 15$.

through an SNR of 15.

The effect of filtering on the noisy experimental velocity data with $\text{SNR} = 5$ is illustrated in Figure 3.9. Vector plots of the analytical velocity field over half of $\Omega_{\mathcal{F}}$ are superposed with the velocity field resulting with the application of no filtering in Figure 3.9(a), median filtering in Figure 3.9(b), Filter 1 in Figure 3.9(c), Filter 2 in Figure 3.9(d), a filter using the term of [2] in Figure 3.9(e) and a filter using the term of [3] in Figure 3.9(f). The results of the PSDF filter are not included because the reduction in error is indistinguishable. The F value for the respective filtered velocity fields are indicated beneath the individual vector plots. The efficacy of Filter 2 at producing a velocity field that is closer to the true velocity field is evidenced by the difference in F as compared to the other filters (a factor of 4.17 smaller w.r.t. Filter 1,

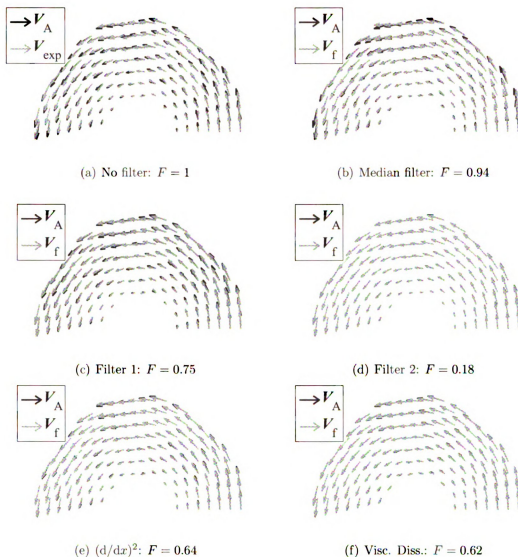


Figure 3.9. Sample velocity vector fields of the initial Couette flow experimental parameters, a resolution of $\eta = 0.05$ on a 20×20 flow domain Ω_F , an embedding level $\Gamma = 25\%$ and $\text{SNR} = 5$ illustrating the effect of (a) no filter (\mathbf{V}_{exp}); (b) a median filter with radius 1 pixel; (c) Filter 1; (d) Filter 2; (e) the filter using the term of [2], see (2.11); and (f) the filter using the term of [3], see (2.12), on the noisy velocity field. The subscript f indicates the filtered field. The performance factor, F , is specified for each case.

a factor of 4.9 w.r.t. the term of [3], a factor of 5 w.r.t. the term of [2] and a factor of 5.22 smaller w.r.t. the median filter).

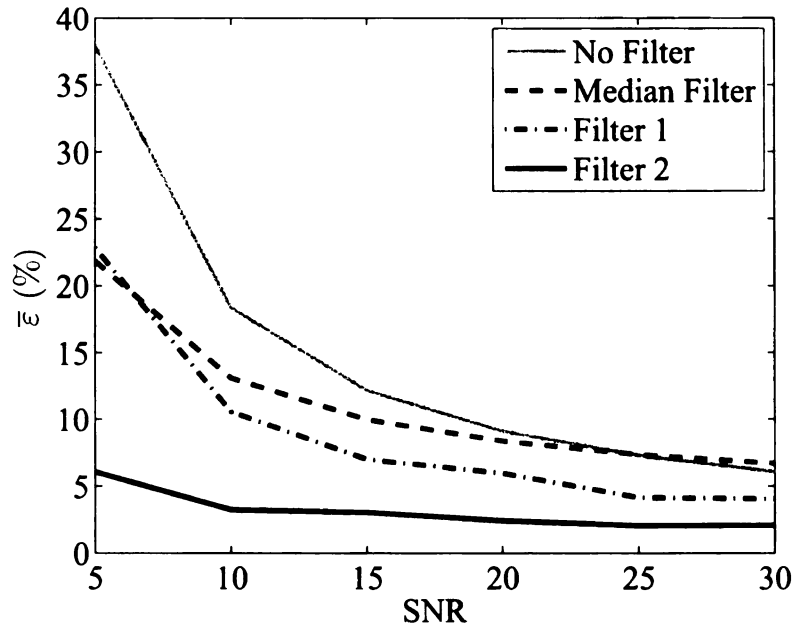


Figure 3.10. Plot of the average normalized relative RMS error, $\bar{\epsilon}$, in the estimated relative pressure field versus SNR for the more realistic Couette flow parameters, resolution $\eta = 0.05$ on a 20×20 flow domain Ω_F and an embedding level of $\Gamma = 25\%$, comparing the results of the three filters proposed here to the result with no filter over the range of SNR tested.

The second set of noise experiments using the optimized scaled filter parameters on the Couette flow mathematical flow phantom with a more realistically scaled velocity field show that the scaling of the filter parameters is appropriate, see Figure 3.10 for a plot of the RMS error $\bar{\epsilon}$ versus SNR. In this case the PPE solver does amplify the noise to a greater extent, $\bar{\epsilon} = 38\%$, than in the previous set of experiments, $\bar{\epsilon} = 24.3\%$. The filters remain effective in reducing the propagation of noise into the estimated relative pressure field reducing $\bar{\epsilon}$ to 21.9% using the median filter, 22.9% using Filter 1, and 6.1% using Filter 2. In these experiments the median filter out performs Filter 1 by 1% and continues to be effective until $\text{SNR} = 20$. Filter 1 becomes more effective

than the median filter as the SNR increases and remains effective through the range of SNR tested with $\bar{\varepsilon} = 4\%$ at SNR = 30 compared to 6.7% for the median filter and 6% without a filter. Filter 2 decreases $\bar{\varepsilon}$ to 2% at SNR = 30.

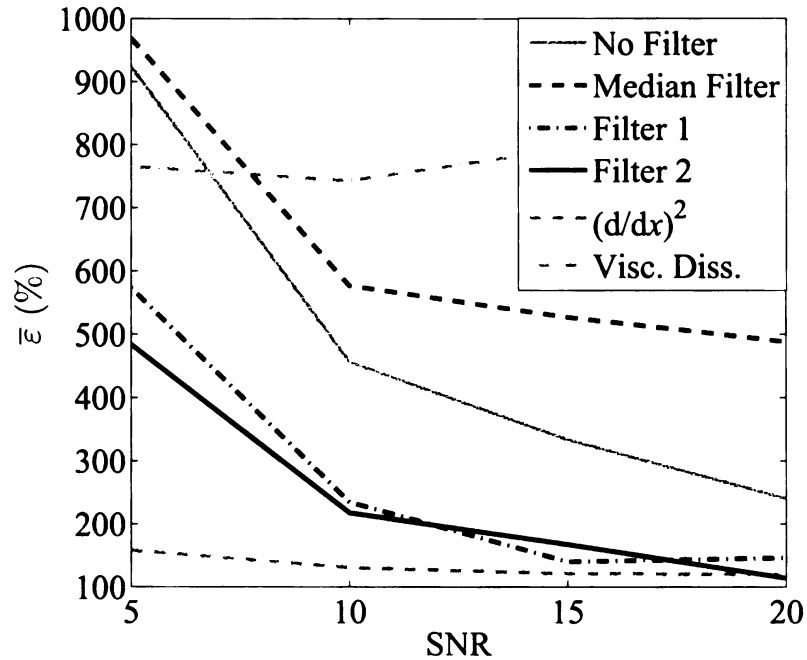


Figure 3.11. Plot of the average normalized relative RMS error, $\bar{\varepsilon}$, in the estimated relative pressure field versus SNR for the Poiseuille flow parameters, resolution $\eta = 0.05$ on a 20×20 flow domain Ω_F and an embedding level of $\Gamma = 25\%$, comparing the results of the three filters proposed here to the result with no filter and two filters from the literature $(d/dx)^2$ [2], Visc. Diss. [3]) over the range of SNR = 5 – 20.

The set of noise experiments using the optimized filter parameters on the Poiseuille flow mathematical flow phantom demonstrate that the solver has difficulty with noise in such simple flows, see Figure 3.11 for a plot of the RMS error $\bar{\varepsilon}$ versus SNR. In this case the PPE solver does amplify the noise to a greater extent, $\bar{\varepsilon} = 924\%$, than in the previous experiments with Couette flow, $\bar{\varepsilon} = 24.3 - 38\%$. The median filter is entirely ineffective. The filter with the additional term of [3] based on viscous dissipation also reduces the error at SNR = 5 ($\bar{\varepsilon} = 765\%$), but this filter also becomes ineffective

before $\text{SNR} = 10$. Filter 1, Filter 2 and the filter with the additional term of [2] that minimizes the square of the first spatial derivatives of the velocity field remain effective through the range of SNR tested. For this flow, the filtering term of [2] is the most effective reducing $\bar{\epsilon}$ to 131% at $\text{SNR} = 5$ whereas Filter 1 reduces it to 573% and Filter 2 reduces it to 483%.

3.3 Discussion

The investigation of the influence of spatial resolution and embedding level Γ on the estimation of the relative pressure field reveals that the PPE solution technique is capable of generating accurate relative pressure fields at spatial resolutions that are consistent with PC-MRI of small blood vessels. Based on the examination of effect of anisotropic resolution, the Poisson solver combined with embedding is affected by changes in the coarseness of the resolution and which direction is coarser. Greater coarseness in the direction of the FFT does not affect the accuracy of the estimated pressure field as much as coarseness in the solving direction when the resolutions differ by a factor of 10 or more. In situations such as these the Poisson solver can be adjusted to maximize the accuracy by applying the FFT in the direction of coarser resolution. It is clearly beneficial to use isotropic resolution as this maximizes the accuracy of the estimated pressure field. This fact is more important in three-dimensional velocity fields measured by MRI where it is more common to have anisotropic resolution due to the multi-slice acquisition of the spatial information (preferred to lengthier 3D data acquisition). The accuracy of the solution is affected by the value for Γ , especially when Ω_F is not embedded at the center of Ω , and there exists optimal embedding levels that provide more accurate solutions. From a practical aspect however, these optimal embedding levels may require an excessively large computational domain Ω , which then requires longer computational times and/or more computational power. Normalized RMS errors of the estimated relative pressure field on the order of 1% or less ($\bar{\varepsilon} \leq 1\%$) are achievable for realistic in-plane resolutions and embedding levels $\Gamma > 20\%$ in the absence of noise in the velocity input.

For PC-MRI, realistic RMS noise levels are about 10% to 20%, corresponding to $\text{SNR} = 5$ to 10. In the initial set of noise tests, see Figure 3.6, the curves for $\bar{\varepsilon}$ vs. SNR for no filter and the median filter cross at $\text{SNR} = 10$, which reveals that the median filter actually amplifies the propagation of the experimental noise into

the estimated relative pressure field for $\text{SNR} > 10$. Similarly, the PSDF filter of [1] begins to amplify the propagation of noise for $\text{SNR} > 7.5$. By implementing two physics-based filters on the experimental velocity field with a normalized RMS noise of 20%, the normalized RMS error in the estimated relative pressure field is reduced from $\bar{\varepsilon} = 23.6\%$ to 14.3% by Filter 1 and down to only 5% by Filter 2, which is quite encouraging. Implementing the filter of [2], see (2.11), reduces the error to 10.4%, and implementing the filter of [3], see (2.12), reduces the error to 7.5%. Filter 1 requires less computational time than Filter 2: 30 min compared to 75 to 90 min on a Dell Optiplex 755 with a 2.99 GHz processor, 1.96 GB of RAM, cache speed of 3 GHz, and cache size of 4 MB (Dell Computers, Round Rock, TX). Thus, the significant gain in accuracy provided by Filter 2 vs. Filter 1 is inversely proportional to their relative computational time, which is an expected trade-off. The filters using the terms of [2] and [3] are implemented in the same manner as Filter 2 and have the same computational time. Because Filter 2 as proposed here is more accurate than either of these two filters with the same computational time, it is clear that they offer no advantage over Filter 2.

The comparison of the F values of the filtered velocity fields is also revealing. Over the range of SNR tested the two physics-based filters outperformed all other filters tested. In some cases the effect of the filter on the velocity field can be inferred from Figure 3.6. For instance, it is apparent that both the projection onto the space of divergence free fields, PSDF, proposed in [1] and the median filter become ineffective in moving the noisy velocity field towards the true velocity field because their relative pressure field $\bar{\varepsilon}$ curves cross the curve for estimation with no filter. From Figure 3.8 the F values for these two filters start at an average of $F = 0.95$ and $F = 0.98$, respectively, for $\text{SNR} = 5$ and quickly become greater than one. The results of the PSDF method do not agree with those published at similar SNR, $F = 0.88$ in [4] compared to an average of $F = 0.95$ here for $\text{SNR} = 5$. However, those experiments

were performed with a larger computational domain (32×32). The PSDF is fast (0.01 sec), produces a velocity field closer to the true velocity field than the median filter and is implemented using a similar Poisson solver to that used for the pressure estimation, but the resulting relative pressure field estimation is worse than that of a median filtered velocity field. The other two filters proposed in the literature have similar, though less severe, effects on the velocity field. Based on Figure 3.6 both of the physics-based filters proposed here, Filter 1 and Filter 2, should generate velocity fields that are nearer the true field because their $\bar{\epsilon}$ curves stay near or below the expected error for the range of SNR tested. Again the results in Figure 3.8 agree with this expectation. The performance of Filter 1 decreases from an average of $F = 0.75$ to $F = 0.69$ over the range of SNR tested while the performance of Filter 2 increases from an average of $F = 0.18$ to $F = 0.25$. It is more difficult to determine the effectiveness of the filters using the terms of [2], $(d/dx)^2$, and [3], Visc. Diss. based solely either on $\bar{\epsilon}$ or F . Over the lower portion of the range of SNR tested, both of these filters generate velocity fields that better estimate the relative pressure field than the noisy velocity field as compared to PSDF, median filtering and Filter 1 according to Figure 3.6. The F value at SNR = 5 for these filters are on average $F = 0.56$ and $F = 0.46$ for the filtering terms of [2] and [3], respectively, which agrees with the $\bar{\epsilon}$ interpretation. According to the F values of these two filters, they start becoming less effective than Filter 1 at SNR ≈ 10 whereas according to $\bar{\epsilon}$ they become less effective between SNR = 15 and 20. The F value of the filter using the term of [2] remains less than one only through SNR = 25, but its $\bar{\epsilon}$ curve remains below that for no filtering throughout the range of SNR tested. The filter using the term of [3] becomes ineffective at SNR ≈ 12.5 according to its F value which is before the SNR that its $\bar{\epsilon}$ curve crosses that of Filter 1 and near the SNR where it crosses the curve of the filter with the term of [2]. At SNR = 25 its $\bar{\epsilon}$ curve crosses the curve of estimation without a filter and its $F = 2$.

The second set of noise tests demonstrate that the method and the optimized scaled filter parameters do transfer to more realistic conditions. While the RMS error in the estimated relative pressure field increases by 60%, from 23.6% to 38%, between the initial experiments and these experiments when no filter is applied to the velocity field at $\text{SNR} = 5$, it only increases 20% from 5% to 6%, when Filter 2 is applied. This indicates that the proposed scaling is appropriate. However, the results of applying Filter 1 seem to indicate the opposite. At $\text{SNR} = 5$ the median filter actually outperforms Filter 1 and the $\bar{\epsilon}$ increases from 14.3% in the initial set of tests to 22.9% in the second set. This increase of $\approx 60\%$ mirrors that of the case with no filter, but it does not mirror the increase in the value of α_1 which increases from an average of 0.65 to 89. More likely the additional filtering term of minimizing the Laplacian of the velocity field is an effective way of combating the propagation of noise from the velocity field to the estimated relative pressure field. The approximate optimization of α'_1 used in Filter 1 is also not as precise as that for α'_2 and γ'_2 used in Filter 2. Fine-tuning the value of α'_1 may increase its accuracy. The median filter remains effective over a greater range of SNR in these experiments decreasing $\bar{\epsilon}$ through $\text{SNR} = 20$ as opposed to $\text{SNR} = 10$ in the initial set of tests. Both Filter 1 and Filter 2 remain effective through the range of SNR tested as they did in the initial set of experiments. The times to execute Filter 1 and Filter 2 in these experiments remains the same as it was in the initial experiments.

The final set of experiments with a mathematical phantom, Poiseuille flow, demonstrate that the proposed filters reduce the error in the estimated relative pressure field when compared to the estimation without filtering in a second flow system. The mathematical simplicity of the Poiseuille flow belies the difficulty encountered by the proposed method in estimating the relative pressure field from the noisy velocity field. There is a drastic increase of $\bar{\epsilon}$ in the estimated relative pressure fields with and without first filtering the velocity field. Estimating a linear gradient using

Fourier methods is difficult because of the practical limitation to use a finite rather than infinite representation. The solver is capable of accurately estimating the relative pressure field with no noise in the velocity field at these resolution conditions ($\bar{\varepsilon} = 0.2\%$). The additions of noise to the velocity field, however, allows the pressure estimation to converge to a periodic field which is preferred by this type of solver. It is worth noting that the filters, with the exception of the filter using the term of [3], follow the same trend of accuracy improvement as was seen in the Couette mathematical phantom experiments. The median filter is effective initially, but becomes ineffective before $\text{SNR} = 10$. Filter 1, Filter 2 and the filter using the term of [2] all reduce the error through the range of SNR tested. Unlike before, the simpler of the two filters proposed here, Filter 1, is either as or more effective at higher SNR than Filter 2. Also unlike the Couette experiments, the filter using the term of [2] is the best performer throughout the range of SNR tested. Interestingly, the filter using the term of [3] increases $\bar{\varepsilon}$ compared to the case with no filter at higher SNR which is a behavior not seen in the previous experiments. Because the error was so large across all cases in using this phantom, it is difficult to tell if any bias was introduced by the combination of filter and mathematical phantom. The fact that Filter 2 continues to be one of the better performers indicates that it has the potential to be a useful filter in cases where the flow physics are less well understood.

These ‘proof of concept’ experiments to determine if this type of two-stage method is worth investigating further are encouraging. PC-MRI resolution conditions do not greatly hamper the PPE solver’s ability to estimate an accurate relative pressure field in zero noise conditions. The level of embedding, I , and the position of Ω_F within Ω do factor greatly into the accuracy of the solution, and the level of embedding required to generate a solution that is within 1% relative RMS error of the true relative pressure field does not require Ω to be excessively larger than Ω_F . Based on the two sets of noise testing, the scaling of the filter parameters is appropriate. Additionally, the

Filter 2 proposed here outperforms all of the other filters tested in the more complex mathematical phantom. Filter 1 is faster than Filter 2 and the filters using the terms of [2] and [3], but it produces a less accurate velocity field than Filter 2 and struggles in conditions a with more realistically scaled velocity field. The results of this 2D validation show that the two-stage method in general, and using either one of the two physics-based filters proposed here in particular, is a reasonable approach to estimating the relative pressure field from noisy velocity fields.

CHAPTER 4

Conclusions

Engineering is a discipline whose goal is to find the best path from problem to solution. In many cases this is an iterative process where the ideal path is found through a series of small improvements. Here the problem being considered directly is estimating the relative pressure field from noisy velocity measurements, but the underlying goal is to provide a diagnostic tool. The work presented here represents one iteration toward the best solution for both of these aspirations. The previous iterations include the minimally invasive blood flow assessments reviewed in Section 1.3 and the various algorithms for estimating the relative pressure field reviewed in Section 1.2. This step adds a noise filter between the velocity measurements and the pressure estimation to improve the resulting relative pressure field. The results of this work show that the inclusion of either one of two proposed physics-based filters as well as two filters from the literature improve the accuracy of the estimated relative pressure field. In this chapter the insight into the problem gained in this iteration of estimating relative pressure fields and the future of the proposed method are presented.

4.1 Insight

It is important to understand how an algorithm will behave in the presence of various complicating factors before it is used to interpret real-world measurements. The mathematical phantom experiments were useful in elucidating the complexities of the problem of estimating the relative pressure field on an irregular domain. The effect of spatial resolution on the algorithm is the first issue that many numerical methods are required to overcome. The results of the presented experiments have demonstrated that the pressure estimation algorithm is adequately capable of resolving relative pressure fields accurately at the relatively coarse resolution achievable in clinical PC-MRI. However, it is recommended that isotropic resolution be used when possible. Embedding the irregular domain as done here is useful for simplifying the application of the boundary conditions, but its effect on the accuracy of the solution has not been published. The results presented here show that using a computational domain that is 25% larger than the major dimension of the irregular physical domain produces suitable results in noise-free conditions. These results provide the necessary level of knowledge of the behavior of the algorithm to then proceed with tests using noisy velocity fields.

Though the resolution and embedding tests discussed in Section 3.1 demonstrate that the pressure algorithm is accurate at the low resolution expected for PC-MRI, the noise tests are equally demonstrative of the inaccuracies that are introduced by noisy velocity measurements. The first stage of the proposed method, namely removing noise in the velocity field using one of three proposed filters or filters described in the literature, proves useful in reducing the negative effects of noisy data. Of the tested filters, the filter that simultaneously applies in a least-squares sense the continuity equation for an incompressible fluid, a constraint on the variation between the filtered velocity field and the noisy one and an additional constraint that limits the size of the Laplacian of the velocity field, Filter 2, performs the best. It succeeds in reducing

the error in the estimated pressure field from an average of 23.6% with no filter to an average of 5.3% with filtering at a realistic resolution in the worst conditions tested. This non-negligible improvement was also demonstrated in a second set of experiments with different flow parameters. The trend was also seen in a set of experiments using a second mathematical phantom. By comparing these results to those of Filter 1, which does not apply the additional term and improves the pressure estimation to an average error of 14.6%, it is evident that removing noise in the Laplacian is useful. Other second terms such as those proposed in [2] and [3] when applied using scaling factors like those proposed here are also effective in mitigating the pollution of the estimated relative pressure field with noise from the measured velocity field. However, accuracy is not the only factor to be considered when comparing the filters, the time required to complete the filtering and estimation of the pressure field is also of importance. At this point, it is uncertain how accurate the pressure field needs to be to fulfill the eventual goal of providing a useful diagnostic technique. For this reason, it is not prudent to ignore the capabilities of Filter 1 which is faster to implement than filters with additional terms.

Using a physics-based approach in the design of the filters is an obvious improvement over *ad hoc* methods like median filtering. An understanding of the principles of fluid mechanics that govern blood flow in vessels like the carotid artery is necessary for these approaches to be workable. Minimizing the continuity equation for a noisy velocity field results in a velocity field that satisfies the conservation of mass, but there is no guarantee that the resulting field is still relevant to the physical system. Even though they are polluted by noise, the measured velocity fields still represent a system that satisfies all governing equations. When removing noise from this field the filtered field should not stray far from this starting point. From these physical insights the cost function of Filter 1, see Section 2.2.1, was written. Filter 2 adds an additional constraint that is designed to allow for a more accurate characterization

of the effect of viscosity. Though it is not directly based on a governing equation, the minimization of the Laplacian of the velocity field is a method of removing noise from the flow field that directly affects the estimation of the viscous terms in the NSE. It is reasonable to assume that the velocity field does not contain discontinuities or large spikes at this level, so this additional constraint seeks to eliminate them. Other terms can also be applied if *a priori* knowledge of the flow field or experience dictates physical constraints separate from those tested here. The difficulty encountered by the method in estimating the relative pressure field from a noisy velocity field with no filtering in the Poiseuille flow experiments underscores the importance of filtering stage. The scaling of the filter parameters proposed here appears appropriate and is a useful way to avoid reoptimizing the parameters for each new application. From these physical principles, as well as the results of the resolution and embedding experiments, this two-stage methodology is proposed for estimating the relative pressure field from a velocity field at conditions that are realistic for clinical PC-MRI experiments.

4.2 Future Work

This work endeavors towards providing the first step of a noninvasive technique for the diagnosis of the physiological relevance of arteriosclerotic stenoses in the carotid artery. To that end, a two-stage method is proposed to estimate the relative pressure field from a noisy velocity field. While the velocity field by itself does provide enough information to calculate such potentially important parameters as wall shear stress and oscillatory shear index, the relative pressure field is also necessary before any serious investigation into the dynamics of the vessel wall can be investigated. It is these dynamics that are expected to provide information about the danger associated with a particular stenosis. The extension of the two-stage method proposed here to the evaluation of the dynamics of the vessel wall is an obvious next step.

Before that step can be taken some refinement to the details of the method are desired. The time required to implement either of the two physics-based filters proposed here is one area of concern. Different minimization algorithms, rewriting the functions in a lower-level computing language like C or Fortran and faster computers are all possible solutions to this problem. Another area with potential for improving the method concerns the parameters used in the implementation of the filters. To this point the parameters are only roughly optimized. It is unlikely that there exists a set of exactly optimized parameters that will provide ideal results independent of the SNR. However, there is the possibility that further optimization of these parameters could lead to better results than those presented here especially in the case of Poiseuille flow. It is possible that some sort of experiment with a physical phantom will be necessary to determine the best set of parameters to be used. This potential for improvement does not preclude the discussion, in general terms, of the future use of the proposed method that follows.

Experiments with 2D mathematical flow phantoms are presented here, but blood flow in the carotid artery and the dynamics of the vessel wall are 3D and time-varying. It is difficult to construct a mathematical phantom with an analytical solution for both the velocity field and pressure field that is rich in all three spatial dimensions and as well as the temporal dimension. Thus, testing of the method proposed here is difficult to implement in higher dimensions. However, the time-varying velocity field is not a factor in the design of either of the two proposed physics-based filters and its effects are only present in the acceleration term in the NSE. Additionally, the pressure field is calculated relative to its own spatial average not the time average. Therefore, once the time derivative of the velocity field is estimated, the 3D pressure field that represents each time step can be calculated as a stand-alone system. Once the method is expanded and validated in 3D, tests on a simple time-varying flow, such as the Womersley flow, can be used to determine the effect of time the derivative on

the pressure estimation which allows for the focus to be shifted to the determination of the characteristics of the vessel wall.

Interaction between the wall and the blood flowing through a vessel will have an impact on the estimation of the pressure field. The experiments carried out in this work did use flow systems with moving boundaries, but not systems with changing volumes. While it is reasonable to assume that the volume of a segment of a blood vessel will be unchanged between cardiac cycles, it is not reasonable to assume that it will remain unchanged during a cycle. If the properties of the vessel wall are to be understood, some coupling between the methodology presented here and the appropriate tissue mechanics models will be required. This is the next major step in developing the minimally invasive tool that is the underlying desire of this work.

APPENDIX A

Finite Difference Schemes

Finite difference schemes use Taylor series expansions to approximate the derivative of a function at a point. In this work there are no mixed derivatives so this appendix focuses on the derivation of schemes for derivatives in a single direction. The Taylor series expansion of a function $f(x)$ about the point $f(x + \Delta x)$ is

$$f(x + \Delta x) = \sum_{n=0}^{\infty} \frac{(\Delta x)^n}{n!} \frac{d^{(n)} f}{dx^{(n)}} \Big|_x \quad (\text{A.1})$$

If f is evaluated on a discrete grid with a fixed spacing of Δx between points, then the index notation $i \pm n$, where $n = 0, 1, 2, \dots, \infty$, can be used to expand the first few terms of the summation of (A.1) at the point $(i + 1)$

$$f_{(i+1)} = f_i + \Delta x \frac{df}{dx} \Big|_i + \frac{(\Delta x)^2}{2} \frac{d^2 f}{dx^2} \Big|_i + \frac{(\Delta x)^3}{6} \frac{d^3 f}{dx^3} \Big|_i + \frac{(\Delta x)^4}{24} \frac{d^4 f}{dx^4} \Big|_i + o(\Delta x^5) \quad (\text{A.2})$$

A similar expansion for the point $i - 1$ yields

$$f_{(i-1)} = f_i - \Delta x \frac{df}{dx} \Big|_i + \frac{(\Delta x)^2}{2} \frac{d^2 f}{dx^2} \Big|_i - \frac{(\Delta x)^3}{6} \frac{d^3 f}{dx^3} \Big|_i + \frac{(\Delta x)^4}{24} \frac{d^4 f}{dx^4} \Big|_i + o(\Delta x^5) \quad (\text{A.3})$$

By subtracting (A.3) from (A.2) and rearranging terms an approximation of the first derivative at point i is possible using the value of f at the locations $i + 1$ and $i - 1$

$$\frac{df}{dx} \Big|_i = \frac{f_{(i+1)} - f_{(i-1)}}{2\Delta x} + o(\Delta x^2) \quad (\text{A.4})$$

Similarly, by adding (A.2) to (A.3) an approximation of the second derivative of f at point i is possible using the value of f at $i + 1$, i and $i - 1$.

$$\frac{d^2 f}{dx^2}|_i = \frac{f_{(i+1)} - 2f_i + f_{(i-1)}}{(\Delta x)^2} + o(\Delta x^2) \quad (\text{A.5})$$

Both (A.4) and (A.5) are second-order accurate central-difference schemes. The second-order accuracy stems from the expected magnitude of the first term of the Taylor series that has been which is of the order of the size of the step in x squared. First-order accurate schemes can also be derived from (A.2) and (A.3)

$$\frac{df}{dx}|_i = \frac{f_{(i+1)} - f_i}{\Delta x} + o(\Delta x) \quad (\text{A.6})$$

$$\frac{df}{dx}|_i = \frac{f_i - f_{(i-1)}}{\Delta x} + o(\Delta x) \quad (\text{A.7})$$

These are a forward scheme, (A.6), and a backward scheme, (A.7). Schemes like these are of use on the boundaries of a discrete domain.

If second-order accurate forward and backward schemes are desired or second derivatives are required, then more points are necessary. The expansions for points $(i + 2)$ and $(i + 3)$ are

$$f_{(i+2)} = f_i + 2\Delta x \frac{df}{dx}|_i + \frac{(2\Delta x)^2}{2} \frac{d^2 f}{dx^2}|_i + \frac{(2\Delta x)^3}{6} \frac{d^3 f}{dx^3}|_i + \frac{(2\Delta x)^4}{24} \frac{d^4 f}{dx^4}|_i + o(\Delta x^5) \quad (\text{A.8})$$

and

$$f_{(i+3)} = f_i + 3\Delta x \frac{df}{dx}|_i + \frac{(3\Delta x)^2}{2} \frac{d^2 f}{dx^2}|_i + \frac{(3\Delta x)^3}{6} \frac{d^3 f}{dx^3}|_i + \frac{(3\Delta x)^4}{24} \frac{d^4 f}{dx^4}|_i + o(\Delta x^5) \quad (\text{A.9})$$

respectively. A second-order accurate forward scheme for a first derivative is found using (A.2) and (A.8)

$$\frac{df}{dx}|_i = \frac{-f_{(i+2)} + 4f_{(i+1)} - 3f_i}{2\Delta x} + o(\Delta x^2) \quad (\text{A.10})$$

These points are also required to find a first-order accurate forward scheme for the second derivative

$$\frac{d^2 f}{dx^2}|_i = \frac{f_{(i+2)} - 2f_{(i+1)} + f_i}{(\Delta x)^2} + o(\Delta x) \quad (\text{A.11})$$

The point approximated in (A.9) is necessary to find the second-order forward scheme of the derivative in (A.11)

$$\frac{d^2 f}{dx^2}|_i = \frac{-f_{(i+3)} + 4f_{(i+2)} - 5f_{i+1} + 2f_i}{(\Delta x)^2} + o(\Delta x^2) \quad (\text{A.12})$$

A similar approach is used to find backward equivalents of (A.10), (A.11) and (A.12).

The expansions about points $(i - 2)$ and $(i - 3)$ are

$$f_{(i-2)} = f_i - 2\Delta x \frac{df}{dx}|_i + \frac{(2\Delta x)^2}{2} \frac{d^2 f}{dx^2}|_i - \frac{(2\Delta x)^3}{6} \frac{d^3 f}{dx^3}|_i + \frac{(2\Delta x)^4}{24} \frac{d^4 f}{dx^4}|_i + o(\Delta x^5) \quad (\text{A.13})$$

and

$$f_{(i-3)} = f_i - 3\Delta x \frac{df}{dx}|_i + \frac{(3\Delta x)^2}{2} \frac{d^2 f}{dx^2}|_i - \frac{(3\Delta x)^3}{6} \frac{d^3 f}{dx^3}|_i + \frac{(3\Delta x)^4}{24} \frac{d^4 f}{dx^4}|_i + o(\Delta x^5) \quad (\text{A.14})$$

respectively. The backward scheme equivalents of (A.10), (A.11) and (A.12) are

$$\frac{df}{dx}|_i = \frac{f_{(i-2)} - 4f_{(i-1)} + 3f_i}{2\Delta x} + o(\Delta x^2) \quad (\text{A.15})$$

$$\frac{d^2 f}{dx^2}|_i = \frac{f_{(i-2)} - 2f_{(i-1)} + f_i}{(\Delta x)^2} + o(\Delta x) \quad (\text{A.16})$$

and

$$\frac{d^2 f}{dx^2}|_i = \frac{-f_{(i-3)} + 4f_{(i-2)} - 5f_{(i-1)} + 2f_i}{(\Delta x)^2} + o(\Delta x^2) \quad (\text{A.17})$$

For those special cases where the proximity of $\partial\Omega_F$ prevents the use of any of the above approximations, a central difference approximation that allows for variations in Δx is required. To start, substitute (A.4) into (A.2)

$$f_{(i+1)} = f_i + \Delta x \frac{f_{(i+1)} - f_{(i-1)}}{2\Delta x} + \frac{(\Delta x)^2}{2} \frac{d^2 f}{dx^2}|_i + \frac{(\Delta x)^3}{6} \frac{d^3 f}{dx^3}|_i + o(\Delta x^4) \quad (\text{A.18})$$

Rearranging yields a new expression for $f_{(i+1)}$ in terms of f_i and $f_{(i-1)}$

$$f_{(i+1)} = 2f_i - f_{(i-1)} + (\Delta x)^2 \frac{d^2 f}{dx^2}|_i + \frac{(\Delta x)^3}{3} \frac{d^3 f}{dx^3}|_i + o(\Delta x^4) \quad (\text{A.19})$$

For the proposes of this derivation it is convenient to once again use $(x \pm n\Delta x)$ instead of $(i \pm n)$. Let us now assume that the grid spacing in the direction of $(x + \Delta x)$ is

different from the spacing in the direction of $(x - \Delta x)$, denoted as Δx_+ and Δx_- , respectively, and both of these spacings are different than the regular spacing on the rest of the grid, Δx . Rewriting (A.2) using this new notation, solving for the second derivative and substituting (A.4) yields

$$\frac{d^2 f}{dx^2} = \frac{2}{(\Delta x_+)^2} \left[f_{(x+\Delta x_+)} - f_x - \Delta x_+ \left(\frac{f_{(x+\Delta x)} - f_{(x-\Delta x)}}{2\Delta x} \right) \right] \quad (\text{A.20})$$

A new expression for $f_{(x+\Delta x)}$ in terms of $f_{(x+\Delta x_+)}$ and $f_{(x-\Delta x)}$ is found by substituting (A.20) into (A.19)

$$f_{(x+\Delta x)} = \frac{2 \left\{ \left[1 - \left(\frac{\Delta x}{\Delta x_+} \right)^2 \right] f_x + \left(\frac{\Delta x}{\Delta x_+} \right)^2 f_{(x+\Delta x_+)} + \frac{1}{2} \left(\frac{\Delta x}{\Delta x_+} - 1 \right) f_{(x-\Delta x)} \right\}}{1 + \frac{\Delta x}{\Delta x_+}} \quad (\text{A.21})$$

Following a similar procedure, a new expression for $f_{(x-\Delta x)}$ in terms of $f_{(x-\Delta x_-)}$ and $f_{(x+\Delta x)}$ is

$$f_{(x-\Delta x)} = \frac{2 \left\{ \left[1 - \left(\frac{\Delta x}{\Delta x_-} \right)^2 \right] f_x + \left(\frac{\Delta x}{\Delta x_-} \right)^2 f_{(x-\Delta x_-)} + \frac{1}{2} \left(\frac{\Delta x}{\Delta x_-} - 1 \right) f_{(x+\Delta x)} \right\}}{1 + \frac{\Delta x}{\Delta x_-}} \quad (\text{A.22})$$

By substituting (A.22) into (A.21) and vice versa new expressions for $f_{(x+\Delta x)}$ and $f_{(x-\Delta x)}$ in terms of the ratios $R_+ = \frac{\Delta x}{\Delta x_+}$ and $R_- = \frac{\Delta x}{\Delta x_-}$, $f_{(x+\Delta x_+)}$ and $f_{(x-\Delta x_-)}$ are obtained

$$f_{(x+\Delta x)} = 2 \left\{ \left[1 - (R_+)^2 + \frac{R_+ - 1}{1 + R_-} (1 - R_-^2) \right] f_x + (R_+)^2 f_{(x+\Delta x_+)} + \frac{R_+ - 1}{1 + R_-} (R_-)^2 f_{(x-\Delta x_-)} \right\} \left\{ (1 + R_+) \left[1 - \frac{(R_+ - 1)(R_- - 1)}{(R_+ + 1)(R_- + 1)} \right] \right\}^{-1} \quad (\text{A.23})$$

and

$$f_{(x-\Delta x)} = 2 \left\{ \left[1 - (R_-)^2 + \frac{R_- - 1}{1 + R_+} (1 - R_+^2) \right] f_x + (R_-)^2 f_{(x-\Delta x_-)} + \frac{R_- - 1}{1 + R_+} (R_+)^2 f_{(x+\Delta x_+)} \right\} \left\{ (1 + R_-) \left[1 - \frac{(R_+ - 1)(R_- - 1)}{(R_+ + 1)(R_- + 1)} \right] \right\}^{-1} \quad (\text{A.24})$$

Substituting (A.23) and (A.24) into (A.4) and (A.5) yields approximations for first and second derivatives in areas where the schemes that assume a fixed grid are not possible. When these schemes are applied in any of the algorithms in this work it is assumed that $\Delta x_{\pm} = 0.5\Delta x$ and that the velocity at that point is zero. This allows for a rudimentary approximation of the derivatives in virtually all regions of $\Omega_{\mathcal{F}}$.

APPENDIX B

Fourier Poisson Equation Solver

The solution of the Poisson equation in **step 4** of Section 2.1.2 is performed using the solver based on fast Fourier transforms (FFT) presented in [5]. The solver is direct and more efficient than the Gaussian method. The two different versions of the solvers used in this work will be worked through in the following order: 2D problem with Neumann boundary conditions followed by 2D problem with Dirichlet boundary conditions.

B.1 2D Neumann Problem

Following the general algorithm laid out in Section 2.1.2, for a 2D computational domain Ω the first step is to incorporate the boundary conditions $\mathbf{b} \cdot \hat{\mathbf{n}}$ on $\partial\Omega$ into $\nabla \cdot \mathbf{b}$, see Figure B.1 for an illustration as well as the definition of the boundary names. On the respective boundaries the boundary conditions are

$$\begin{aligned}(\nabla P \cdot \hat{\mathbf{n}})_{0,j} &= (b_x)_{0,j} \\(\nabla P \cdot \hat{\mathbf{n}})_{M,j} &= (b_x)_{M,j} \\(\nabla P \cdot \hat{\mathbf{n}})_{i,0} &= (b_y)_{i,0} \\(\nabla P \cdot \hat{\mathbf{n}})_{i,N} &= (b_y)_{i,N}\end{aligned}\tag{B.1}$$

where b_x is the x -component of the discrete form of the \mathbf{b} and b_y is its y -component. Using the second-order finite difference scheme (A.5) in the center of Ω , the discretized

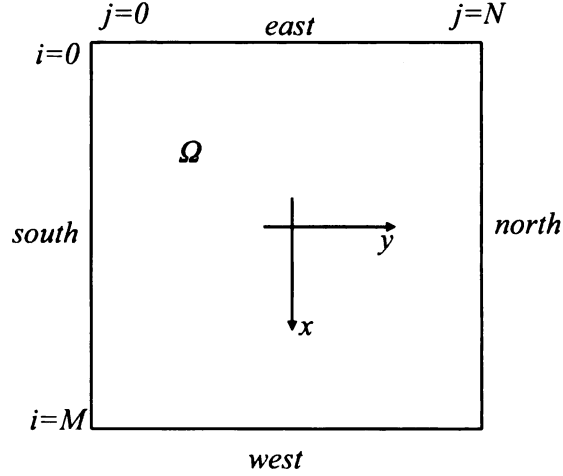


Figure B.1. A schematic illustrating the computational domain Ω and defining the names of the boundaries and indices used in the direct solver of the Poisson equation in two-dimensions.

version of $\nabla^2 P$ is

$$\frac{P_{(i+1),j} - 2P_{i,j} + P_{(i-1),j}}{(\Delta x)^2} + \frac{P_{i,(j+1)} - 2P_{i,j} + P_{i,(j-1)}}{(\Delta y)^2} = (\nabla \cdot \mathbf{b})_{i,j} = g_{i,j} \quad (\text{B.2})$$

By using the same discretization on the *east* boundary then for points $i = 0$ and $j = 1, 2, \dots, (N - 1)$

$$\frac{P_{1,j} - 2P_{0,j} + P_{-1,j}}{(\Delta x)^2} + \frac{P_{0,(j+1)} - 2P_{0,j} + P_{0,(j-1)}}{(\Delta y)^2} = (\nabla \cdot \mathbf{b})_{0,j} \quad (\text{B.3})$$

However, the point $P_{-1,j}$ does not exist in this computational domain. To eliminate this point from (B.3), the Neumann boundary condition are applied as prescribed in (B.1) discretized using (A.4)

$$\frac{P_{1,j} - P_{-1,j}}{(2\Delta x)} = (b_x)_{0,j} \quad (\text{B.4})$$

Substituting (B.4) into (B.3) yields the expression

$$\frac{2P_{1,j} - 2P_{0,j}}{(\Delta x)^2} + \frac{P_{0,(j+1)} - 2P_{0,j} + P_{0,(j-1)}}{(\Delta y)^2} = (\nabla \cdot \mathbf{b})_{0,j} + \frac{2}{\Delta x} (b_x)_{0,j} = g_{0,j} \quad (\text{B.5})$$

Similarly for the *west* boundary for points $i = M$ and $j = 1, 2, \dots, (N - 1)$

$$\begin{aligned} \frac{-2P_{M,j} + 2P_{(M-1),j}}{(\Delta x)^2} + \frac{P_{M,(j+1)} - 2P_{M,j} + P_{M,(j-1)}}{(\Delta y)^2} \\ = (\nabla \cdot \mathbf{b})_{M,j} - \frac{2}{\Delta x} (b_x)_{M,j} = g_{M,j} \end{aligned} \quad (\text{B.6})$$

the *south* boundary for points $i = 1, 2, \dots, (M - 1)$ and $j = 0$

$$\frac{P_{(i+1),0} - 2P_{i,0} + P_{(i-1),0}}{(\Delta x)^2} + \frac{2P_{i,1} - 2P_{i,0}}{(\Delta y)^2} = (\nabla \cdot \mathbf{b})_{i,0} + \frac{2}{\Delta y} (b_y)_{i,0} = g_{i,0} \quad (\text{B.7})$$

and the *north* boundary for points $i = 1, 2, \dots, (M - 1)$ and $j = N$

$$\begin{aligned} \frac{P_{(i+1),N} - 2P_{i,N} + P_{(i-1),N}}{(\Delta x)^2} + \frac{-2P_{i,N} + 2P_{i,(N-1)}}{(\Delta y)^2} \\ = (\nabla \cdot \mathbf{b})_{i,N} - \frac{2}{\Delta y} (b_y)_{i,N} = g_{i,N} \end{aligned} \quad (\text{B.8})$$

In the corners, boundary conditions apply in both directions, but the same method is used to incorporate the boundary conditions as on the sides of the domain. The *southeast* corner ($i = j = 0$) of Ω has contributions from the *south* and the *east* boundary conditions

$$\begin{aligned} \frac{2P_{1,0} - 2P_{0,0}}{(\Delta x)^2} + \frac{2P_{0,1} - 2P_{0,0}}{(\Delta y)^2} \\ = (\nabla \cdot \mathbf{b})_{0,0} + \frac{2}{\Delta x} (b_x)_{0,0} + \frac{2}{\Delta y} (b_y)_{0,0} = g_{0,0} \end{aligned} \quad (\text{B.9})$$

The remaining corners proceed in the same fashion. At $i = 0$ and $j = N$

$$\begin{aligned} \frac{2P_{1,N} - 2P_{0,N}}{(\Delta x)^2} + \frac{-2P_{0,N} + 2P_{0,(N-1)}}{(\Delta y)^2} \\ = (\nabla \cdot \mathbf{b})_{0,N} + \frac{2}{\Delta x} (b_x)_{0,N} - \frac{2}{\Delta y} (b_y)_{0,N} = g_{0,N}. \end{aligned} \quad (\text{B.10})$$

At $i = M$ and $j = 0$

$$\begin{aligned} \frac{-2P_{M,0} + 2P_{(M-1),0}}{(\Delta x)^2} + \frac{2P_{M,1} - 2P_{M,0}}{(\Delta y)^2} \\ = (\nabla \cdot \mathbf{b})_{M,0} - \frac{2}{\Delta x} (b_x)_{M,0} + \frac{2}{\Delta y} (b_y)_{M,0} = g_{M,0} \end{aligned} \quad (\text{B.11})$$

At $i = M$ and $j = N$

$$\begin{aligned} & \frac{-2P_{M,N} + 2P_{(M-1),N}}{(\Delta x)^2} + \frac{-2P_{M,N} + 2P_{M,(N-1)}}{(\Delta y)^2} \\ & = (\nabla \cdot \mathbf{b})_{M,N} - \frac{2}{\Delta x} (b_x)_{M,N} - \frac{2}{\Delta y} (b_y)_{M,N} = g_{M,N} \end{aligned} \quad (\text{B.12})$$

The next step in the solver is to use a FFT to decouple (B.5). This requires a cosine transform of the form

$$\hat{g}_{k,j} = \frac{2}{M} \sum_{i=0}^M {}'' g_{i,j} \cos ik \frac{\pi}{M} \quad (\text{B.13})$$

where the $''$ indicates that the first and last terms are multiplied by one half. The inverse of (B.13) is

$$g_{i,j} = \sum_{k=0}^M {}'' \hat{g}_{k,j} \cos ik \frac{\pi}{M} \quad (\text{B.14})$$

The transform of (B.14) can also be applied to the discretized pressure field

$$P_{i,j} = \sum_{k=0}^M {}'' \hat{P}_{k,j} \cos ik \frac{\pi}{M} \quad (\text{B.15})$$

Substituting (B.13) and (B.15) into (B.2) yields

$$\begin{aligned} & \frac{1}{(\Delta x)^2} \sum_{k=0}^M {}'' \hat{P}_{k,j} \left[\cos(i+1)k \frac{\pi}{M} - 2 \cos ik \frac{\pi}{M} + \cos(i-1)k \frac{\pi}{M} \right] + \\ & \sum_{k=0}^M {}'' \left(\frac{\hat{P}_{i,(j+1)} - 2\hat{P}_{k,j} + \hat{P}_{k,(j-1)}}{(\Delta y)^2} \right) \cos ik \frac{\pi}{M} = \\ & \sum_{k=0}^M {}'' \hat{g}_{k,j} \cos ik \frac{\pi}{M} \end{aligned} \quad (\text{B.16})$$

The first term on the RHS of (B.16) can be simplified using trigonometric identities $\cos(A+B) = \cos A \cos B - \sin A \sin B$ and $2 \sin^2 A = 1 - \cos 2A$, to

$$\cos(i+1)k \frac{\pi}{M} - 2 \cos ik \frac{\pi}{M} + \cos(i-1)k \frac{\pi}{M} = -4 \sin^2 k \frac{\pi}{2M} \cos ik \frac{\pi}{M} \quad (\text{B.17})$$

Substituting (B.17) into (B.16) and combining the sums on the LHS yields

$$\begin{aligned} \frac{1}{(\Delta y)^2} \sum_{k=0}^M \text{"} \left[\hat{P}_{k,(j+1)} - \left(2 + 4 \frac{\Delta y^2}{\Delta x^2} \sin^2 k \frac{\pi}{2M} \right) \hat{P}_{k,j} + \hat{P}_{k,(j-1)} \right] \cos ik \frac{\pi}{M} \\ = \sum_{k=0}^M \text{"} \hat{g}_{k,j} \cos ik \frac{\pi}{M} \end{aligned} \quad (\text{B.18})$$

Now apply the orthogonality of the basis function $\cos ik \frac{\pi}{M}$ to yield the tridiagonal system

$$\hat{P}_{k,(j+1)} - \left(2 + 4\chi^2 \sin^2 k \frac{\pi}{2M} \right) \hat{P}_{k,j} + \hat{P}_{k,(j-1)} = \Delta y^2 \hat{g}_{k,j} \quad (\text{B.19})$$

where $\chi = \Delta y / \Delta x$. On the *south* ($j = 0$) and *north* ($j = N$) boundaries (B.13) and (B.15) to (B.7) and (B.8) respectively are applied yielding

$$\begin{aligned} \frac{1}{(\Delta x)^2} \sum_{k=0}^M \text{"} \hat{P}_{k,0} \left[\cos(i+1)k \frac{\pi}{M} - 2 \cos ik \frac{\pi}{M} + \cos(i-1)k \frac{\pi}{M} \right] \\ + 2 \sum_{k=0}^M \text{"} \left(\frac{\hat{P}_{k,1} - \hat{P}_{k,0}}{\Delta y^2} \right) \cos ik \frac{\pi}{M} \\ = \sum_{k=0}^M \text{"} \hat{g}_{k,0} \cos ik \frac{\pi}{M} \end{aligned} \quad (\text{B.20})$$

and

$$\begin{aligned} \frac{1}{(\Delta x)^2} \sum_{k=0}^M \text{"} \hat{P}_{k,N} \left[\cos(i+1)k \frac{\pi}{M} - 2 \cos ik \frac{\pi}{M} + \cos(i-1)k \frac{\pi}{M} \right] \\ + 2 \sum_{k=0}^M \text{"} \left(\frac{-\hat{P}_{k,N} + \hat{P}_{k,(N-1)}}{\Delta y^2} \right) \cos ik \frac{\pi}{M} \\ = \sum_{k=0}^M \text{"} \hat{g}_{k,N} \cos ik \frac{\pi}{M} \end{aligned} \quad (\text{B.21})$$

Following the same simplification as for (B.19) the boundaries become

$$2\hat{P}_{k,1} - \left(2 + 4\chi^2 \sin^2 k \frac{\pi}{2M} \right) \hat{P}_{k,0} = \Delta y^2 \hat{g}_{k,0} \quad (\text{B.22})$$

for $j = 0$ and

$$-\left(2 + 4\chi^2 \sin^2 k \frac{\pi}{2M} \right) \hat{P}_{k,N} + 2\hat{P}_{k,(N-1)} = \Delta y^2 \hat{g}_{k,N} \quad (\text{B.23})$$

for $j = N$. The result of the transform is $(N + 1)$ tridiagonal systems of $(M + 1)$ equations which can be solved in a variety of standard ways. For the problem with Neumann boundary conditions, however, an additional step is required before the system can be solved.

In the case of the Neumann problem, a least-squares solution to the Poisson equation is sought. To complete the solution the problem the discrete form of Green's theorem is applied to this system

$$\sum_{i=0}^M (b_{y(i,N)} - b_{y(i,0)}) + \sum_{j=0}^N (b_{x(M,j)} - b_{x(0,j)}) = \sum_{i=0}^M \sum_{j=0}^N g_{i,j} \quad (\text{B.24})$$

Noisy velocity data and embedding mean that this system may not satisfy (B.24) initially and, therefore, that a solution does not exist. The RHS of (B.24) is perturbed slightly so that the resulting new system $\tilde{g}_{i,j}$ does obey Green's theorem. The solution to this system will be a least-squares solution to the original system $g_{i,j}$ if the perturbation is small compared to $g_{i,j}$. The perturbed system is defined as

$$\tilde{g}_{i,j} = g_{i,j} - \frac{\sum_{i=0}^M \sum_{j=0}^N c_i c_j g_{i,j}}{\sum_{i=0}^M \sum_{j=0}^N c_i c_j} \quad (\text{B.25})$$

Table B.1. The weights for the perturbation required to solve the 2D Neumann Poisson equation.

i			
	0	$1, 2, \dots, M - 1$	M
c_i	0.5	1	0.5
j			
	0	$1, 2, \dots, N - 1$	N
c_j	0.5	1	0.5

where c_i and c_j are weights whose value depends on i, j , see Table B.1. The Fourier coefficients are solved for using the $(M + 1)$ tridiagonal systems of $(N + 1)$ equations defined in (B.19), (B.22), (B.23) and $\tilde{g}_{i,j}$ yielding $\hat{P}_{i,j}$. As mentioned before one of

the tridiagonal systems will be singular. The output of this system can be set to an arbitrary value, in this work it is set to zero. The final step is to transform back into physical space using (B.15) to obtain $P_{i,j}$.

B.2 2D Dirichlet Problem

The solver for the 2D Dirichlet problem starts with the same discrete version of $\nabla^2 P$ as the Neumann problem, but as the boundary conditions are different, so is their incorporation. For this problem (B.2) is the same, but the boundary conditions are

$$\begin{aligned} P_{0,j} &= (p_{east})_j \\ P_{M,j} &= (p_{west})_j \\ P_{i,N} &= (p_{north})_i \\ P_{i,0} &= (p_{south})_i \end{aligned} \quad (\text{B.26})$$

where p_{east} , p_{west} , p_{north} and p_{south} are discrete functions that define the value of $P_{i,j}$ on their respective boundaries. At $i = 1$ and $j = 1, 2, \dots, (N - 2)$, (B.2) becomes

$$\frac{P_{2,j} - 2P_{1,j} + P_{0,j}}{(\Delta x)^2} + \frac{P_{1,j+1} - 2P_{1,j} + P_{1,(j-1)}}{(\Delta y)^2} = (\nabla \cdot \mathbf{b})_{1,j} \quad (\text{B.27})$$

Applying the appropriate boundary condition from (B.26) and rearranging

$$\frac{P_{2,j} - 2P_{1,j}}{(\Delta x)^2} + \frac{P_{1,(j+1)} - 2P_{1,j} + P_{1,(j-1)}}{(\Delta y)^2} = (\nabla \cdot \mathbf{b})_{1,j} - \frac{1}{(\Delta x)^2} (p_{east})_j = g_{1,j} \quad (\text{B.28})$$

The other boundaries follow in the same manner. For $i = (M - 1)$ and $j = 1, 2, \dots, (N - 2)$

$$\begin{aligned} \frac{-2P_{(M-1),j} + P_{(M-2),j}}{(\Delta x)^2} + \frac{P_{(M-1),j+1} - 2P_{(M-1),j} + P_{(M-1),(j-1)}}{(\Delta y)^2} \\ = (\nabla \cdot \mathbf{b})_{(M-1),j} - \frac{1}{(\Delta x)^2} (p_{west})_j = g_{(M-1),j} \end{aligned} \quad (\text{B.29})$$

For $i = 1, 2, \dots, (M - 2)$ and $j = 1$

$$\begin{aligned} \frac{P_{(i+1),1} - 2P_{i,1} + P_{(i-1),1}}{(\Delta x)^2} + \frac{P_{i,2} - 2P_{i,1}}{(\Delta y)^2} \\ = (\nabla \cdot \mathbf{b})_{i,1} - \frac{1}{(\Delta y)^2} (p_{north})_i = g_{i,1} \end{aligned} \quad (\text{B.30})$$

For $i = 1, 2, \dots, (M - 2)$ and $j = (N - 1)$

$$\begin{aligned} & \frac{P_{(i+1),(N-1)} - 2P_{i,(N-1)} + P_{(i-1),(N-1)}}{(\Delta x)^2} + \frac{-2P_{i,(N-1)} + P_{i,(N-2)}}{(\Delta y)^2} \\ & = (\nabla \cdot \mathbf{b})_{i,(N-1)} - \frac{1}{(\Delta y)^2} (p_{south})_i = g_{i,(N-1)} \end{aligned} \quad (\text{B.31})$$

The corners are treated with two boundary conditions. For $i = 1$ and $j = 1$

$$\begin{aligned} & \frac{P_{2,1} - 2P_{1,1}}{(\Delta x)^2} + \frac{P_{1,2} - 2P_{1,1}}{(\Delta y)^2} \\ & = (\nabla \cdot \mathbf{b})_{1,1} - \frac{1}{(\Delta x)^2} (p_{east})_1 - \frac{1}{(\Delta y)^2} (p_{south})_1 = g_{1,1} \end{aligned} \quad (\text{B.32})$$

For $i = 1$ and $j = (N - 1)$

$$\begin{aligned} & \frac{P_{2,(N-1)} - 2P_{1,(N-1)}}{(\Delta x)^2} + \frac{-2P_{1,(N-1)} + P_{1,(N-2)}}{(\Delta y)^2} \\ & = (\nabla \cdot \mathbf{b})_{1,(N-1)} - \frac{1}{(\Delta x)^2} (p_{west})_N - \frac{1}{(\Delta y)^2} (p_{south})_1 = g_{1,(N-1)} \end{aligned} \quad (\text{B.33})$$

For $i = (M - 1)$ and $j = 1$

$$\begin{aligned} & \frac{-2P_{(M-1),j} + P_{(M-2),j}}{(\Delta x)^2} + \frac{P_{(M-1),2} - 2P_{(M-1),1}}{(\Delta y)^2} \\ & = (\nabla \cdot \mathbf{b})_{(M-1),1} - \frac{1}{(\Delta x)^2} (p_{east})_1 - \frac{1}{(\Delta y)^2} (p_{north})_M = g_{(M-1),1} \end{aligned} \quad (\text{B.34})$$

For $i = (M - 1)$ and $j = (N - 1)$

$$\begin{aligned} & \frac{-2P_{(M-1),(N-1)} + P_{(M-2),(N-1)}}{(\Delta x)^2} + \frac{-2P_{(M-1),(N-1)} + P_{(M-1),(N-2)}}{(\Delta y)^2} \\ & = (\nabla \cdot \mathbf{b})_{(M-1),(N-1)} - \frac{1}{(\Delta x)^2} (p_{west})_N - \frac{1}{(\Delta y)^2} (p_{north})_M = g_{(M-1),(N-1)} \end{aligned} \quad (\text{B.35})$$

A problem with Dirichlet boundary conditions is decoupled with a sine FFT. The forward transform for $g_{i,j}$ is

$$\hat{g}_{k,j} = \frac{2}{M} \sum_{i=1}^{(M-1)} g_{i,j} \sin ik \frac{\pi}{M} \quad (\text{B.36})$$

The inverse FFT for g is

$$g_{i,j} = \sum_{k=1}^{M-1} \hat{g}_{i,j} \sin ik \frac{\pi}{M} \quad (\text{B.37})$$

Similarly, the inverse FFT for P is

$$P_{i,j} = \sum_{k=1}^{(M-1)} \hat{P}_{i,j} \sin ik \frac{\pi}{M} \quad (\text{B.38})$$

Following the procedure used to derive the 2D solver with Neumann boundary conditions in B.1, the next step is to substitute (B.36) and (B.38) into (B.2). This substitution yields

$$\begin{aligned} \frac{1}{(\Delta x)^2} \sum_{k=1}^{(M-1)} \hat{P}_{k,j} \left[\sin(i+1)k \frac{\pi}{M} - 2 \sin ik \frac{\pi}{M} + \sin(i-1)k \frac{\pi}{M} \right] + \\ \sum_{k=1}^{(M-1)} \left(\frac{\hat{P}_{k,(j+1)} - 2\hat{P}_{k,j} + \hat{P}_{k,(j-1)}}{(\Delta y)^2} \right) \sin ik \frac{\pi}{M} = \\ \sum_{k=1}^{(M-1)} \hat{g}_{k,j} \sin ki \frac{\pi}{M} \end{aligned} \quad (\text{B.39})$$

The term in the square brackets on the right hand side can be simplified using the identities $\sin(A+B) = \sin A \cos B + \sin B \cos A$ and $2 \sin^2 A = 1 - \cos 2A$

$$\left[\sin(i+1)k \frac{\pi}{M} - 2 \sin ik \frac{\pi}{M} + \sin(i-1)k \frac{\pi}{M} \right] = -4 \sin^2 k \frac{\pi}{2M} \sin ik \frac{\pi}{M} \quad (\text{B.40})$$

Notice that (B.40) has the same form as (B.17), but was derived from a sine transform rather than a cosine transform.

Following the same steps of combining the summations and applying the orthogonality of the basis function $\sin ik \frac{\pi}{M}$ as were used in the Neumann problem, the coefficients of (B.39) are set equal yielding

$$\hat{P}_{k,(j+1)} - \left(2 + 4\chi^2 \sin^2 k \frac{\pi}{2M} \sin ik \frac{\pi}{M} \right) \hat{P}_{k,j} + \hat{P}_{k,(j-1)} = (\Delta y)^2 \hat{g}_{k,j} \quad (\text{B.41})$$

where χ has the same definition as in the Neumann problem. For $j = 1$ and $j = (N-1)$ the coefficients are

$$\hat{P}_{k,2} - \left(2 + 4\chi^2 \sin^2 k \frac{\pi}{2M} \sin ik \frac{\pi}{M} \right) \hat{P}_{k,1} = (\Delta y)^2 \hat{g}_{k,1} \quad (\text{B.42})$$

and

$$-\left(2 + 4\chi^2 \sin^2 k \frac{\pi}{2M} \sin ik \frac{\pi}{M}\right) \hat{P}_{k,(N-1)} + \hat{P}_{k,(N-2)} = (\Delta y)^2 \hat{g}_{k,(N-1)} \quad (\text{B.43})$$

respectively. This group of $(M - 1)$ tridiagonal systems of $(N - 1)$ equations can be solved for $\hat{P}_{k,j}$ using any one of the standard techniques. The solution $P_{i,j}$ is obtained from $\hat{P}_{k,j}$ using the inverse transform defined in (B.38).

APPENDIX C

Mathematical Phantom

C.1 Couette Flow Between Rotating Cylinders

Couette flow is one of the few analytical solutions to the NSE. The derivation of the velocity and pressure fields for Couette flow between rotating cylinders begins with (2.3) in polar coordinates (r, θ) ignoring the axial direction

$$\begin{aligned} \rho \left(\frac{\partial v_r}{\partial t} + v_r \frac{\partial v_r}{\partial r} + \frac{v_\theta}{r} \frac{\partial v_r}{\partial \theta} - \frac{v_\theta^2}{r} \right) &= -\frac{\partial P}{\partial r} \\ +\mu \left(\frac{\partial^2 v_r}{\partial r^2} + \frac{1}{r} \frac{\partial v_r}{\partial r} + \frac{1}{r^2} \frac{\partial^2 v_r}{\partial \theta^2} - \frac{v_r}{r^2} - \frac{2}{r^2} \frac{\partial v_\theta}{\partial \theta} \right) & \end{aligned} \quad (\text{C.1})$$

$$\begin{aligned} \rho \left(\frac{\partial v_\theta}{\partial t} + v_r \frac{\partial v_\theta}{\partial r} + \frac{v_\theta}{r} \frac{\partial v_\theta}{\partial \theta} - \frac{v_r v_\theta}{r} \right) &= -\frac{1}{r} \frac{\partial P}{\partial \theta} \\ +\mu \left(\frac{\partial^2 v_\theta}{\partial r^2} + \frac{1}{r} \frac{\partial v_\theta}{\partial r} + \frac{1}{r^2} \frac{\partial^2 v_\theta}{\partial \theta^2} - \frac{v_\theta}{r^2} + \frac{2}{r^2} \frac{\partial v_\theta}{\partial \theta} \right) & \end{aligned} \quad (\text{C.2})$$

where v_r is the radial component of the velocity and v_θ is the azimuthal component. Now assume that the flow is steady ($\frac{\partial}{\partial t} = 0$), axisymmetric ($\frac{\partial}{\partial \theta} = 0$) and that the flow in the radial direction is negligible ($v_r \approx 0$), then (C.1) and (C.2) simplify to

$$\rho \left(\frac{v_\theta^2}{r} \right) = -\frac{dP}{dr} \quad (\text{C.3})$$

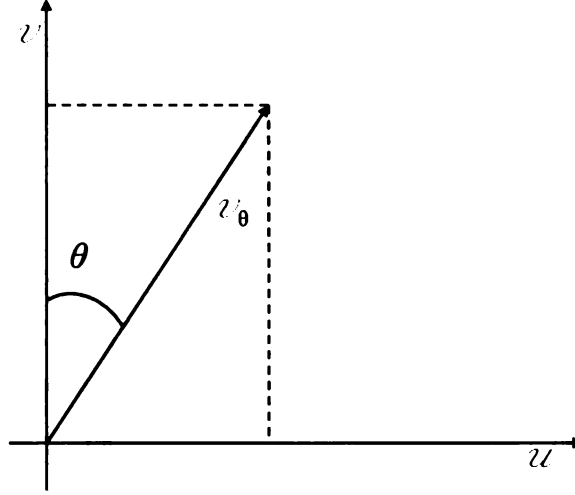


Figure C.1. A schematic illustrating the components of v_θ for the case where $v_r = 0$ in the Cartesian coordinate system

and

$$0 = \mu \left(\frac{\partial^2 v_\theta}{\partial r^2} + \frac{1}{r} \frac{\partial v_\theta}{\partial r} + \frac{v_\theta}{r^2} \right) \quad (\text{C.4})$$

respectively. Both the P and the v_θ are now functions of r only. Integrating (C.4) twice to solve for v_θ and applying the no slip boundary conditions on the walls of both cylinders ($v_\theta(r_1) = r_1\omega_1$ and $v_\theta(r_2) = r_2\omega_2$) yields

$$v_\theta(r) = \frac{\omega_2 r_2^2 - \omega_1 r_1^2}{r_2^2 - r_1^2} \frac{1}{r} + \frac{r_1^2 r_2^2 (\omega_1 - \omega_2)}{r_2^2 - r_1^2} r \quad (\text{C.5})$$

and leads to the definitions of A and B used in Section 2.3.1. The components of v_θ in the Cartesian coordinate system are found by geometry (see Figure C.1)

$$\begin{cases} u(r, \theta) = v_\theta \sin \theta \\ v(r, \theta) = v_\theta \cos \theta \end{cases} \quad (\text{C.6})$$

The pressure field is found by substituting (C.5) into (C.3) and integrating yielding

$$P(r) = \rho \left[\frac{\omega_2 r_2^2 - \omega_1 r_1^2}{r_2^2 - r_1^2} \frac{r^2}{2} + 2 \frac{\omega_2 r_2^2 - \omega_1 r_1^2}{r_2^2 - r_1^2} \frac{r_1^2 r_2^2 (\omega_1 - \omega_2)}{r_2^2 - r_1^2} \ln r - \left(\frac{r_1^2 r_2^2 (\omega_1 - \omega_2)}{r_2^2 - r_1^2} \right)^2 \frac{1}{2r^2} + C \right] \quad (\text{C.7})$$

C.2 Poiseuille Channel Flow

Pressure driven flow in a channel with stationary walls, also known as Poiseuille flow, is a second simple analytical solution to the NSE. The derivation of the velocity field and pressure field begin with (2.3) in Cartesian coordinates. It is assumed that the flow is steady, parallel to the channel walls, fully developed, and has no out-of-plane velocity component. The NSE simplify to

$$0 = -\frac{\partial P}{\partial x} + \mu \left(\frac{\partial^2 u}{\partial y^2} \right) \quad (\text{C.8})$$

where u is the component of the velocity in the x -direction. By rearranging (C.8)

$$\frac{1}{\mu} \frac{\partial P}{\partial x} = \left(\frac{\partial^2 u}{\partial y^2} \right) \quad (\text{C.9})$$

where the LHS is in terms of x and the RHS is in terms of y only. The RHS of (C.9) can be set equal to a constant C

$$C = \frac{d^2 u}{dy^2} \quad (\text{C.10})$$

solving for u knowing that the velocity is zero at the wall ($u = 0$ at $y = 0$ and $y = h$) yields

$$u(y) = \frac{C}{2} (y^2 - hy) \quad (\text{C.11})$$

The constant C in (C.11) is equal to the pressure gradient in the x -direction divided by the dynamic viscosity. To relate C to a physiological value, it is desirable to put it in terms of flow rate per unit depth. The flow rate for these conditions, Q_c , is found by

$$Q_c = \int_0^h u(y) dy \quad (\text{C.12})$$

Substituting (C.11), integrating and solving (C.12) for C yields

$$C = -\frac{12Q_c}{h^3} = \frac{1}{\mu} \frac{dP}{dx} \quad (\text{C.13})$$

The analytical velocity field is now

$$u(y) = \frac{-12Q_c\mu}{h^3} (y^2 - hy) \quad (\text{C.14})$$

The analytical pressure field is found by integrating (C.13) w.r.t. x

$$P(x) = -\frac{12Q_c\mu}{h^3} (x - x_o) \quad (\text{C.15})$$

where x_o is an arbitrary datum.

APPENDIX D

Experimental Parameters

The experiments determining the robustness of the PPE solution method to resolution, level of embedding and location of $\Omega_{\mathcal{F}}$ in Ω used a set of parameters in the Couette flow mathematical phantom that were not intended to match physiological conditions, see Table D.1. Instead it was intended to be a purely mathematical system. As such, the parameters were chosen for convenience. Using the values from Table D.1 the Re_C of this flow is 2.10×10^6 which is far beyond the transition to turbulent flow in this system. Therefore, the tests performed using this set of parameters serve as a ‘proof of concept’ for the method.

In the second set of noise experiments an attempt was made to have a more realistically scaled velocity field. This was done by matching Re_C and Re_a as defined in Section 2.3.3 as closely as possible. Using the conditions from the calculation of the Wo from Section 2.1.1 ($\rho = 1040\text{kg m}^{-3}$, $\mu = 0.004\text{Ns}$, $D_a = 0.01\text{m}$) and assuming an average velocity of $\bar{U}_a = 0.1\text{ m s}^{-1}$, $Re_A \approx 260$. The parameters in Table D.2 closely approximate these viscous conditions leading to $Re_C = 235$.

For the set of Poiseuille flow of experiments, similar values to those chosen for the second set of Couette flow experiments. The volumetric flow rate Q_c was chosen to approximate the average flow rate in the carotid artery and normalized by the average

radius of the artery to yield the desired units and velocity scales. This is based on the average velocity and approximate cross-sectional area. The parameters in Table D.3 were used to generate the analytical velocity field and relative pressure field.

Table D.1. Parameters used in the Couette flow mathematical phantom in the resolution, embedding and initial noise experiments.

x_{\min} (m)	-1
x_{\max} (m)	1
y_{\min} (m)	-1
y_{\max} (m)	1
r_1 (m)	0.25
r_2 (m)	0.79
ω_1 (rad/s)	π
ω_2 (rad/s)	2π
μ (N s m ⁻²)	0.656×10^{-3}
ρ (kg m ⁻³)	992.2
η (-)	0.05

Table D.2. Parameters used in the Couette flow mathematical phantom noise experiments with more realistic viscous terms.

x_{\min} (m)	-6.2×10^{-3}
x_{\max} (m)	6.2×10^{-3}
y_{\min} (m)	-6.2×10^{-3}
y_{\max} (m)	6.2×10^{-3}
r_1 (m)	2×10^{-3}
r_2 (m)	5×10^{-3}
ω_1 (rad/s)	36π
ω_2 (rad/s)	18π
μ (N s m ⁻²)	4×10^{-3}
ρ (kg m ⁻³)	1040
η (-)	0.05

Table D.3. Parameters used in the Poiseuille flow mathematical phantom noise experiments.

x_{\min} (m)	-6.2×10^{-3}
x_{\max} (m)	6.2×10^{-3}
y_{\min} (m)	-6.2×10^{-3}
y_{\max} (m)	6.2×10^{-3}
h (m)	10^{-3}
Q_c (m ³ /s)	1.57×10^{-3}
μ (N s m ⁻²)	4×10^{-3}
ρ (kg m ⁻³)	1040
η (-)	0.05

APPENDIX E

Tabulated Experimental Results

This appendix contains the tabulated results from Sections 3.1 and 3.2. The tables are labeled with their corresponding figures.

Table E.1. The normalized relative RMS error, $\bar{\epsilon}$, results of the isotropic and anisotropic resolution tests (see Figures 3.1 and 3.2).

η	$\bar{\epsilon}$ (%)	χ_α	$\alpha = \eta_{sol} \bar{\epsilon}$ (%)	$\alpha = \eta_{sol} \bar{\epsilon}$ (%)
0.0007	0.0032	0.1250	0.0217	0.0217
0.0014	0.0028	0.2500	0.0246	0.0246
0.0056	0.0087	0.5000	0.0222	0.0222
0.0112	0.0243	1.0000	0.0183	0.0183
0.0223	0.0966	2.0000	0.0430	0.0430
0.0255	0.1278	4.0000	0.1485	0.1485
0.0298	0.1930	5.3333	0.1520	0.1520
0.0357	0.3249	6.4000	0.2139	0.2139
0.0446	0.3943	7.1111	0.2563	0.2563
0.0595	0.5899	8.0000	0.3650	0.3650
0.0893	1.8457	9.1429	0.5880	0.4227
		10.6667	0.6379	0.6379
		12.8000	1.2395	0.7797
		16.0000	2.6315	1.3225

Table E.2. The normalized relative RMS error, $\bar{\epsilon}$ (%), results of the embedding tests (see Figure 3.3).

Γ (%)	0.0000	8.6957	17.391	26.807	34.783	43.478	60.699	69.565
Center	1.4908	1.1014	1.0029	0.9595	0.9223	0.8923	0.8714	0.8575
Off Center	1.4320	1.0835	1.0024	0.9875	0.9833	0.9755	0.9639	0.9515
Corner	1.2316	1.0178	0.9584	0.9269	0.9187	0.9260	0.9412	0.9581
Γ (%)	78.261	86.957	95.652	104.35	113.04	121.74	130.44	139.13
Center	0.8487	0.8430	0.8390	0.8360	0.8339	0.8322	0.8308	0.8296
Off Center	0.9407	0.9329	0.9286	0.9275	0.9288	0.9323	0.9369	0.9423
Corner	0.9733	0.9851	0.9933	0.9983	1.007	1.0014	1.0009	0.9996
Γ (%)	147.83	156.52	165.22	173.91	182.61	191.30	200.00	208.70
Center	0.8286	0.8277	0.8268	0.8261	0.8255	0.8249	0.8243	0.8239
Off Center	0.9481	0.9536	0.9590	0.9640	0.9684	0.9723	0.9756	0.9784
Corner	0.9979	0.9960	0.9940	0.9920	0.9900	0.9882	0.9865	0.9849
Γ (%)	217.39	226.09	234.78	243.48	252.17	260.87	269.57	278.26
Center	0.8234	0.8229	0.8225	0.8222	0.8219	0.8916	0.8213	0.8211
Off Center	0.9808	0.9828	0.9844	0.9858	0.9869	0.9877	0.9885	0.9890
Corner	0.9834	0.9821	0.9808	0.9797	0.9786	0.9777	0.9768	0.9761

Table E.3. The filter parameters that yield optimal performance at SNR = 5. These are the parameters used in all future experiments with noisy velocity fields (see Figures 3.4 and 3.5).

	α'_1	α'_2	γ'_2	α'_3	γ'_3	α'_4	γ'_4
Parameter	0.1	0.01	0.53	0.01	0.1	0.0001	0.1

Table E.4. The average normalized relative RMS error and standard deviation, $\bar{\varepsilon} \pm \sigma$ (%), in the estimated relative pressure field, for the initial Couette flow parameters, a resolution of $\eta = 0.05$ on a 20×20 flow domain Ω_F and an embedding level $\Gamma = 25\%$, after applying the three filters proposed here (Median Filter, Filter 1, Filter 2) to the relative pressure field estimated with no filtering and three filters from the literature (PSDF [1], $(d/dx)^2$ [2], Visc. Diss. [3]) over the range of SNR tested (see Figure 3.6).

SNR	5	10	15
No Filter	23.6 ± 4.10	11.9 ± 1.88	8.09 ± 1.48
Median Filter	19.3 ± 1.81	12.1 ± 0.91	10.1 ± 0.52
Filter 1	14.3 ± 2.54	7.65 ± 1.52	5.0834 ± 1.06
Filter 2	5.30 ± 1.96	2.64 ± 1.28	2.29 ± 0.45
PSDF	22.4 ± 4.38	13.2 ± 1.63	11.1 ± 1.13
d/dx^2	10.5 ± 1.82	6.48 ± 0.71	4.23 ± 0.60
Visc. Diss.	7.56 ± 1.34	5.30 ± 0.73	5.14 ± 0.56
SNR	20	25	30
No Filter	5.89 ± 1.04	4.78 ± 0.81	3.98 ± 0.71
Median Filter	10.1 ± 0.40	10.2 ± 0.36	10.2 ± 0.34
Filter 1	3.63 ± 0.60	3.03 ± 0.61	2.55 ± 0.55
Filter 2	2.94 ± 0.23	1.95 ± 0.46	2.00 ± 0.26
PSDF	10.32 ± 0.70	9.85 ± 0.58	9.58 ± 0.46
d/dx^2	3.72 ± 0.52	3.16 ± 0.43	2.88 ± 0.35
Visc. Diss.	4.78 ± 0.51	4.55 ± 0.36	4.30 ± 0.49

Table E.5. The average performance factor F and standard deviation, $F \pm \sigma$, for all filters tested using the initial Couette flow experimental parameters, a resolution of $\eta = 0.05$ on a 20×20 flow domain Ω_F and an embedding level $\Gamma = 25\%$ across the range of SNR tested (see Figure 3.8).

SNR	5	10	15
Median Filter	0.95 ± 0.03	1.60 ± 0.05	2.22 ± 0.22
Filter 1	0.75 ± 0.04	0.72 ± 0.05	0.74 ± 0.06
Filter 2	0.18 ± 0.03	0.22 ± 0.04	0.20 ± 0.02
PSDF	0.98 ± 0.05	1.34 ± 0.07	1.82 ± 0.08
d/dx^2	0.56 ± 0.04	0.74 ± 0.05	0.80 ± 0.06
Visc. Diss.	0.46 ± 0.03	0.82 ± 0.07	1.34 ± 0.09
SNR	20	25	30
Median Filter	2.99 ± 0.14	3.79 ± 0.21	4.41 ± 0.34
Filter 1	0.68 ± 0.06	0.76 ± 0.06	0.69 ± 0.05
Filter 2	0.19 ± 0.03	0.23 ± 0.04	0.25 ± 0.02
PSDF	2.34 ± 0.15	2.91 ± 0.16	3.36 ± 0.19
d/dx^2	0.87 ± 0.02	0.99 ± 0.03	1.12 ± 0.06
Visc. Diss.	1.73 ± 0.16	2.01 ± 0.22	2.31 ± 0.16

Table E.6. The average normalized relative RMS error and standard deviation, $\bar{\varepsilon} \pm \sigma$ (%), in the estimated relative pressure field, for the second Couette flow parameters, a resolution of $\eta = 0.05$ on a 20×20 flow domain Ω_F and an embedding level $\Gamma = 25\%$, after applying the three filters proposed here (Median Filter, Filter 1, Filter 2) to the relative pressure field estimated with no filtering (see Figure 3.10).

SNR	5	10	15
No Filter	37.9 ± 8.57	18.4 ± 4.05	12.2 ± 2.66
Median Filter	21.9 ± 2.76	13.1 ± 1.49	9.99 ± 1.12
Filter 1	22.9 ± 3.48	10.6 ± 1.47	7.01 ± 1.24
Filter 2	5.85 ± 0.60	3.37 ± 0.97	3.08 ± 0.36
SNR	20	25	30
No Filter	9.11 ± 1.99	7.29 ± 1.58	6.08 ± 1.32
Median Filter	8.36 ± 0.85	7.35 ± 0.67	6.72 ± 0.54
Filter 1	5.97 ± 1.33	4.16 ± 0.69	4.06 ± 0.56
Filter 2	2.41 ± 0.51	2.05 ± 0.21	2.09 ± 0.16

Table E.7. The average normalized relative RMS error and standard deviation, $\bar{\varepsilon} \pm \sigma$ (%), in the estimated relative pressure field, for the Poiseuille flow parameters, a resolution of $\eta = 0.05$ on a 20×20 flow domain Ω_F and an embedding level $\Gamma = 25\%$, after applying the three filters proposed here (Median Filter, Filter 1, Filter 2) to the relative pressure field estimated with no filtering and two filters from the literature ($(d/dx)^2$ [2], Visc. Diss. [3]) over the range of SNR tested (see Figure 3.11).

SNR	5	10	15	20
No Filter	923.4 ± 78.2	456.1 ± 15.8	332.9 ± 16.3	239.9 ± 33.7
Median Filter	968.4 ± 51.4	576.7 ± 27.2	526.4 ± 25.6	488.1 ± 25.7
Filter 1	572.5 ± 61.1	234.1 ± 73.6	139.9 ± 9.27	145.7 ± 21.4
Filter 2	483.5 ± 25.8	217.1 ± 28.1	166.6 ± 18.1	113.3 ± 6.93
d/dx^2	157.5 ± 14.8	130.5 ± 5.81	120.9 ± 6.94	119.4 ± 19.0
Visc. Diss.	764.7 ± 22.9	742.3 ± 85.7	793.2 ± 58.6	727.1 ± 31.9

BIBLIOGRAPHY

- [1] S. M. Song, S. Napel, G. H. Glover, and N. J. Pelc. Noise reduction in three-dimensional phase contrast MR velocity measurements. *J. Magn. Reson. Imaging*, 3:587–596, 1993.
- [2] N. Fatouraee and A. A. Amini. Regularization of flow streamlines in multislice phase-contrast MR imaging. *IEEE Trans. Med. Imag.*, 22:699–709, 2003.
- [3] L. G. Raguin, A. K. Kodali, D. V. Rovas, and J. G. Georgiadis. An inverse problem for reduced-encoding MRI velocimetry in potential flow. *Conf. Proc. IEEE Engineering in Medicine and Biology Society*, 2:1100–3, 2004.
- [4] S. M. Song, R. M. Leahy, D. P. Boyd, B. H. Brundage, and S. Napel. Determining cardiac velocity fields and intraventricular pressure distribution from a sequence of ultrafast CT cardiac images. *IEEE Trans. Med. Imag.*, 13:386–397, 1994.
- [5] P. N. Swarztrauber. Fast Poisson solvers. In G. H. Goulb, editor, *Studies in Numerical Analysis*, volume 24, pages 319–70. Mathematical Association of America, Washington DC, 1984.
- [6] J. P. Mohr, L. R. Caplan, J. W. Melski, R. J. Goldstein, G. W. Duncan, J. P. Kistler, M. S. Pessin, and H. L. Bleich. The Harvard cooperative stroke registry: A prospective registry. *Neurology*, 28:754–762, 1978.
- [7] J. Bogousslavsky, G. Van Melle, and F. Regli. The Lausanne stroke registry: Analysis of 1000 consecutive patients with first stroke. *Stroke*, 19:445–453, 1988.
- [8] C. W. White, C. B. Wright, D. B. Doty, L. F. Hiratza, C. L. Eastham, D. G. Harrison, and M. L. Marcus. Does visual interpretation of the coronary arteriogram predict the physiologic importance of a coronary stenosis? *N. Engl. J. Med.*, 310:819–824, 1984.
- [9] W. Grossman. *Cardiac Catheterization, Angiography, and Intervention*, chapter Current Practice Standards, pages 9–10. Willimas & Wilkins, Baltimore, 5th edition, 1996.

- [10] T. Ebbers, L. Wigström, A. F. Bolger, B. Wranne, and M. Karlsson. Noninvasive measurement of time-varying three-dimensional relative pressure fields within the human heart. *J. Biomech. Eng.-T. ASME*, 124:288–293, 2002.
- [11] A. Nasiraei-Moghaddam, G. Behrens, N. Fatouraee, R. Agarwal, E. T. Choi, and A. A. Amini. Factors affecting the accuracy of pressure measurements in vascular stenosis from phase-contrast MRI. *Magn. Resonan. Med.*, 52:300–309, 2004.
- [12] G.-Z. Yang, P. J. Kilner, N. B. Wood, S. R. Underwood, and D. N. Firmin. Computation of flow pressure fields from magnetic resonance velocity mapping. *Magn. Resonan. Med.*, 36:520–526, 1996.
- [13] J. M. Tyszka, D. H. Laidlaw, J. W. Asa, and J. M. Silverman. Three-dimensional, time-resolved (4D) relative pressure mapping using magnetic resonance imaging. *J. Magn. Reson. Imaging*, 12:321–329, 2000.
- [14] D. P. Lum, K. M. Johnson, R. K. Paul, A. S. Turk, D. W. Consigny, J. R. Grinde, C. A. Mistretta, and T. M. Grist. Transstenotic pressure gradients: Measurement in swine – retrospectively ECG-gated 3D phase-contrast MR angiography versus endovascular pressure-sensing guidewires. *Radiology*, 245:751–760, 2007.
- [15] L. Hatle, A. Brubakk, A. Tromsdal, and B. Angelsen. Noninvasive assessment of pressure-drop in mitral-stenosis by Doppler ultrasound. *Br. Heart J.*, 40:131–140, 1978.
- [16] S. N. Urchuk and D. B. Plewes. MR measurement of time-dependent blood pressure variations. *J. Magn. Reson. Imaging*, 5:621–627, 1995.
- [17] S. N. Urchuk, S. E. Fremes, and D. B. Plewes. *In vivo* validation of MR pulse pressure measurement in an aortic flow model: Preliminary results. *Magn. Resonan. Med.*, 38:215–223, 1997.
- [18] T. Ebbers, L. Wigström, A. F. Bolger, J. Engvall, and M. Karlsson. Estimation of relative cardiovascular pressures using time-resolved three-dimensional phase contrast MRI. *Magn. Reson. Med.*, 45:872–879, 2001.
- [19] R. B. Thompson and E. R. McVeigh. Fast measurement of intracardiac pressure differences with 2D breath-hold phase-contrast MRI. *Magn. Reson. Med.*, 49:1056–1066, 2003.
- [20] J.-P. Tasu, E. Mousseaux, A. Delouche, C. Oddou, O. Jolivet, and J. Bittoun. Estimation of pressure gradients in pulsatile flow from magnetic resonance acceleration measurements. *Magn. Resonan. Med.*, 44:66–72, 2000.

- [21] F. Buyens, O. Jolivet, A. De Cesare, J. Bittoun, A. Herment, J.-P. Tasu, and E. Mousseaux. Calculation of left ventricle relative pressure distribution in MRI using acceleration data. *Magn. Resonan. Med.*, 53:877–884, 2005.
- [22] N. B. Wood. Aspects of fluid dynamics applied to the larger arteries. *J. Theor. Biol.*, 199:137–161, 1999.
- [23] F. P. Glor, J. J. M. Westenberg, J. Vierendeels, M. Danilouchkine, and P. Verdonck. Validation of the coupling of magnetic resonance imaging velocity measurements with computational fluid dynamics in a U bend. *International Society for Artificial Organs*, 26:622–635, 2002.
- [24] N. B. Wood, S. J. Weston, P. J. Kilner, A. D. Gosman, and D. N. Firmin. Combined MR imaging and CFD simulation of flow in the human descending aorta. *J. Magn. Reson. Imaging*, 13:699–713, 2001.
- [25] P. Yim, K. DeMarco, M. A. Castro, and J. Cebal. *Plaque Imaging: Pixel to Molecular Level*, chapter Characterization of Shear Stress on the Wall of the Carotid Artery Using Magnetic Resonance Imaging and Computational Fluid Dynamics, pages 412–442. IOS Press, 2005.
- [26] Q. Long, X. Y. Xu, B. Ariff, S. A. Thorn, A. D. Hughes, and A. V. Stanton. Reconstruction of blood flow patterns in a human carotid bifurcation: A combined CFD and MRI study. *J. Magn. Reson. Imaging*, 11:299–311, 2000.
- [27] J. R. Cebal, P. J. Yim, R. Löhner, O. Soto, and P. L. Choyke. Blood flow modeling in carotid arteries with computational fluid dynamics and MR imaging. *Acad. Radiol.*, 9:1286–1299, 2002.
- [28] P. Papathanasopoulou, S. Zhao, U. Köhler, M. B. Robertson, Q. Long, P. Hoskins, X. Y. Xu, and I. Marshall. MRI measurement of time-resolved wall shear stress vectors in a carotid bifurcation model, and comparison with CFD predictions. *J. Magn. Reson. Imaging*, 17:153–162, 2003.
- [29] I. Marshall, S. Zhao, P. Papathanasopoulou, P. Hoskins, and X. Y. Xu. MRI and CFD studies of pulsatile flow in healthy and stenosed carotid bifurcation models. *Journal of Biomechanics*, 37:679–687, 2004.
- [30] A. Leuprecht, S. Kozerke, P. Boesiger, and K. Perktold. Blood flow in the human ascending aorta: a combined MRI and CFD study. *Journal of Engineering Mathematics*, 47:387–404, 2003.
- [31] S. D. Shpilfoygel, R. A. Close, D. J. Valentino, and G. R. Duckwiler. X-ray videodensitometric methods for blood flow and velocity measurement: A critical review of literature. *Med. Phys.*, 27:2008–2023, 2000.

- [32] S. P. Huang, R. J. Decker, K. G. Goodrich, D. J. Parker, J. B. Muhlestein, D. D. Blatter, and D. L. Parker. Velocity measurement based on bolus tracking with the aid of three-dimensional reconstruction from digital subtraction angiography. *Med. Phys.*, 24:677–686, 1997.
- [33] N. Hangiandreou, J. Folts, W. Peppler, and C. Mistretta. Coronary blood flow measurement using an angiographic first pass distribution technique: A feasibility study. *Med. Phys.*, 18:947–954, 1991.
- [34] S. Molloy, Y. J. Qian, and A. Ersahin. Absolute volumetric blood flow measurements using dual-energy digital subtraction angiography. *Med. Phys.*, 20:85–91, 1993.
- [35] S. Molloy, G. Bednarz, J. Tang, Y. Zhou, and T. Mathur. Absolute volumetric coronary blood flow measurement with digital subtraction angiography. *International Journal of Cardiac Imaging*, 14:137–145, 1998.
- [36] S. E. Nissen, J. L. Elion, D. C. Booth, J. Evans, and A. N. DeMaria. Value and limitations of computer analysis of digital subtraction angiography in the assessment of coronary flow reserve. *Circulation*, 73:562–571, 1986.
- [37] P. Spiller, F. K. Schmiel, B. Politz, M. Block, U. Fermor, W. Hackbarth, J. Jehle, R. Korfer, and H. Pannek. Measurement of systolic and diastolic flow rates in the coronary artery system by x-ray densitometry. *Circulation*, 68:337–347, 1983.
- [38] R. W. Barnes. *Noninvasive Diagnostic Techniques in Vascular Disease*, chapter 4: Continuous-wave Doppler Ultrasound, pages 19–24. The C. V. Mosby Company, 1985.
- [39] K. W. Beach and D. E. Strandness. *Noninvasive Diagnostic Techniques in Vascular Disease*, chapter 5: Pulsed Doppler Ultrasound for Blood Velocity Measurements, pages 25–32. The C. V. Mosby Company, St. Louis, 1985.
- [40] K. Fusejima. Noninvasive measurement of coronary-artery blood-flow using combined two-dimensional and Doppler echocardiography. *J. AM. Coll. Cardiol*, 10:1024–1031, 1987.
- [41] H. Mast, J. P. Mohr, J. L. P. Thompson, A. Osipov, S. H. Trocio, S. Mayer, and W. L. Young. Transcranial Doppler ultrasonography in cerebral arteriovenous malformations: Diagnostic sensitivity and association of flow velocity with spontaneous hemorrhage and focal neurological deficit. *Stroke*, 26:1024–1027, 1995.
- [42] T. Hozumi, K. Yoshida, T. Aksaka, Y. Asami, Y. Ogata, T. Takagi, S. Kaji, T. Kawamoto, Y. Ueda, and S. Morioka. Noninvasive assessment of coronary

- flow velocity and coronary flow velocity reserve in the left anterior descending coronary artery by Doppler echocardiography: Comparison with invasive technique. *J. Am. Coll. Cardiol*, 32:1251–1259, 1998.
- [43] T. Hozumi, K. Yoshida, Y. Ogata, T. Akasaka, Y. Asami, T. Takagi, and S. Morioka. Noninvasive assessment of significant left anterior descending coronary artery stenosis by coronary flow velocity reserve with transthoracic color Doppler echocardiography. *Circulation*, 97:1557–1562, 1998.
- [44] G. N. Hounsfield. Computed medical imaging. *Med. Phys.*, 7:283–290, 1980.
- [45] L. Axel. Cerebral blood-flow determination by rapid-sequence computed tomography – A theoretical-analysis. *Radiology*, 137:679–686, 1980.
- [46] N. A. Mullani and K. L. Gould. First-pass measurements of regional blood flow with external devices. *J. Nucl. Med.*, 24:577–581, 1983.
- [47] W. Jaschke, R. G. Gould, P. A. Assimakopoulos, and M. J. Lipton. Flow measurements with a high-speed computed tomography scanner. *Med. Phys.*, 14:238–243, 1987.
- [48] P. F. Ludman, M. Darby, N. Tomlinson, P. A. Poole-Wilson, and S. Rees. Cardiac flow measurement by ultrafast CT - validation of continuous and pulsatile flow. *J. Comput. Assist. Tomogr.*, 16:795–803, 1992.
- [49] R. J. Herfkens, L. Axel, M. J. Lipton, S. Napel, W. Berninger, and R. Redington. Measurement of cardiac-output by computed transmission tomography. *Invest. Radiol.*, 17:550–553, 1982.
- [50] J. S. Garrett, P. Lanzer, W. Jaschke, E. Botvinick, R. Sievers, C. B. Higgins, and M. J. Lipton. Measurement of cardiac output by cine computed tomography. *Am. J. Cardiol.*, 56:657–661, 1985.
- [51] T. Kaminaga, H. Naito, M. Takamiya, and T. Nishimura. Quantitative evaluation of mitral regurgitation with ultrafast CT. *J. Comput. Assist. Tomogr.*, 18:239–242, 1994.
- [52] U. J. Schoepf, R. Bruening, H. Konschitzky, C. R. Becker, A. Knez, J. Weber, O. Muehling, P. Herzog, A. Huber, R. Haberl, and M. F. Reiser. Pulmonary embolism: Comprehensive diagnosis by using electron-beam CT for detection of emboli and assessment of pulmonary blood flow. *Radiology*, 217:693–700, 2000.
- [53] P. F. Ludman, A. J. Coats, P. A. Poole-Wilson, and R. S. Rees. Measurement accuracy of cardiac output in humans: indicator dilution technique vs geometric analysis by ultrafast computed tomography. *J. Am. Coll. Cardiol*, 21:1482–1489, 1993.

- [54] P. A. Doriot, P. A. Dorsaz, L. Dorsaz, and W. J. Rutishauser. Is the indicator dilution theory really the adequate base of many blood flow measurement techniques? *Med. Phys.*, 24:1889–1898, 1997.
- [55] A. H. Mahnken, M. Grasruck, B. Schmidt, R. W. Günther, and J. E. Wildberger. Flat panel computed tomography for non-invasive flow measurement: Initial results in *In Vitro* studies. *Eur Radiol*, 18:747–752, 2008.
- [56] S. M. Song and R. M. Leahy. Computation of 3-D velocity fields from 3-D cine CT images of a human heart. *IEEE Trans. Med. Imaging*, 10:295–306, 1991.
- [57] F. Bloch, W. W. Hansen, and M. Packard. Nuclear induction. *Phys. Rev.*, 69:127, 1946.
- [58] E. M. Purcell, H. C. Torrey, and R. V. Pound. Resonance absorption by nuclear magnetic moments in a solid. *Phys. Rev.*, 69:37–38, 1946.
- [59] P. C. Lauterbur. Image formation by induced local interactions: examples employing nuclear magnetic-resonance. *Nature*, 242:190–191, 1973.
- [60] P. Mansfield. Multi-planar image formation using NMR spin echoes. *J. Phys. C. Solid State Phys.*, 10:L55–L58, 1977.
- [61] Z. P. Liang and P. C. Lauterbur. *Principles of Magnetic Resonance Imaging: A Signal Processing Perspective*. IEEE Press, 2000.
- [62] C. J. Elkins and M. T. Alley. Magnetic resonance velocimetry: applications of magnetic resonance imaging in the measurement of fluid motion. *Exp. Fluids*, 43:823–858, 2007.
- [63] L. Axel and L. Dougherty. MR imaging of motion with spatial modulation of magnetization. *Radiology*, 171:841–845, 1989.
- [64] T. J. Mosher and M. B. Smith. A DANTE tagging sequence for the evaluation of translational sample motion. *Magn. Reson. Med.*, 15:334–339, 1990.
- [65] K. W. Moser, E. C. Kutter, J. G. Georgiadis, R. O. Buckius, H. D. Morris, and J. R. Torczynski. Velocity measurement of flow through a step stenosis using Magnetic Resonance Imaging. *Exp. Fluids*, 29:438–447, 2000.
- [66] K. W. Moser, J. G. Georgiadis, and R. O. Buckius. On the use of optical flow methods with spin-tagging magnetic resonance imaging. *Annals of Biomedical Engineering*, 29:9–17, 2001.

- [67] H. G. Bogren and M. H. Buonocore. 4D magnetic resonance velocity mapping of blood flow patterns in the aorta in young vs. elderly normal subjects. *J. Magn. Reson. Imaging*, 10:861–869, 1999.
- [68] M. Markl, F. P. Chan, M. T. Alley, K. L. Wedding, M. T. Draney, C. J. Elkins, D. W. Parker, R. Wicker, C. A. Taylor, R. J. Herfkens, and N. J. Pelc. Time-resolved three-dimensional phase-contrast MRI. *J. Magn. Reson. Imaging*, 17:499–506, 2003.
- [69] N. J. Pelc, M. A. Bernstein, A. Shimakawa, and G. H. Glover. Encoding strategies for three-direction phase-contrast MR imaging of flow. *J. Magn. Reson. Imaging*, 1:405–413, 1991.
- [70] C. Tang, D. D. Blatter, and D. L. Parker. Accuracy of phase-contrast flow measurements in the presence of partial-volume effects. *J. Magn. Reson. Imaging*, 3:377–385, 1993.
- [71] D. N. Firmin, G. L. Nayler, P. J. Kilner, and D. B. Longmore. The application of phase-shifts in NMR for flow measurement. *Magn. Reson. Med.*, 14:230–241, 1990.
- [72] N. J. Pelc, M. T. Alley, J. Listerud, and S. W. Atlas. *Magnetic Resonance Imaging of the Brain and Spine*, chapter Fundamentals of flow and hemodynamics, pages 101–126. Lippincott Williams & Wilkins, 2002.
- [73] C. A. Taylor and M. T. Draney. Experimental and computational methods in cardiovascular fluid mechanics. *Annu. Rev. Fluid Mech.*, 36:197–231, 2004.
- [74] M. F. Walker, S. P. Souza, and C. L. Dumoulin. Quantitative flow measurement in phase-contrast MR angiography. *J. Comput. Assist. Tomogr.*, 12:304–313, 1988.
- [75] D. Meier, S. Maier, and P. Bösiger. Quantitative flow measurement on phantoms and on blood vessels with MR. *Magn. Reson. Med.*, 5:25–34, 1988.
- [76] H. Zhang, S. S. Halliburton, J. R. Moore, O. P. Simonetti, P. R. Schvartzman, R. D. White, and G. P. Chatzimavroudis. Accurate quantification of steady and pulsatile flow with segmented k-space magnetic resonance velocimetry. *Exp. Fluids*, 33:458–463, 2002.
- [77] M. B. Robertson, U. Köhler, P. R. Hoskins, and I. Marshall. Quantitative analysis of PC MRI velocity maps: pulsatile flow in cylindrical vessels. *Magn. Reson. Imaging*, 19:685–695, 2001.

- [78] A. E. Ensley, A. Ramuzat, T. M. Healy, G. P. Chatzimavroudis, C. Lucas, S. Sharma, R. Pettigrew, and A. P. Yoganathan. Fluid mechanic assessment of the total cavopulmonary connection using magnetic resonance phase velocity mapping and digital particle image velocimetry. *Annals of Biomedical Engineering*, 28:1172–1183, 2000.
- [79] G. A. Varapasathan, P. A. Araoz, C. B. Higgins, and G. P. Reddy. Quantification of flow dynamics in congenital heart disease: Applications of velocity-encoded cine MR imaging. *Radiographics*, 22:895–905, 2002.
- [80] R. Botnar, G. Rappitsch, M. B. Scheidegger, D. Liepsch, K. Perktold, and P. Boesiger. Hemodynamics in the carotid artery bifurcation: a comparison between numerical simulations and *in vitro* MRI measurements. *J. Biomech.*, 33:137–144, 2000.
- [81] F. M. White. *Fluid Mechanics*. McGraw – Hill, Inc., 1994.
- [82] M. C. Potter and J. F. Foss. *Fluid Mechanics*. Great Lakes Press, Inc, Okemos, MI, 1982.
- [83] R. Fahraeus and T. Lindqvist. The viscosity of blood in narrow capillary tubes. *Am. J. Physiol.*, 96:562–568, 1931.
- [84] J. R. Womersley. Method for the calculation of velocity, rate of flow and viscous drag in arteries when the pressure gradient is known. *J. Physiol.*, 127:553–563, 1955.
- [85] J. C. Tannehill, D. A. Anderson, and R. H. Pletcher. *Computational Fluid Mechanics and Heat Transfer*. Taylor & Francis, Washington DC, 1984.
- [86] B. L. Buzbee, G. H. Goulb, and C. W. Nielson. On direct methods for solving Poisson’s equations. *SIAM J. Numer. Anal.*, 7:627–656, 1970.
- [87] C.-C. J. Kuo and B. C. Levy. Discretization and solution of elliptic PDEs – a digital signal processing approach. *Proc. IEEE*, 78:1808–1842, 1990.
- [88] B. L. Buzbee, F. W. Dorr, J. A. George, and G. H. Goulb. The direct solution of the discrete Poisson equation on irregular regions. *SIAM J. Numer. Anal.*, 8:722–736, 1971.
- [89] A. Tura, A. Sarti, T. Gaens, and C. Lamberti. Regularization of blood motion fields by modified Navier-Stokes equations. *Medical Engineering and Physics*, 21:27–36, 1999.
- [90] L. G. Raguin and J. G. Georgiadis. Kinematics of the stationary helical vortex mode in Taylor–Couette–Poiseuille flow. *J. Fluid Mech.*, 516:125–154, 2004.

- [91] J. C. Russ. *The Image Processing Handbook*. CRC Press, Ann Arbor, 1992.
- [92] B. K. P. Horn and B. G. Schunck. Determining optical-flow. *Artificial Intelligence*, 17:185–203, 1981.

MICHIGAN STATE UNIVERSITY LIBRARIES



3 1293 03062 8667